UNIVERSITAT POLITÈCNICA DE CATALUNYA
BARCELONATECH
Departament d'Enginyeria Electrònica

# *"SELECTIVE THERMAL EMITTERS BASED ON PHOTONIC CRYSTALS"*

Thesis submitted in partial fulfillment of
the requirement for the PhD Degree issued
by the Universitat Politècnica de Catalunya,
in its Electronic Engineering Program.

David Hernández García

Director: Ramon Alcubilla
Co-director: Moisés Garín

September 2014

To my family and friends.

Thank you for your support and confidence.

*I know one thing: that I know nothing.*

*Socrates.*

*Only two things are infinite,*
*the universe and human stupidity,*
*and I'm not sure about the former.*

*Albert Einstein.*

# Acronyms

**ALD** Atomic Layer Deposition

**BB** Black Body

**CVD** Chemical Vapour Deposition

**DOS** Density of States

**$E_g$** Bandgap Energy

**FCC** Face Centered Cubic

**FDTD** Finite Differences Time Domain

**FTIR** Fourier Transform Infrared

**HCP** Hexagonal Close-Packed

**HF** Hydrofluoric Acid

**ICMM** Instituto de Ciencia de Materiales de Madrid

**MIT** Massachusetts Institute of Technology

**MNT** Micro i Nano Tecnologies

**mp-Si** Macroporous Silicon

**OTR** Omnidirectional Total Reflection

**PBG** Photonic Band Gap

**PhC** Photonic Crystals

**PhqC** Photonic Quasicrystals

**Pt** Platinum

**PV** Photovoltaic

**PWE** Plane Wave Expansion

**RIE** Reactive Ion Etching

**SCR** Space Charge Region

**SE** Selective Emitters

**SEM** Scanning Electron Microscope

**Si** Silicon

**SiC** Silicon Carbide

**$SiO_2$** Silicon Dioxide

**$T_E$** Emitter Temperature

**TMA** Trimethylaluminum

**TMAH** Tetramethylammonium Hydroxide

**TMM** T-Matrix Method

**TPV** Thermophotovoltaic

**UPC** Universitat Politècnica de Catalunya

# Acknowledgements

This thesis would not have been possible without the collaboration, the help and the work of a number of people from various Universities and Research Centers (Universitat Politècnica de Catalunya, Institut de Ciències Fotòniques, Instituto de Ciencia de Materiales de Madrid, Universitat de Barcelona and Centre de Recerca en Nanoenginyeria). Hereby, I would like to express my gratitude to all of them.

First of all, I would like to thank my supervisor, Prof. Ramon Alcubilla, and Dr. Trifon Trifonov and Dr. Moisés Garín for their guidance, constant support and friendship. Trifon, my mentor, I would have never been capable to develop any of my work without your knowledge and expertise, and above all, your excellent teaching skills. Moisés, any optical result had even sense to me before your patient explanations. Ramon, for your motivating encouragement and for making me questioning so many times *Which is the purpose of it?* To all of you, thank you very much for training me so well on clean room working methods, solid state physics, photonic crystals, macroporous silicon, theoretical simulation, interferometry, heat transfer, SEM/FIB techniques, scientific writing, etc... I have no words!

I will always be in debt with Xavier Fermin, Miguel García and Gema López, the true responsibles of making everything possible in the everyday work, no matter how complex the challenge is. Without their great work there would be no thesis.

I do not forget all my colleagues from the department, both PhD students and professors, together we have shared so excellent moments, great ideas and discussions, trips and beers, that you have become vital to finish this adventure.

I especially thank my family and friends for their love and understanding, their kind support and unconditional confidence since the very beginning. I dedicate this work to them.

My last words are dedicated to those who were there in one or another way but I forgot to mention above. Thank you all!

# Abstract

One of the fundamental limits of conversion efficiency in photovoltaic cells is the broadband distribution of solar spectrum. On one hand, only photons with energy higher than the semiconductor's bandgap can be converted in the device, on the other hand, carriers generated by high energy photons rapidly loose their excess of energy by thermalization with the lattice.

To overcome this limitation, and span the useful convertible region of solar spectrum, many approaches have focused on improving the direct photon to electron conversion by the development of up- and down-converters. A less studied alternative, however, is the use of spectrally narrow distributed emitters, optically matched with the gap energy of the photovoltaic cell, instead of direct sunlight.

Indeed, a material heated by the sun, or another energy source as methane or hydrogen, can re-emit light with suitable spectral distribution and significant higher power density, improving conversion efficiencies in solar cells. This way of operation is known as thermophotovoltaic energy conversion.

Several materials have been considered to be used as emitters in thermophotovoltaic systems. Silicon carbide is a common one, thanks to its high stability at temperatures up to >2000 K. However, its broadband spectral emission limits the conversion efficiency in the photovoltaic device and forces to work at elevated temperatures. Selective emitters, which stand for materials whose thermal emission occupies a narrow spectral region, are a promising alternative to reach elevated conversion efficiencies at lower temperatures.

Natural selective emitters as rare earths have attracted considerable research interest as they present unique emission peaks with the highest emittance level. This approach, however, presents some drawbacks, the spectral

position where strong emission appears is not controllable, and the width of the emission band is relatively narrow, leading to a low power density emitted by the source.

An advantageous way to engineer the selective emission of a thermal source and control the spectral position and bandwidth of strong emission, is by making use of photonic crystals (artificial materials engineered to show optical properties that may not be found in nature). The spectral control of the spontaneous emission in such materials is a unique feature of photonic crystals, although their fabrication, mainly in three-dimensions, is still challenging.

Several interactions between photonic crystals and radiation have been reported: the photonic bandgap effect, surface plasmon polaritons, phonon polaritons, or the microcavity effect, to give some examples. All these approaches allow engineering the thermal emission of materials to match the energy band of the photovoltaic cell and benefit the optical to electrical conversion efficiency, although some limitations arise when utilized in high temperature thermophotovoltaic systems which will be analyzed during the realization of this thesis.

This thesis is therefore devoted to the study of the thermal emission properties and thermal stability of photonic crystal based selective emitters. Various structures have been analyzed: macroporous silicon crystals, photonic quasi-crystals and metallic microcavities. A study in self-assembled colloidal crystals was also started and the preliminary results are presented in the appendix of the document.

Here, it is demonstrated that macroporous silicon crystals and quasi-crystals can inhibit thermal radiation in a controllable manner with thermal stability up to 1500 K. The great selective emission properties of metallic microcavities have also been demonstrated, although the working temperature of such structures is limited below 1100 K to prevent degradation of the metallic layer.

# Contents

# 1

# Introduction

This chapter briefly introduces the concept and state of the art of Thermophotovoltaic (TPV) energy conversion, paying especial attention to the emitter element of the system. The thermal emitter, its thermal stability and the tuning of its spectral radiation are the main research points of the present thesis.

The motivation and objectives of the thesis are also presented at the end of this chapter.

## 1.1 Thermophotovoltaic Energy Conversion

TPV energy conversion is a method for converting thermal radiation into electrical energy.[1,2] The concept was developed in the middle 1950's from an assignment of the U.S. defense department.

### 1.1.1 Concept and Application

The concept of TPV energy conversion is illustrated in Fig. 1.1: thermal energy coming from a heat source (sunlight, fuel or hydrogen combustion, for instance) is focused to a thermal emitter that converts the incoming broadband spectrum into narrowband emission; this radiation is directed to a Photovoltaic (PV) cell to be converted into electricity; in addition, low energy photons radiated by the emitter are reflected back to avoid the heating of the PV device and to help maintaining the temperature of th emitter. Therefore, the components of the system are the heat source, the absorber/emitter element, the PV cell, and a waste heat rejection system.

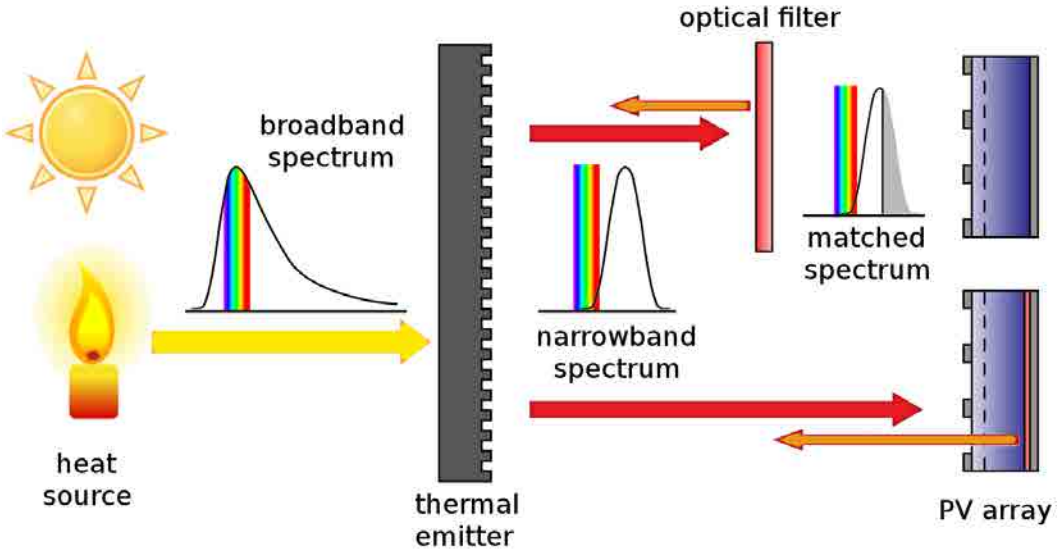


**Figure 1.1:** Diagram of TPV concept: spectrally broadband energy is absorbed and re-emitted into a narrowband spectral region matched with the PV cell. Low energy photons are rejected back to the emitter.

In order to make the process efficient, the energy of the photons reaching the cell must be accumulated in a spectral region slightly above the Bandgap Energy ($E_g$) of the PV semiconductor. This motivates two main points of TPV systems attending to efficiency:

- The use of *low bandgap energy* PV cells, as thermal radiation of bodies at practical temperatures mainly falls into the infrared spectral region.
- The use of *spectral control* techniques to guarantee that only photons with energy higher than $E_g$ reach the PV cell.

Spectral control techniques include the engineering of the emitter's radiation and the waste heat rejection system. This rejection system must be capable to return back to the emitter those photons that are not useful for the solar cell (with energy below $E_g$), helping to maintain the temperature in the emitter. This filtering process, as seen in Fig. 1.1, can be accomplished by optical filters or back surface reflectors in the PV cell. However, the most efficient way of avoiding low energy photons to reach the cell is directly not emitting them. This can be accomplished by the use of thermal emitters

whose spectral radiation occupies a narrow frequency band, minimizing the emitted energy at non-useful spectral ranges, the so-called Selective Emitters (SE).

With this configuration, SE working at a typical temperature of $\sim$ 1500 K, placed at a short distance of the solar converter, can radiate $>$ 25 W/cm$^2$ and concentrate this energy in the desired spectral region.

TPV systems can be added in high temperature industrial processes, such as furnaces or hybrid electric engines, for the co-generation of electricity. In such applications, all wasted heat is derived to the TPV system.

### 1.1.2 On System's Efficiency

From a theoretical point of view, a TPV system can be understood as a heat engine that converts heat energy into work. From that assumption, the Carnot efficiency can be considered as the theoretical limit in such systems,

$$\eta = 1 - \frac{T_C}{T_E} \tag{1.1}$$

where $T_C$ is the temperature of the PV cell, and $T_E$ the one of the emitter. Considering a thermal emitter working at 1500 K and a PV cell at room temperature, efficiency reaches a Carnot's limit of 0.8. In practice, however, TPV reported efficiencies are much lower.

The efficiency of a TPV system can be determined as the product of four major efficiencies:

$$\eta_{TPV} = \eta_{Rad} \cdot \eta_{VF} \cdot \eta_E \cdot \eta_{PV} \tag{1.2}$$

The Radiant Efficiency ($\eta_{Rad}$) is defined as the ratio between the power radiated by the emitter to the power consumed (from the heat source) to reach the working temperature. In TPV systems, it is usual to find an absorber element attached to the emitter. The absorber is designed to absorb the maximum energy from the heat source which is transferred to the emitter by conduction (reaching thermal equilibrium). The absorber-emitter tandem maximizes $\eta_{Rad}$.

The View Factor ($\eta_{VF}$) is related to the amount of energy radiated by the thermal emitter that actually reaches the PV cell(s).

Note the geometrical configuration of the TPV system determines $\eta_{VF}$ and $\eta_{Rad}$. Most research efforts have been centered in the so-called *radiant tube burner configuration*: a cylindrical PV converter array surrounding a thermal emitter on the outside surface of a section of a radiant tube burner. This TPV generator concept maximizes the view factor of the system as the heat source, emitting in all directions, is completely surrounded by the emitter which, itself, is completely surrounded by the PV array.

The Emitter Efficiency ($\eta_E$) is defined as the ratio between the emitter's radiated energy which is suitable for the PV device (above $E_g$) to the total energy radiated by the emitter. The thermal emitter element can be engineered to maximize the "useful" radiation spectrum and, therefore, $\eta_E$.

Finally, the Photovoltaic Efficiency ($\eta_{PV}$), defined as the ratio between the electrical to the optical power in the PV diode. The optimization of these four quantities will determine the final conversion efficiency in the TPV system.

There are many research works reporting on TPV systems' efficiency based on the modeling of theoretical systems.[3–7] The study of $\eta_{TPV}$ as a function of the emitter's temperature carried on by Khvostikov et al.[3] demonstrated the increase in efficiency with emitter's temperature. It is known that radiation of hot bodies follows the Plank's law[8] and, therefore, at higher temperatures the amount of high energy photons increases, gaining a better TPV efficiency in the system. However, this behavior is not maintained at very high temperatures. A large generation of high energy photons far above $E_g$ penalizes the system's efficiency as the excess of photon energy is thermally lost.

Gee et al.[5] reported a 26.9% top efficiency using GaSb cells and photonic crystal emitters working at 1800 K. Previously, Henry[4] calculated the overall TPV efficiency of a tungsten one-dimensional photonic crystal, at operation temperature of 1200 K, using silicon PV cells, in 21.7%. Bernal et al.[6] also reported on maximum efficiency for their micro-TPV system with 2D tungsten emitter and GaSb cells to be 26.2%.

These calculated numbers, however, are based on assumptions and modeling. Engineering limitations and power losses in the different system's elements may provoke wide variations in the mentioned efficiencies. Some experimental realizations are commented in section 1.2.

### 1.1.3 About Thermal Stability

The general emitter temperature in TPV systems is found in the range 1200-1600 K. Therefore, high temperature thermal stability of the emitter element must be a major concern of this thesis.

A common material used as thermal emitter in TPV systems is Silicon Carbide (SiC). Although its broadband emission limits the system's efficiency, its structure and radiation properties remain stable at temperatures >2000 K. Refractory metals such as tungsten present also very high melting points. However, metallic micro-structures turn soft and malleable at lower temperatures. They oxidize in air atmosphere and loose their optical properties much below their melting points.[9] On the other hand, dielectric micro- and nano-structures have proven their thermal stability at temperatures around 1400-1700 K,[10] mainly those made of Silicon (Si) and Silicon Dioxide ($SiO_2$).

It is worth mentioning that TPV systems trying to isolate the PV cell from the heat source, and maintains it at room temperature, by creating distance between the emitter and the converter, avoiding conductive heat transfer and generating energy purely from photons. In principle, thermal stability issues only apply to the thermal emitter element.

### 1.1.4 Remarks

TPV energy conversion is an alternative to classical PV systems where the profit of thermal photons to generate electricity is pursued. Although higher conversion efficiencies can be reached in the PV converter if the adequate radiation spectrum is focused, in practice, low $\eta_{TPV}$ are reported due to limitations in the system's configuration and heat transfer losses. Main advantages of such systems are a considerably increase of the power density reaching the PV cell and the ability to reuse thermal energy from high temperature processes for the co-generation of electricity.

## 1.2 State of the Art

The state of the art of TPV energy conversion is mainly related to the PV device and the spectral control in the emitter element. Two extensive bibliographic works related to TPV were compiled by Broman[11] and the National Renewable Energy Laboratory (NREL) on the series of Conferences on Thermophotovoltaic Generation of Electricity. The most relevant results are reviewed below.

### 1.2.1 Historical Review

The origin of TPV energy conversion is found in the mid-1950's when Henry H. Kolm, at Massachusetts Institute of Technology (MIT)'s Lincoln Laboratory, received a phone call from the U.S. defense department informing that Russians had developed a method for generating electricity from a lantern flame. Kolm's solution was to place a silicon solar cell, which was in the earliest stage of development at Bell Laboratories, next to a lantern, measuring the electrical power output and publishing the results in May 1956. The irony is that the Russian method was thermoelectric, not TPV. During a technical meeting in Europe, Kolm informed of his experiment to Dr. Pierre Aigrain, who is generally considered to be the first to present the concept of TPV in a series of lectures given at MIT in 1960. Early papers by White[1] and Wedlock[2] presented the earliest theoretical and experimental TPV research results. In 1963, Werth[12] showed TPV energy conversion using a propane-heated emitter (working at 1700 K) and germanium solar cells.

Shockley and Queisser[13] showed that, for Black Body (BB) radiation sources, the efficiency of a TPV system is strongly dependent upon the ratio of the cell's $E_g$ to the Emitter Temperature ($T_E$). They found the relation $E_g \approx 2kT_E$ to achieve maximum efficiency. Considering this, the optimal working temperature for a BB emitter working with Si solar cells ($E_g = 1.1$ eV) is around 6500 K (i.e. the temperature of the Sun). No workable materials exist at these temperatures. Therefore, for efficient TPV conversion at reasonable temperatures, BB sources cannot be used and PV materials with lower $E_g$ must be considered.

As a result, TPV research has focused on tailoring the emitter radiation to concentrate emission just above the bandgap energy of the PV cell, where the device is most efficient, and on low bandgap energy semiconductors. In the 1980's, new efficient

PV materials such as InGaAs became available increasing the interest in TPV energy conversion.

### 1.2.2 The Photovoltaic Cell

Low bandgap PV cells are one critical component to achieve the highest conversion efficiency in TPV systems. Each semiconductor has unique bandgap energy, determined by its crystalline structure, as shown in Table 1.1. Ternary and quaternary compounds as InGaAs and InGaAsSb are the ones showing the lowest $E_g$ and, therefore, being the ideal candidates for TPV systems.

**Table 1.1:** Bandgap energy of various PV materials.

| **Material** | $\mathbf{E}_g$ |
|---|---|
| Si | 1.1 eV |
| GaSb | 0.72 eV |
| Ge | 0.66 eV |
| $In_xGa_{1-x}As$ | $0.4 - 1.4$ eV |
| $In_xGa_{1-x}As_ySb_{1-y}$ | $0.5 - 0.6$ eV |

$E_g$ determines the useful convertible spectrum of the energy radiated by the thermal emitter, as it is depicted in Fig. 1.2. The area enclosed by the BB radiation curve and the left part of $\lambda_g$ (higher energy photons) represents the useful area. Note $\lambda_g$ is the bandgap energy of the semiconductor expressed in terms of wavelength. As it is observed, this area increases with temperature and depends on the chosen semiconductor.

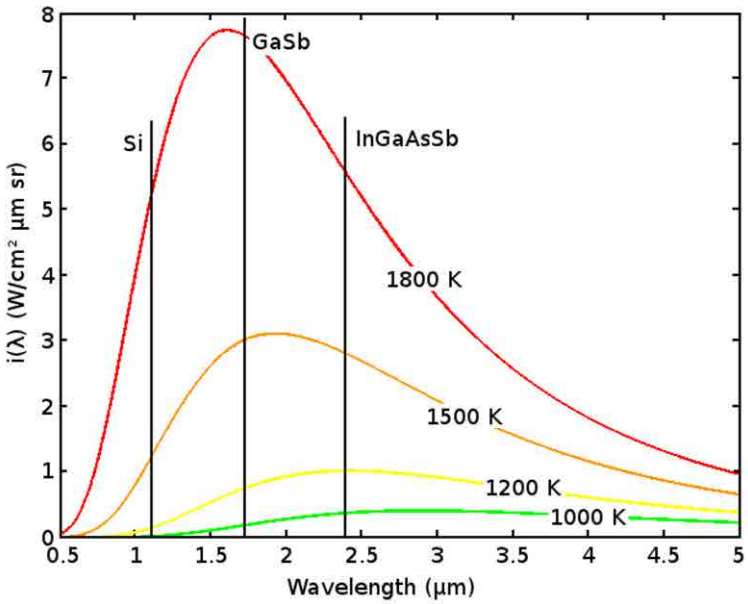


**Figure 1.2:** Spectrum of BB thermal radiation at different temperatures. $\lambda_g$ for various semiconductors is added to highlight the useful spectrum for PV generation.

First demonstrations of PV devices were a AgCl cell coated with a platinum electrode, immersed into acid solution, by Becquerel in 1839;[14] and a photoconductive effect on selenium in 1883 by Fritts.[15] It was not until 1941 when the first p-n junction solar cell was introduced by Russell Ohl.[16,17] From that time on, most PV cells have been fabricated based on p-n junctions thanks to the conversion efficiencies that can be easily reached. These p-n junctions, however, have a theoretical limit known as Shockley-Queisser limit:[13] 31% at 1 Sun and 41% efficiency when concentrated sunlight is considered. There are four main efficiency losses that determine this limit:

- Photons with energy below $E_g$ do not generate electron-hole pairs.
- Photons with energy far above $E_g$ do not generate more electron-hole pairs but the excess energy is lost as heat in the device.
- The natural recombination of excited electrons before extraction.
- Finally, the extracted voltage, reflecting the energy difference between the two electrodes, is less than $E_g$.

In a laboratory environment, the record Silicon solar cell efficiency at 1 Sun (single p-n junction), held by the University of New South Wales in Sydney, Australia, is 25%.[18]

Beyond the limit of p-n junctions, extensive research has been undertaken to increase the PV efficiency by increasing the useful conversion bandwidth of solar spectrum. Third generation PV cells (second generation stands for low cost technologies) includes tandem solar cells, frequency conversion and hot-carrier effects with the aim of improving the results obtained by first generation devices by the combination of different materials and photonic effects in the devices.[19] However, the cost of third generation approaches, such as multi-junction solar cells, is still too high for its commercial use except in specialized applications. This high cost mainly comes from the manufacture of complex structures and the high price of materials.

In the academic environment, extensive research has been undertaken on low energy semiconductors such as InGaSb, InGaAsSb or InGaAsP.[20–24] Despite these materials technology is well-assessed for applications such as near-infrared detectors, lasers or LEDs, they present again a main drawback in the cost of the substrate to be included as commercial PV devices.

In practice, GaSb (0.72 eV) is widely used in TPV systems due to its relatively easy fabrication process, although alternative materials with very low $E_g$ as quaternary InGaAsSb would be sensitive to a greater portion of the thermal spectrum.[25]

### 1.2.3 Spectral Control

TPV systems, considered also one of the third generation solar cells, pursue a very different strategy to increase the optical-to-electrical conversion efficiency: rather than focusing on the solar cell, the emphasis is shifted on controlling the spectra of the photons entering the PV device.[26,27] Broadband thermal radiation is absorbed by the absorber/emitter element to reach the working temperature and re-emit photons that are optimized to match the PV cell's $E_g$.

Fig. 1.3 shows the common approaches to the spectral control in TPV systems. Filters are a common way to avoid undesired photons to reach the cell, helping at the same time to maintain the emitter temperature by recycling low energy photons back into the hot element. However, they introduce additional losses in the system and are out of the scope of the present work. On the other hand, spectral control can be

directly embedded into the emitter to control the spectral emission properties of the element, as it is the case of rare earth based SE, Photonic Crystals (PhC) based SE and anti-reflective coatings.[7,28]

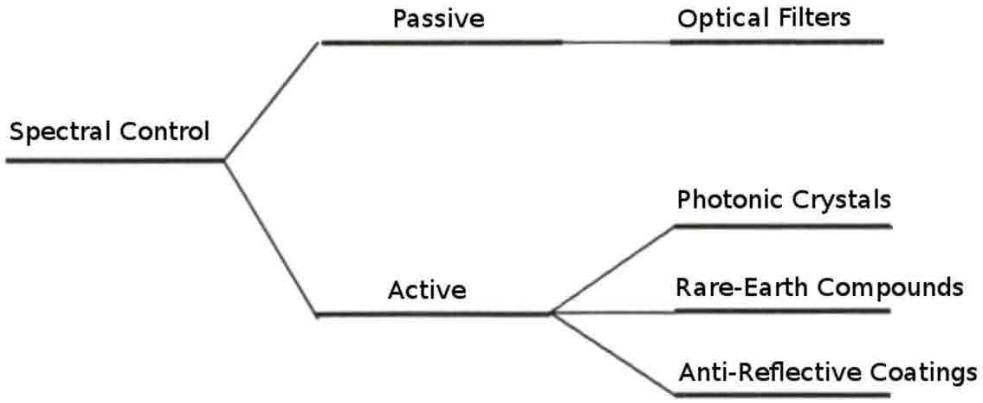


**Figure 1.3:** Some avenues of TPV spectral control.

### Rare Earth based Selective Emitters

Rare earth based SE[29–31] are a common subject of study as rare earths present unique optical properties due to some radiative transitions between energy levels. These materials also present very high melting points and high temperature stability.

The first rare earth SE were polycrystalline in structure. Guazzoni[32] built rare earth oxide emitters of the order of 1 mm by sintering oxide powders. They exhibited large emittance in the emission bands, but also undesirably large emittance outside the emission bands. Nelson and Parent[33,34] developed fibrous rare earth oxide emitters resulting in much lower spectral emittance outside the emission bands.

As an example, an $Yb_2O_3$ emitter heated at $\sim$ 1700 K presents a sharp emission peak centered at 1.27 eV with 0.85 emissivity. Another compound as $Er_2O_3$, presents a selective emission peak at 0.8 eV with 0.82 emissivity.[35,36] The spectral emissivity of $Er_2O_3$ at 1073 K is shown in Fig. 1.4.

These approaches, however, present some drawbacks, the spectral position where strong emission bands appear is not controllable because it is intrinsic to each kind of rare earth, and the width of the emission band is relatively narrow, leading to low power density emitted by the source. Besides, these materials are restricted to oxide ceramics or crystals whose thermal conductivity is low. They are also highly influenced

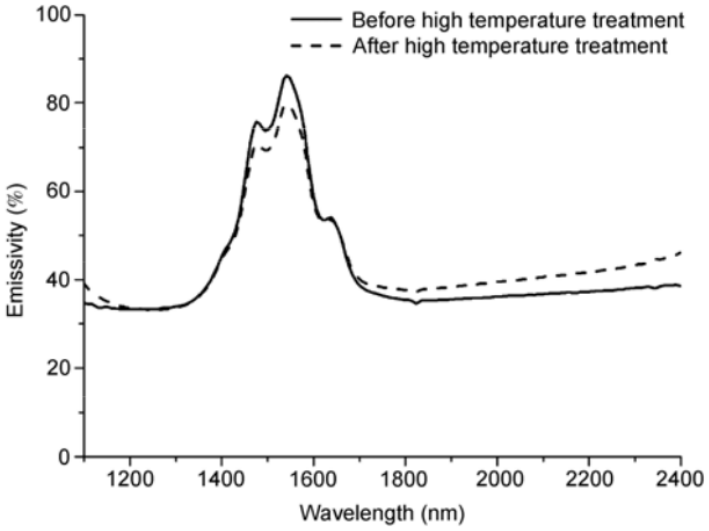


**Figure 1.4:** High temperature (800 °C) normal spectral emissivity of $Er_2O_3$ before and after high temperature treatment at 1400 °C. Extracted from[36].

by bulk factors such as scattering at the grain boundaries, inclusions of particles or inclusions of dopants. This means that even small variations of crystalline structure, chemical composition or impurities, can drastically vary the radiation properties of rare earth based SE.

An extensive work on rare earth selective emission is summarized in the texts of Wyboune and Dieke.[37,38]

### Photonic Crystal based Selective Emitters

An alternative method for achieving selective emission in materials that normally show a broadband emission spectrum is modifying their physical structure at micro and nanoscale through a periodic variation of their refractive index. These photonic crystals are designed to forbid the transmission of light at certain wavelengths, the so-called Photonic Band Gap (PBG) regions,[39] where reflectance becomes the highest and the spontaneous emission is inhibited. These materials can be designed to suppress thermal radiation at the spectral region of interest by matching their PBG to the cell's $E_g$, avoiding the production of low energy photons.

Although PhC have been studied since 1887, in the form of one-dimensional (1D) periodic multi-layers of alternate dielectrics (such as Bragg mirrors), it was in 1987 when

Yablonovitch and John published two milestone papers on PhC.[40,41] Yablonovitch's idea was to engineer the photonic Density of States (DOS) for controlling the spontaneous emission of materials; John's idea was to use PhC for affecting and guiding light modes. The structures Yablonovitch produced were three-dimensional (3D) PhC based on drilling three intersecting arrays of holes into a block of ceramic material, named *Yablonovite* after him.[42]

The structuring methods for PhC can be listed as: periodic layers of alternating materials (1D), posts or holes etched into the substrate material (2D), or volumes with crystalline structure (3D). An schematic can be seen in Fig. 1.5.

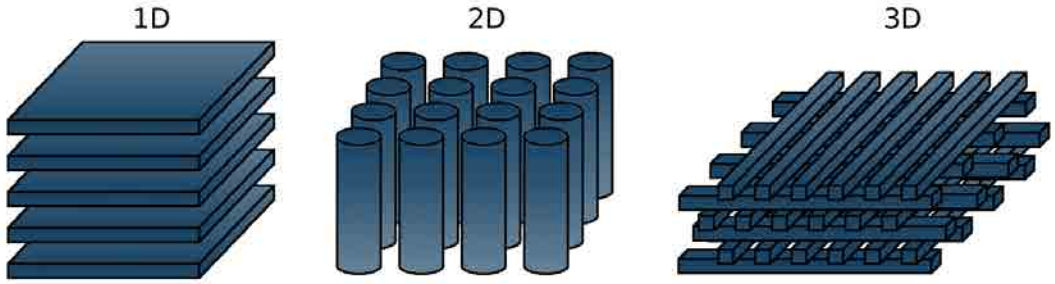


**Figure 1.5:** PhC structuring in 1-dimension, 2-dimensions and 3-dimensions.

An extensive work to develop SE based in 3D PhC was done by Lin et al. at *Sandia National Labs*.[10,43–45] A woodpile structure was fabricated layer-by-layer adjusting size and periodicity to reach a Face Centered Cubic (FCC) structure showing an absolute PBG in the near infrared. The structure is shown in Fig. 1.6a and the resulting photonic DOS in Fig. 1.6b, showing a PBG centered at 0.5 $c_0/a$ (note frequency units are represented as a function of the structure's lattice $a$ due to the commented scalability of Maxwell's equations).

Experimental measurements proved that thermal radiation got strongly inhibited within the forbidden band (PBG) of such structure, while emittance on the outside spectrum exceeded the one of bare material.

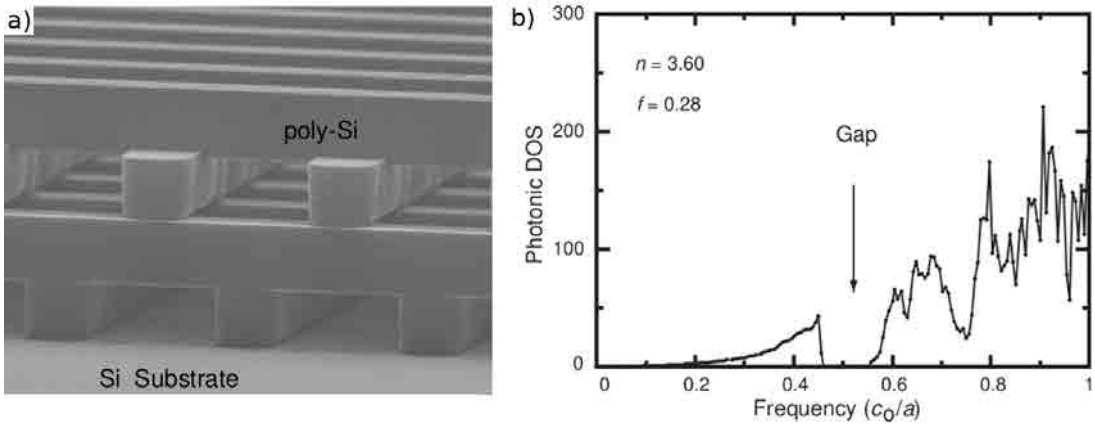


**Figure 1.6:** (a) SEM image of a 3D woodpile photonic structure. (b) Photonic DOS of the optical structure as a function of the lattice constant $a$. Extracted from [10].

The woodpile structure, originally made of polysilicon, was replicated in tungsten to take profit of the high melting point of the metal, and its low emissivity in the infrared. [44] The higher contrast of refractive indexes in this metallic structure expanded the photonic gap reaching a wide spectral region where thermal radiation was inhibited. Thermal emission measurements of these metallic PhC are presented in Fig. 1.7 for different temperatures. The BB radiation at 1500 K is also plotted for comparison. It is observed the low radiation of the metallic structure above 2 $\mu$m wavelength.

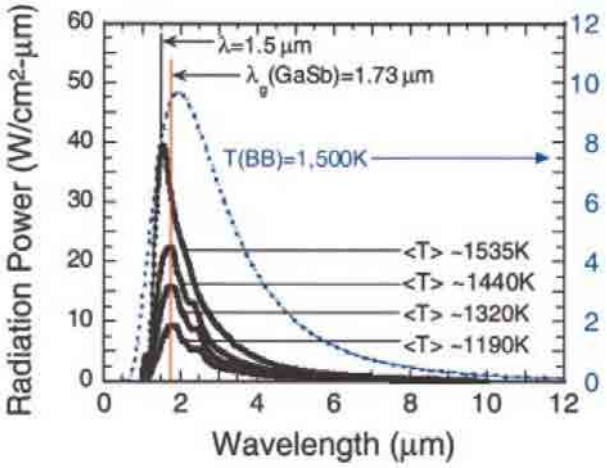


**Figure 1.7:** W-PhC radiation power at different temperatures from 1190 to 1535 K. Experimental measurements are compared with BB emission at 1500 K. Extracted from [43].

The main drawback of these metallic structures is the lack of thermal stability. Above 1200 K, the microstructured metal becomes soft and malleable breaking the structuring. This effect was also observed by Sai et al. in his bidimensional structures consisting in periodic arrays of metallic microcavities (see Fig. 1.8).[46–48] Sai demonstrated a reduction in the reflectance response of such structures, which translated in an enhancement of the emittance at NIR wavelengths.

The limitation of high temperature thermal stability of metallic microstructures was recently partially overcome by the addition of an Atomic Layer Deposition (ALD) coating of $HfO_2$ on the PhC surface to avoid structure degradation. Samples showed long term thermal stability for more than 144 hours above 1200 K.[49,50]

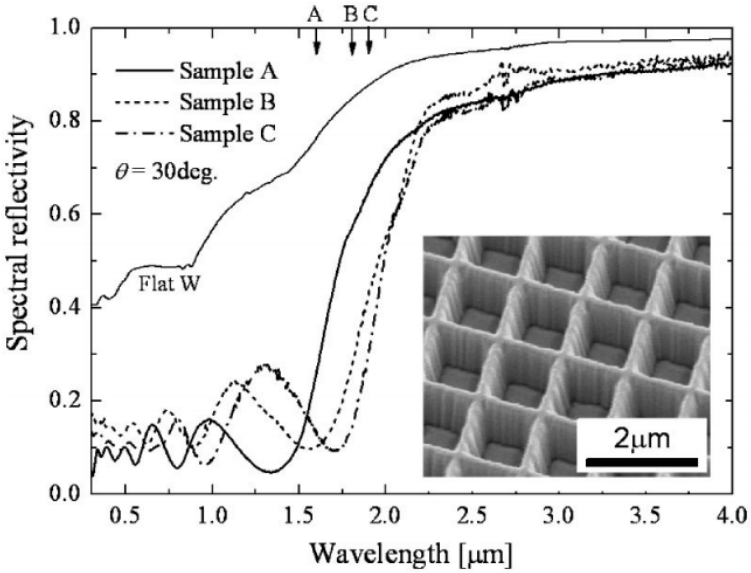


**Figure 1.8:** Reflectivity of the W-PhC (2D periodic microcavities). It is observed a decay at lower wavelengths due to the structuring. Two configurations, attending to the depth of the cavities, are compared. Extracted from[47].

### Macroporous Silicon Photonic Crystals

Another important research line on PhC is porous silicon. Although it was discovered in 1956, when researchers from Bell Labs were looking for chemical polishing techniques of Si, it was not until the 80's decade when Canham[51] presented a first device based in porous silicon. It was light-emitting diodes for the spectral region 1.3-1.6 $\mu$m.

Macroporous silicon PhC were developed, both at design and fabrication levels, by the Micro i Nano Tecnologies (MNT) research group through the work of Dr. Trifonov and Dr. Garín.[52,53] An overview of the achievements is presented in section 3.4.

Periodic structures can be created in bare-Si through a two-steps process: first, the distribution of the pores on the silicon surface is defined by lithography and, then, an electrochemical etching of the silicon allows to define different pore shapes and modulation periodicities in depth. These so-called Macroporous Silicon (mp-Si) structures, with pores sizing $> 50$ nm, are capable to modify the material's emission at the visible and infrared spectral regions.[54–57] Examples of mp-Si structures are presented in Fig. 1.9. As it is observed, different periodicities can be reached, showing different optical responses as a function of the structure's size.

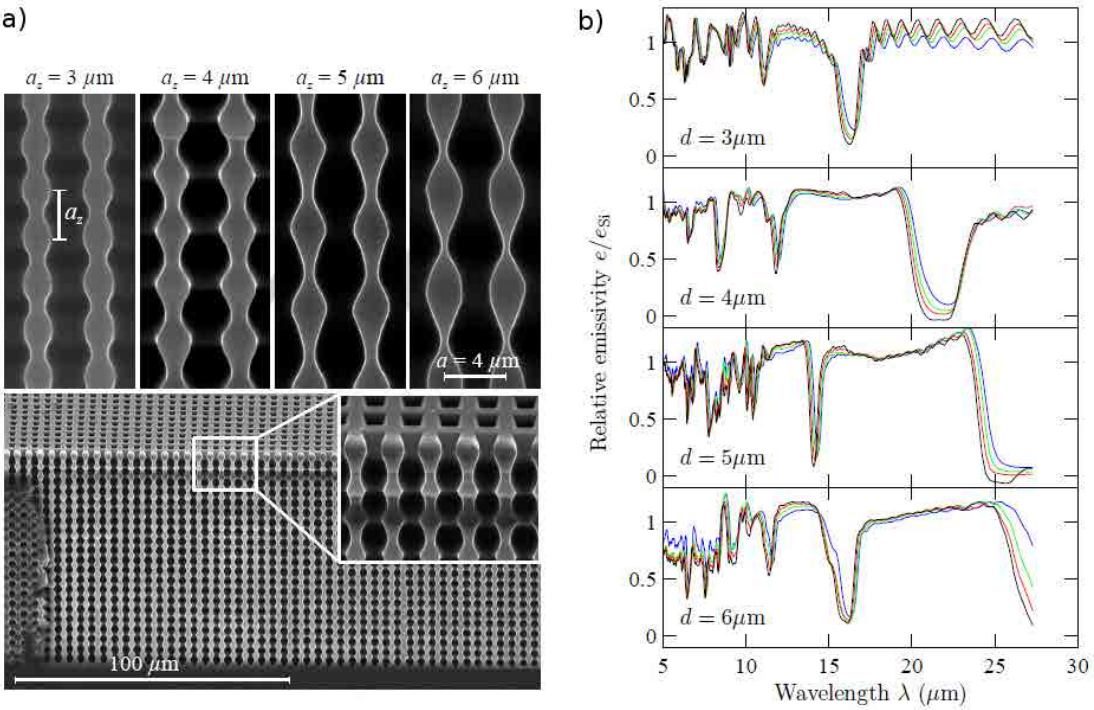


**Figure 1.9:** (a) SEM images of mp-Si samples with different modulation periodicities. A bird's eye view of the sample and zooms into the pores' modulation is shown. (b) Normalize emittance spectra. Black, red, green and blue lines stand for emittance measured at temperatures 100, 200, 300 and 400 °C respectively. Extracted from[57].

### Self-Assembled Photonic Crystals

Worth mentioning photonic structures are self-assembled colloidal crystals which enjoy great popularity due to its ease of access and the richness of results offered.[58,59] These self-assembled structures achieve long-range ordering with a natural diffraction effect for propagating light with wavelength comparable to particle size. Some examples are presented in Fig. 1.10.

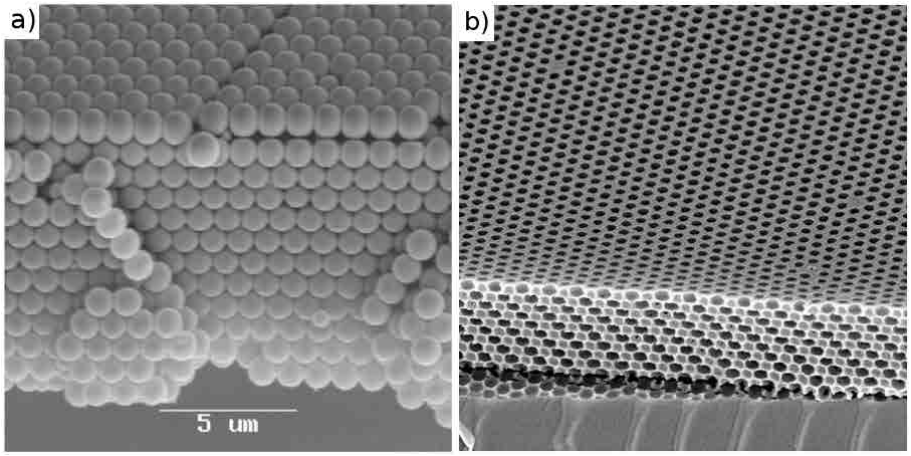


**Figure 1.10:** Self-assembled PhC structures: (a) artificial opal and (b) inverse opal.

Self-assembly is a natural method to obtain 3D PhC in the optical range by controlling the photonic DOS, as proposed by Yablonovitch in his pioneering work of 1987.[40] It was in the mid-90's when the first experimental realization of 3D structures based on self-assembled artificial opals were performed by Astratov et al.[60]

The suppression of spontaneous emission in inversed opal structures has been widely demonstrated.[61–63] As photonic crystals, these structures inhibit radiation within the PBG region and enhance it outside. Also, it has been demonstrated that the radiation pattern can present a strong angular dependence in these self-assembled crystals.[64,65]

More recently, spectral emission control has been proved in metallic inversed opal structures (made of tungsten), which also present high thermal stability up to 1700 K when the structure is coated with a film of $HfO_2$.[66]

### 1.2.4 TPV Prototypes

Some TPV prototypes have been presented in the last years reporting some interesting conversion efficiencies and output electrical power densities. Here, it is presented a summary of the most relevant.

Qiu and Hayden[67,68] investigated various gas fired radiators and the influence of the combustion process on the radiant power and efficiency. Investigations showed that the main losses are relative to the conversion of fuel to radiant energy, suggesting this conversion efficiencies could be increased by the use of selective emitters. Such TPV system was improved presenting a novel cascaded system combining TPV and thermoelectric generation.[69] This power generation system consisted of a natural gas burner, a SiC emitter, a ceramic glass optical filter, GaSb solar cells and a PbSnTe based thermoelectric converter. The system reached 1.5% conversion efficiency in the TPV element, and 5% in the thermoelectric element, taking profit of the residual heat.

Durisch et al. presented a prototype consisting of butane burner with an $Yb_2O_3$ SE and commercial Si solar cells.[70] The prototype showed a 1.1% efficiency (15 W output power for 1.35 kW input). The system was improved afterwards by improving the quality of the used Si converters and changing the system's geometry to avoid inhomogeneous irradiation on the photocells, $\eta_{TPV}$ rised up to 2.4%.

A further better approach was developed by Fraas et al. based on a tungsten emitter and GaSb PV cells.[71] The use of such metallic emitter forces to work in vacuum to avoid oxidation of the metallic emitter, however, the natural selective emission of tungsten made the system achieving a conversion efficiency of $\eta_{TPV} = 11\%$.

Recently, a full solar TPV device developed by Lenert et al.[72] took advantage of the nanophotonic properties of the absorber-emitter surface to reach a experimental efficiency of 3.2%. The device integrates a multiwalled carbon nanotube absorber and a one-dimensional $Si/SiO_2$ photonic crystal emitter on the same substrate, with the absorber-emitter areas optimized to tune the energy balance of the device.

## 1.3 Thesis Objectives

In previous sections, the concept of TPV energy conversion and its state of the art were presented, together with a description of the system's implementation, design and main drawbacks. The thermal emitter is one of the most important elements to be optimized attending to TPV system's efficiency. The principal objective of this thesis is the study of the thermal emission properties of photonic crystals and their optimization as tunable selective emitters. The emitter efficiency ($\eta_E$) and high temperature thermal stability tests are the main points to evaluate the fabricated crystals.

Three different kind of structures were designed and studied, named macroporous silicon PhC, macroporous silicon Photonic Quasicrystals (PhqC) and metallic PhC. The characterization of the optical response of these structures was performed up to 1100 K by direct thermal emission measurements. Thermal stability tests were performed at higher temperatures in muffle ovens for different atmospheres. As part of the thesis work, a high temperature characterization setup was developed to be capable to experimentally measure the thermal emission of the crystals.

As part of this thesis, the analysis of self-assembled PhC as selective emitters was started in close collaboration with various research groups from the Universitat Politècnica de Catalunya (UPC) and the Instituto de Ciencia de Materiales de Madrid (ICMM). The first achievements of this new approach are presented at the end of the document.

This work is founded in the group's previous experience on macroporous silicon fabrication and optical characterization at high temperature.

This thesis is organized as follows:

**Chapter 1** introduces the concept of thermophotovoltaic energy conversion and the state of the art. The chapter briefly analyzes the different elements of a TPV system and focuses on the thermal emitter element, showing the ability of photonic crystals to work as high temperature selective emitters.

**Chapter 2** is devoted to the theoretical background of light-matter interaction in photonic crystals. The chapter starts with the well-known Maxwell's equations to find their solutions in periodic media and obtain the reflectance, transmittance and emittance properties of the media.

**Chapter 3** describes the fabrication techniques of macroporous silicon based selective emitters and the optical characterization techniques at room temperature and at high temperature utilized during the realization of this work.

**Chapter 4** presents the main results on selective emission of macroporous silicon PhC and PhqC. The thermal stability of these silicon-based samples is analyzed in this chapter.

**Chapter 5** presents the main results on selective emission of metallic PhC. The chapter analyzes the resonant emission enhancement within periodic metallic microcavities and the high temperature thermal stability of the samples.

**Chapter 6** summarizes the main points of the thesis, presents the conclusions of the work and analyzes the future work to be performed.

**Appendix A** presents the preliminary results on self-assembled colloidal structures as NIR selective emitters. This work was initiated in collaboration with different research groups and is still in progress.

**Appendix B** describes in detail the developed high temperature characterization setup as a fundamental part of the thesis work.

# 2

# Theoretical Background

In chapter 1 it was introduced how thermal emitters should adapt their spectral radiation to the PV cell needs in order to increase conversion efficiencies in the TPV system. The use of PhC is the optimal way of accomplishing this objective.

In this chapter, the most relevant theoretical background to understand the physics that govern the emission properties of materials, in particular photonic crystals, will be briefly presented starting with the well-known Maxwell's equations.

## 2.1 From Maxwell's Equations to Photonic Crystals

Energy transfer between the thermal emitter and the PV device is performed by radiation phenomena, which consists of electromagnetic waves that mainly lay on the near and medium infrared (NIR and MIR) spectral regions. The interaction between electromagnetic waves and matter is described by Maxwell's equations.

Maxwell's equations must be solved in every particular case to obtain the spectrum that will be radiated by a particular thermal emitter. Note that Maxwell's equations must be completed with absorption and scattering coefficients to consider the case of emitting/absorbing mediums.

The material which is presented in this section has been extracted from classic optics texts like *"Principles of Optics: Electromagnetic theory of propagation interference and diffraction of light"* by Born and Wolf, and the Joannopoulos' text on photonic crystals *"Photonic crystals: Molding the flow of light"*.[39]

### 2.1.1 Maxwell's Equations

The Maxwell's equations for the electric field, **E**, and magnetic field, **H**, are the following:

$$\nabla \times \mathbf{H} = \mathbf{J} + \frac{\partial \mathbf{D}}{\partial t} \tag{2.1}$$

$$\nabla \times \mathbf{E} = -\frac{\partial \mathbf{B}}{\partial t} \tag{2.2}$$

$$\nabla \cdot \mathbf{D} = \rho \tag{2.3}$$

$$\nabla \cdot \mathbf{B} = 0 \tag{2.4}$$

where **J** is the conduction current, **D** is the electric displacement, **B** the magnetic induction and $\rho$ the electric charge density. In addition to that, the constitutive relations for the media are:

$$\mathbf{D} = \varepsilon_0 \cdot \mathbf{E} + \mathbf{P} = (\varepsilon_0 + \chi) \cdot \mathbf{E} = \varepsilon \mathbf{E} \tag{2.5}$$

$$\mathbf{B} = \mu_0 \cdot (\mathbf{H} + \mathbf{M}) = \mu_0 \cdot (1 + \chi_m) \cdot \mathbf{H} = \mu \cdot \mathbf{H} \tag{2.6}$$

$$\mathbf{J} = \sigma \mathbf{E} \tag{2.7}$$

The electric dipole moment, **P**, depends linearly upon **E** for most media. Therefore, the electric permitivity $\varepsilon$ can be expressed as the sum of the vacuum permitivity $\varepsilon_0$ and the electric susceptibility $\chi$. Similarly, the magnetic field has a contribution from the magnetic dipole moment, **M**, linearly dependent of **H** for most media, and then the magnetic permeability $\mu$ can be expressed as the product of the vacuum permeability $\mu_0$ and the magnetic susceptibility $\chi_m$ plus 1.

In these equations, the properties of a medium are represented: $\varepsilon$, $\mu$ and $\sigma$. In the case of isotropic media, these properties are scalar quantities, however, in anisotropic media, as the case of PhC, these properties must be considered tensors.

For the moment, let's consider the simplest case of light-matter interaction in which the following conditions are satisfied:

1. We assume isotropic media, so $\varepsilon$ and $\mu$ are scalar quantities.

2. We are in the linear regime, so $\mathbf{D}$ is linearly dependent on $\mathbf{E}$, and $\mathbf{B}$ is linearly dependent on $\mathbf{H}$.

3. We ignore any explicit frequency dependence (material dispersion) of the dielectric constant $\varepsilon$. Instead, we simply choose the value of $\varepsilon$ appropriate to the frequency range of work.

4. We assume non-magnetic and non-electric media, so $\mu = \mu_0$ and $\sigma = \rho = 0$.

In such case, Maxwell's equations can be simplified as follows:

$$\nabla \times \mathbf{H} = \varepsilon \frac{\partial \mathbf{E}}{\partial t} \tag{2.8}$$

$$\nabla \times \mathbf{E} = -\mu_0 \frac{\partial \mathbf{H}}{\partial t} \tag{2.9}$$

$$\nabla \cdot \mathbf{E} = 0 \tag{2.10}$$

$$\nabla \cdot \mathbf{H} = 0 \tag{2.11}$$

In general, both $\mathbf{E}$ and $\mathbf{H}$ are complicated functions of both time and space. Because the Maxwell's equations are linear, however, we can separate the time dependence from the spatial dependence by expanding the fields into a set of harmonic modes. This is no great limitation, since we know by Fourier analysis that we can build any solution with an appropriate combination of these harmonic modes. The harmonic modes are mathematically expressed the following way:

$$\mathbf{E} = \mathbf{E}_0 \cdot e^{j(\mathbf{kr}-\omega t)} = \mathbf{E}(\mathbf{r}) \cdot e^{-j\omega t} \tag{2.12}$$

$$\mathbf{H} = \mathbf{H}_0 \cdot e^{j(\mathbf{kr}-\omega t)} = \mathbf{H}(\mathbf{r}) \cdot e^{-j\omega t} \tag{2.13}$$

where the wave vector $\mathbf{k}$, that points in the direction of wave propagation, must be independent of $\mathbf{r}$. Same reasoning must be considered for the frequency $\omega$ and $t$. These solutions apply for both $\mathbf{E}$ and $\mathbf{H}$ under the medium conditions just described. When replacing this into the simplified Maxwell's equations, we obtain the curl equations:

$$\nabla \times \mathbf{H}(\mathbf{r}) = -j\omega\varepsilon\mathbf{E}(\mathbf{r}) \tag{2.14}$$

$$\nabla \times \mathbf{E}(\mathbf{r}) = j\omega\mu_0\mathbf{H}(\mathbf{r}) \tag{2.15}$$

The **master equation** is obtained when combining the two above:

$$\nabla \times \left(\frac{1}{\varepsilon}\nabla \times \mathbf{H}(\mathbf{r})\right) = \left(\frac{\omega}{c}\right)^2 \mathbf{H}(\mathbf{r}) \tag{2.16}$$

where $c$ is the vacuum speed of light: $c = 1/\sqrt{\varepsilon_0\mu_0}$. Note the master equation is in terms of $\mathbf{H}$. The solution of the electric field $\mathbf{E}(\mathbf{r})$ is obtained by solving the curl equation from $\mathbf{H}(\mathbf{r})$.

The physical interpretation of the master equation is the following: we perform a series of operations on a function $\mathbf{H}(\mathbf{r})$, and if $\mathbf{H}(\mathbf{r})$ is really an allowable electromagnetic mode of the studied media, the result will be a constant times the original function $\mathbf{H}(\mathbf{r})$. This situation arises often in mathematics and is called an *eigenvalue problem*: the function $\mathbf{H}(\mathbf{r})$ is called the *eigenfunction* or *eigenvector* of the operator $\hat{\Theta}$, and the multiplicative constant $(\omega/c)^2$ is called the *eigenvalue*.

$$\hat{\Theta}\mathbf{H}(\mathbf{r}) = \left(\frac{\omega}{c}\right)^2 \mathbf{H}(\mathbf{r}) \tag{2.17}$$

The solutions of the eigenvalue problem determine, indeed, a relation between $\omega$ and $\mathbf{k}$, as the above equation returns the allowed eigenfunctions $\mathbf{H}(\mathbf{r})$ for each allowed eigenvalue $(\omega/c)^2$, and $\mathbf{H}(\mathbf{r}) = H_0 e^{j\mathbf{kr}}$. The so-called dispersion relation is then obtained when solving the eigenvalue problem in a particular media:

$$\mathbf{k}^2 - \mu_0\varepsilon\omega^2 = 0 \Longleftrightarrow \omega = \frac{c}{n} \cdot \mathbf{k} \tag{2.18}$$

The dispersion relation divides the space of solutions in two: for the refractive index $n = \sqrt{\varepsilon_r}$ being 1, we find the solution for harmonic modes traveling in air. When $n > 1$, we find modes traveling into media. In homogeneous media, $\omega(\mathbf{k})$ is linearly related with the velocity of wave propagation in the media $c/n$. In more complex systems, the different $\omega(\mathbf{k})$ curves must be solved for a dependent refractive index on propagation direction, $n(\mathbf{k})$.

An example of the dispersion relation is depicted in Fig. 2.1 where it is considered the following case: a piece of Si of thickness $a$, infinite in the XY plane, placed in air,

and a wavefront traveling in the $\hat{\mathbf{z}}$ direction. The master equation 2.17 is solved and the different allowed $\mathrm{H}(\mathbf{r})$ and $\omega$ are obtained. The discrete lines in Fig. 2.1 correspond to modes that are localized in the piece of material, the shaded region is a continuum of states that extend to the air and the red line corresponds to the *light line* ($\omega = c\mathbf{k}$).

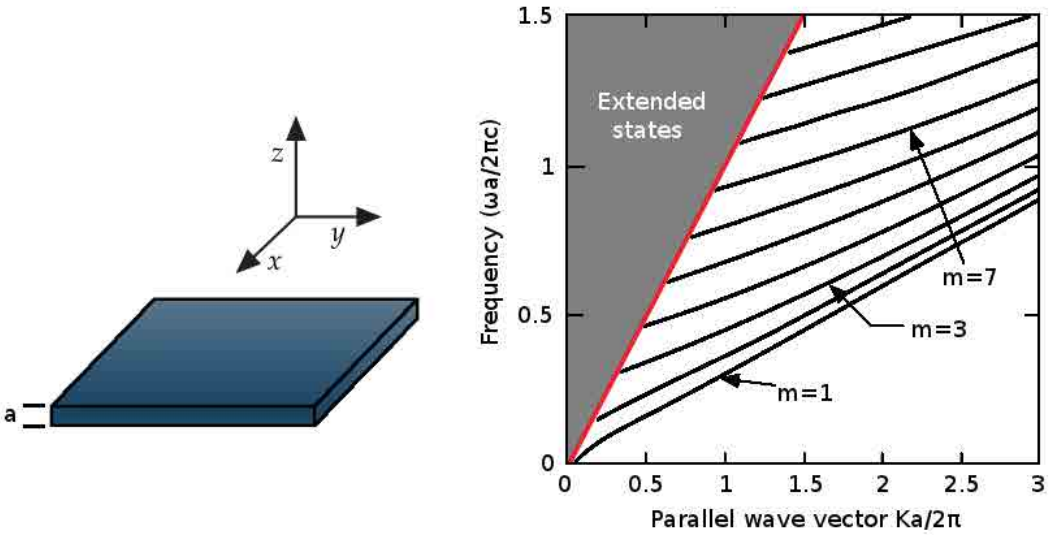


**Figure 2.1:** Dispersion relation for an homogeneous media with $n = 3.42$ and thickness $a$. The different propagating modes in media and air are represented considering propagation in $\hat{\mathbf{z}}$ direction. Extracted from[39].

Note the axis are normalized against the lattice parameter $a$. An interesting feature of electromagnetism in dielectric media is that there is no fundamental length scale other than the assumption that the system is macroscopic. This leads to simple relationships between electromagnetic problems that differ only by a contraction or expansion of all distances: the solution of the problem at one length scale determines the solutions at all other lengths by scaling all distances.

### 2.1.2 Dispersion Relation & Photonic Crystals

Photonic crystals affect light propagation in a similar way that semiconductors affect electron propagation. If semiconductors posses a periodic potential which defines valence and conduction energy bands for electrons, and a gap in between, the optical analogue present a periodic dielectric function which can exhibit a photonic bandgap (PBG), *i.e.* a certain energy range in which photons are prohibited to propagate along

the periodic material regardless of polarization and propagation direction. This is accomplished if the dielectric constants of the materials in the crystal are sufficiently different.

If the absorption of light by the materials is minimal, the partial reflections from all of the various interfaces of the crystal experiment constructive interference in the PBG region, and the light is totally reflected, avoiding transmission. In addition, as absorption is minimal, the emittance of the crystal is inhibited within the PBG. This way, PhC can be designed as selective emitters by tuning the PBG to the desired frequency range by properly choosing the materials, their optical properties and the microstructure of the emitter.

To solve Maxwell's equations in PhC, let's continue with the eigenvalue problem. The spectrum of PhC is the totality of all of the eigenvalues $\omega$, but we must consider now the solutions in a medium with discrete and periodic $\varepsilon(\mathbf{r})$. The simplest possible PhC, shown in Fig. 2.2, consist in alternating layers of materials with different dielectric constant. Note the lattice constant $a$ refers now to the periodicity of the system, and not the thickness of the layer as in Fig. 2.1.

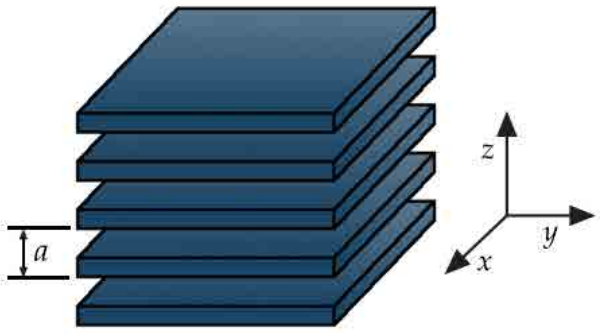


**Figure 2.2:** One dimensional photonic crystal with lattice constant $a\hat{\mathbf{z}}$.

Although this simplest system can be analytically resolved, we will use the dispersion relation to analyze its optical behavior. We can apply the Floquet-Bloch theorem,[73] which tells us that the solutions to the eigenvalue problem can always be chosen to have the form of a plane wave times a function with the periodicity of the lattice. In other words, the solutions to equation 2.17 are plane waves modulated by a lattice periodic function:

$$e^{j\mathbf{kr}} \cdot \mathbf{u}(\mathbf{r}) = e^{j\mathbf{kr}} \cdot \mathbf{u}(\mathbf{a} + \mathbf{r}) \tag{2.19}$$

The solutions for these modes, due to the periodic function, can be completely characterized by their behavior in a single primitive cell. This primitive cell, named *irreducible Brillouin zone*, is uniquely defined and simplifies the computational space into a few **k**-directions that characterize the whole system by reducing the several symmetries that can be found in a periodic system for wave propagation.

For now, let's consider waves that propagate entirely in the $\hat{\mathbf{z}}$ direction, crossing the dielectric sheets of Fig. 2.2 at normal incidence. In Fig. 2.3, $\omega(k_z)$ is plotted for three different multilayer films: a system in which all layers have the same dielectric constant; a system with dielectric constants of 12 and 13; and a system with dielectric constats 1 and 13. The diagram is plotted inside the Brillouin zone from -0.5 to 0.5.

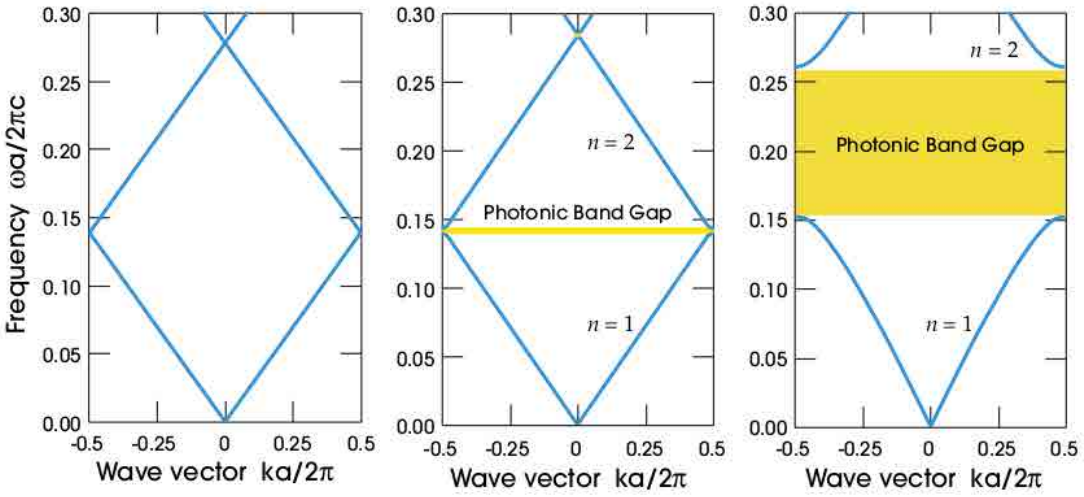


**Figure 2.3:** Photonic band structures computed for $k_z$ propagation. (a) Every layer has the same dielectric constant. (b) Layers alternate between $\varepsilon_r$ of 12 and 13. (c) Layers alternate between $\varepsilon_r$ of 1 and 13. Extracted from[39].

In the first case of an homogeneous medium, modes lie continuously along the light line. As $k_z$ repeats itself outside the Brillouin zone, the light line folds back into the zone when it reaches an edge. In the second case, the nearly-homogeneous medium, presents a photonic band gap for frequencies between the first and the second mode lines. There is no allowed mode in the crystal that has a frequency within this PBG,

regardless of $k_z$. Finally, it is observed in the third case how the bandwidth of the PBG increases considerably with the dielectric contrast increase.

A path to analyze the position of PBG and, therefore, the region of thermal radiation inhibition in PhC, arises from the dispersion relation of plane waves within the crystal.

### 2.1.3 Fresnel's Equations

The electric and magnetic fields, solutions of the Maxwell's equations in a media, are here analyzed in terms of reflectance and transmittance through a change of media. The intensity of light reflected from the surface of a dielectric as a function of the angle of incidence was first obtained by Fresnel in 1827. When an electromagnetic wave strikes the surface of a dielectric, both reflected and refracted waves are generally produced. The angles that the incident, reflected and refracted rays make to the normal of the interface are given as $\theta_i$, $\theta_r$ and $\theta_t$. The relationship between these angles is given by the *law of reflection* and the *Snell's law*:

$$\theta_r = \theta_i \tag{2.20}$$

$$\frac{\sin\theta_i}{\sin\theta_t} = \frac{n_2}{n_1} \tag{2.21}$$

Fig. 2.4 shows an schematic of the described behavior.

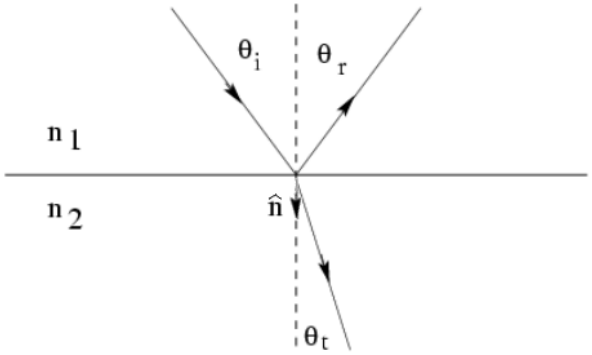


**Figure 2.4:** Relationship between the incident, reflected and refracted angles for an electromagnetic wave in a change of dielectric media.

Two different cases are considered attending to the polarization of incident light: defining the *plane of incidence* as the plane that contains the incident and reflected $k$-vectors, the perpendicular ("S") polarization sticks out the plane of incidence while the parallel ("P") polarization lies parallel to the plane of incidence. The behavior of electromagnetic waves traveling through multiple changes of media is dependent on their polarization.

From the presented *law of reflection* and *Snell's law*, we would like to compute the fraction of a light wave reflected and transmitted by a flat interface between two media with different refractive indexes. It proceeds by considering the boundary conditions at the interface:

$$\hat{n} \times (\mathbf{E}^{(2)} - \mathbf{E}^{(1)}) = 0 \tag{2.22}$$

$$\hat{n} \cdot (\mathbf{B}^{(2)} - \mathbf{B}^{(1)}) = 0 \tag{2.23}$$

Once the Maxwell's equations are solved and the allowed modes are found, we find the following relation for "S" polarized waves:

$$\mathbf{E}_i + \mathbf{E}_r = \mathbf{E}_t \tag{2.24}$$

$$-\mathbf{B}_i \cos\theta_i + \mathbf{B}_r \cos\theta_r = -\mathbf{B}_t \cos\theta_t \tag{2.25}$$

As $\mathbf{B} = n/c \cdot \mathbf{E}$ and $\theta_r = \theta_i$, this gives the following relation:

$$n_1(\mathbf{E}_r - \mathbf{E}_i)\cos\theta_i = -n_2(\mathbf{E}_r + \mathbf{E}_i)\cos\theta_t \tag{2.26}$$

From this expressions, we can find the reflection and transmission coefficients as follows:

$$r_S = \frac{\mathbf{E}_r}{\mathbf{E}_i} = \frac{n_1 \cos\theta_i - n_2 \cos\theta_t}{n_1 \cos\theta_i + n_2 \cos\theta_t} \tag{2.27}$$

$$t_S = \frac{\mathbf{E}_t}{\mathbf{E}_i} = \frac{2n_1 \cos\theta_i}{n_1 \cos\theta_i + n_2 \cos\theta_t} \tag{2.28}$$

These equations are called the Fresnel's equations for perpendicularly polarized light ("S"). For, parallel polarized light ("P"), we can find equivalent expressions:

$$r_P = \frac{\mathbf{E}_r}{\mathbf{E}_i} = \frac{n_1 \cos\theta_t - n_2 \cos\theta_i}{n_1 \cos\theta_t + n_2 \cos\theta_i} \tag{2.29}$$

$$t_P = \frac{\mathbf{E}_t}{\mathbf{E}_i} = \frac{2n_1 \cos\theta_i}{n_1 \cos\theta_t + n_2 \cos\theta_i} \tag{2.30}$$

Reflectance and transmittance, defined as the ratio between the reflected/transmitted power to the incident power is calculated the following way:

$$R_{S,P} = r_{S,P}^2 \tag{2.31}$$

$$T_{S,P} = \frac{n_2 \cos\theta_t}{n_1 \cos\theta_i} t_{S,P}^2 \tag{2.32}$$

These equations can be applied to any system to find reflectance and transmittance coefficients, from which the absorption is obtained in an indirect way following the relation $R + T + A = 1$.

### 2.1.4 Fresnel's Equations & Photonic Crystals

In the simplest case of the multilayer interaction of a light beam impinging a structure like the one presented in Fig. 2.2, reflectance and transmittance of the whole structure are obtained by applying Fresnel's equations at each interface of the multilayer. A reflectance pattern like the one presented in Fig. 2.5 is obtained.

At the wavelength of peak reflectance, constructive interference of light that is reflected from two consecutive interfaces of the structure is obtained when the optical path length difference of the two light rays is equal to $m \cdot \lambda/2$ (where $m$ is a positive integer). The so-called half-lambda configuration:

$$m\frac{\lambda}{2} = d_1\sqrt{{n_1}^2 - \sin^2\theta_i} + d_2\sqrt{{n_2}^2 - \sin^2\theta_i} \tag{2.33}$$

This equation determines the wavelength $\lambda_0$ at which optical constructive interference occurs and reflectance is maximum. The optical response of PhC is therefore

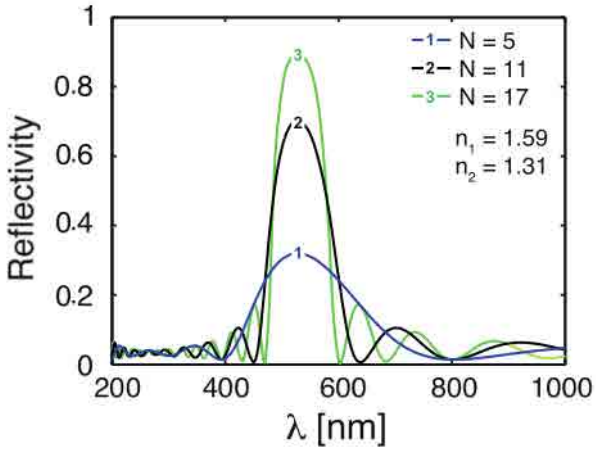


**Figure 2.5:** Calculated reflectivity of a 1D photonic crystal with alternating dielectric layers as a function of the number of layers. Extracted from [74].

determined by the refractive indexes $n_1$ and $n_2$ of the layers, the film thicknesses $d_1$ and $d_2$, and the angle of incidence.

In addition to that, as it is observed in Fig. 2.5, the maximum reflectance of the structure at $\lambda_0$ depends on the number $N$ of repeating pairs of alternating layers. The higher the number of layers, the higher the reflectivity of the photonic structure. Reflectance at $\lambda_0$ is obtained, at normal incidence, applying the following formula:

$$R = \left( \frac{n_{in} \cdot {n_2}^{2N} - n_{out} \cdot {n_1}^{2N}}{n_{in} \cdot {n_2}^{2N} - n_{out} \cdot {n_1}^{2N}} \right)^2 \tag{2.34}$$

where $n_{in}$ and $n_{out}$ refers to the refractive indexes of the surrounding media (= 1 if the crystal is placed in air).

To determine the bandwidth around the peak wavelength $\lambda_0$ for which the structure exhibits the highest reflectivity, it is obtained that the bandwidth $\Delta\lambda_0$ of a photonic stopband at normal incidence can be calculated by:

$$\Delta\lambda_0 = \frac{4\lambda_0}{\pi} \arcsin\left( \frac{n_2 - n_1}{n_2 + n_1} \right) \tag{2.35}$$

This way, by applying Fresnel's equations the position and bandwidth of the photonic stopbands can be theoretically calculated from the geometrical and optical properties of the crystal. Note, however, the reflection properties of light in a media depend

on the light polarization mode and the angle of incidence, as it has been presented in the previous section. As the definition of *Photonic Band Gap* stands for a range of optical wavelengths at which propagation is forbidden (R = 1) for any polarization mode and any angle of incidence on the crystal, analyzing the PBG of a structure through Fresnel's equations requires a recursive analysis for all angles of incidence and light polarization modes.

### 2.1.5 Numerical Analysis

The simple case of 1D PhC was analyzed in previous sections presenting analytical solutions for Maxwell and Fresnel's equations. Such calculations become much more complex when 2D and 3D periodic structures are considered. In those cases, computational analysis is essential to solve the band diagram of the structures and analyze the reflectance and transmittance properties.

Predicting the optical properties of photonic materials is one of the key issues in photonics. Numerical methods are usually divided in two main categories, namely time and frequency domain methods. Among time domain, the most powerful and widely used is the Finite Differences Time Domain (FDTD) method.[75] Here, the space is discretized in a suitable grid, the so-called Yee lattice, where electric and magnetic field components of the Maxwell's equations are explicitly calculated. Its accuracy is limited only by computational resources and time, and it is among the few methods allowing to include nonlinear effects. The main drawback of this method is the extensive computational resources needed to accurately solve problems so that the whole simulation volume must be discretized.

On the other hand, the scattering matrix relates the incoming fields expressed as a superposition of plane waves with the fields scattered by the system in a given direction. The transition matrix is the function relating the incoming and outgoing scattered fields in a given basis. Then, there exist several widely used frequency domain methods to solve Maxwell's equations based on the these matrices. Fresnel's coefficients are utilized in these methods.

The scattering matrix, T-Matrix and transfer matrix[76–78] methods have been successfully used in a variety of large-scale numerical computations. These methods can include both evanescent and propagating waves.[79] One advantage of these methods is

its speed and efficiency. Nevertheless, if the simulated system possesses a large spatial structure, the number of basis elements needed to reach a given accuracy may be large.

In the case of perfect PhC, the full solution of the Maxwell's equations is suitably found in the frequency domain as the solution of an eigenvalue problem. A widely used method is based on an iterative solver of Maxwell's equations in the frequency domain in a plane wave basis by making use of the Floquet-Bloch theorem.[80] This method is suitable for obtaining the dispersion relations of the crystal as well as its associated eigenfunctions.

It is worth mentioning that there is no general purpose method suitable for any kind of problem within the available simulation techniques. During the realization of this thesis, several available software modules have been utilized to characterize the properties of designed structures. MEEP is an open source FDTD code based package from the MIT. It provides a general purpose method to solve complex emission and transport problems in the time domain and obtain the reflectance pattern of the analyzed structures. A complementary code that uses the Plane Wave Expansion (PWE) method, provided by the same research group, is known as MPB. This package was used to calculate the dispersion relation of perfect (infinite and non-deffect) PhC in 3D. Finally, a code based on T-Matrix Method (TMM), home-developed, was used to solve problems involving light scattering in finite (and also deffect-included) photonic structures and obtain the reflectance, transmittance and absorption responses.

## 2.2 Thermal Radiation

So far, it has been presented how to solve Maxwell's equations in the particular case of PhC to obtain the dispersion relation and the reflectance/transmittance patterns of the optical structures. The dispersion relation gives us direct information about the spectral position and bandwidth of the PBG. On the other hand, Fresnel's equations allow us obtaining the reflectance, transmittance and absorption patterns. From them, spectral emittance is obtained in an indirect way, as it is equal to absorption as stated by the *Kirchhoff's law of thermal radiation*:

*"For a body of any arbitrary material, emitting and absorbing thermal electromagnetic radiation at every wavelength in thermodynamic equilibrium, the ratio of its emissive power to its dimensionless coefficient of absorption is equal to a universal function only of radiative wavelength and temperature, the perfect black-body emissive power."*

The dimensionless coefficient of absorption, or absorptivity, is the fraction of incident light that is absorbed by the body when it is radiating and absorbing in thermodynamic equilibrium. In slightly different terms, the emissive power of an arbitrary opaque body of fixed size and shape at a definite temperature can be described by a dimensionless ratio, called emissivity, the ratio of the emissive power of the body to the emissive power of a black body of the same size and shape at the same fixed temperature.

With this definition, a corollary of Kirchhoff's law is that for an arbitrary body emitting and absorbing thermal radiation in thermodynamic equilibrium, the emissivity is equal to the absorptivity. Therefore, during this thesis we will talk equivalently about materials' emissivity and absorptivity.

Kirchhoff's law has another corollary: emissivity cannot exceed one because the absorptivity cannot, by conservation of energy. It is not possible to thermally radiate more energy than a theoretical black body at equilibrium.

Emittance is the relative ability of a body's surface to emit energy by radiation. It is the ratio of energy radiated by a particular material to the energy radiated by a BB at the same temperature. A true BB would have $\epsilon_{BB} = 1$, $\forall\lambda$, while any real object shows $\epsilon(\lambda) < 1$. The radiated power of the thermal source (PhC in these cases

of study) is obtained from the emittance as a function of the surface temperature and the surface area ($\sigma_{sb}$ refers to the Stefan-Boltzmann constant, $5.67 \cdot 10^{-8}$ W/m$^2$K$^4$):

$$P = \sigma_{sb} \epsilon A T^4 \tag{2.36}$$

### 2.2.1 The Black-Body Radiation

A BB is defined as a body that absorbs all incident radiation whatever the wavelength, polarization or incident angle. Thus, a BB neither reflects nor transmits radiation, making it a perfect emitter as it must emit all energy that it absorbs.

No materials behave exactly as a BB. However, materials such as carbon black, platinum black or SiC approach the BB radiation.

To determine the dependence of the BB's spectral emissive power with temperature, the quantum theory developed by Max Planck must be introduced.[81] The emissive power of a BB is described as follows:

$$e_{BB}(\lambda, T) = \frac{2\pi hc^2}{\lambda^5} \cdot \frac{1}{e^{hc/\lambda kT} - 1} \tag{2.37}$$

where $h$ is the Planck's constant ($6.6262 \cdot 10^{-34}$ Js), $k$ the Boltzmann's constant ($1.38 \cdot 10^{-23}$ J/K) and $c$ the vacuum speed of light (299792458 m/s).

The spectral distribution of BB emissive power described by equation 2.37 was already shown in Fig. 1.2. Two important features must be pointed out:

- The wavelength for maximum $e_{BB}(\lambda)$ shifts to lower wavelengths with increasing temperature.
- The total emitted power at all wavelengths (i.e. curve's integral) increases with temperature.

This way, the wavelength of the peak of the BB radiation curve gives a measure of the temperature.

As already stated, for a given body at a given temperature, the BB spectral emissive power $e_{BB}(\lambda, T)$ is the maximum possible that can be achieved. This considers all angles of radiation. At the same temperature, all other emitting surfaces will produce a lower power. Therefore, the spectral emittance $\epsilon$ is defined as:

$$\epsilon(\theta, \phi, \lambda, T) = \frac{e(\theta, \phi, \lambda, T)}{e_{BB}(\theta, \phi, \lambda, T)} \leq 1 \tag{2.38}$$

When the spectral emittance of a body is constant (and $\leq 1$) for all wavelengths (or photon energies) this is known as *gray body* material.

### 2.2.2 Selective Emission

Selective emission stands for materials whose spectral emittance is not constant at all wavelengths (as gray bodies) but concentrated at particular spectral regions. The interest in using selective emitters as thermal sources relies in controlling the spectral position where the emission is concentrated. Now it is clear the main idea is inhibiting thermal radiation above $\lambda_g$ of the PV cell's semiconductor, and maximize it in a region slightly below $\lambda_g$, where the PV cell is more efficient:[82]

$$\epsilon_{SE} = \begin{cases} \epsilon_{BB} & (\lambda \sim \lambda_g) \\ 0 & (\lambda > \lambda_g) \end{cases} \tag{2.39}$$

The selective emission is therefore characterized from the emittance properties of the structures which must be controlled to reach, ideally, the behavior described in equation 2.39.

As commented, by tailoring the photonic DOS, we can effectively control the emission of active media. Spontaneous emission spectra in selective emitters present not only a suppression of radiation in the PBG regions but emission enhancement in the surroundings of the gaps.[61,83] Such complex behavior has been attributed to the strong spectral and angular redistribution of the DOS due to the periodic modulation of the refractive index.

# 3

# Fabrication and Characterization Techniques

This chapter describes the electrochemical etching technique utilized for the fabrication of macroporous silicon structures. The fundamentals of the technique are given together with a description of the physical parameters that govern the stable growth of modulated pores in silicon. Then, various post-fabrication processes are presented deemed to enhance the optical properties of the silicon-based structures.

The chapter is also devoted to the different optical setups utilized to fully characterize the response of the fabricated selective emitters, and the thermal stability tests. Especial attention is given to the house-made high temperature characterization setup as it has been developed in the framework of the present work.

## 3.1 Macroporous Silicon

Three-dimensional macroporous silicon PhC are fabricated by light-assisted electrochemical etching of $n-$type silicon in Hydrofluoric Acid (HF) solution. Pore distribution is defined on the surface of the silicon wafer by lithography; then, the modulation of pore diameter in depth is accomplished by controlling the infrared illumination which is focused to the semiconductor to activate its dissolution in the acid. Fig. 3.1 shows some examples of the structures that are obtained.

The physics of macropore formation under illumination, the process sequence and the sample preparation features are detailed in the following sections.

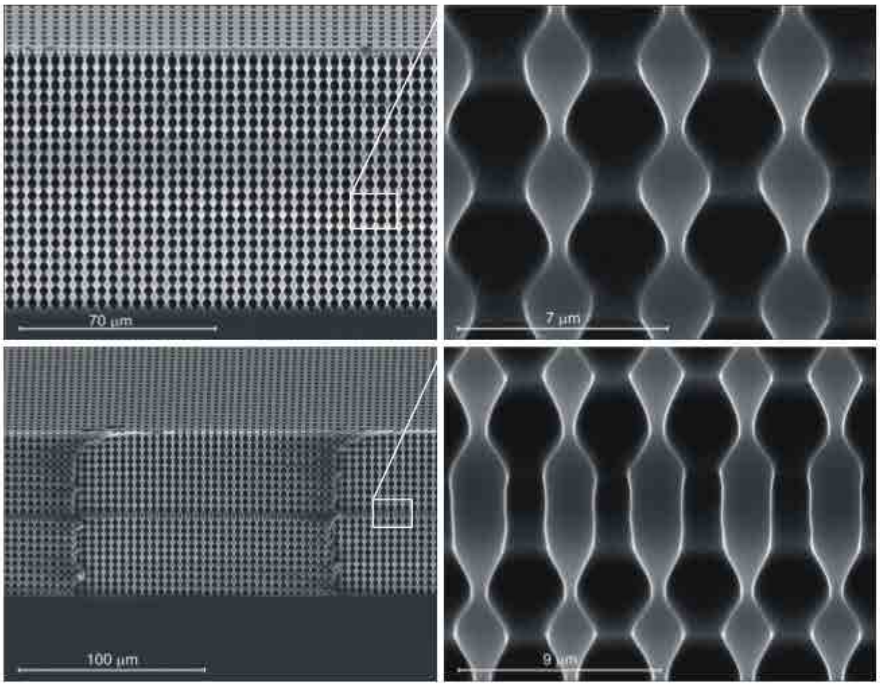


**Figure 3.1:** SEM images of photonic structures based on mp-Si fabricated by electrochemical etching of silicon in HF solution.

### 3.1.1 The Semiconductor-Electrolyte Interface

Semiconductor-electrolyte systems behave, at first approximation, the following way: at the semiconductor-electrolyte interface, two parallel layers of charge develop, one at each side of the interface and with opposite signs, forming a rectifying potential barrier similar to that of a Schottky diode[84] (metal-semiconductor contact), except that any charge transfer across the semiconductor-electrolyte interface involves a chemical reaction. Ions in the electrolyte approach the surface of the semiconductor as close as possible. On the other hand, charge present in the semiconductor is due to majority and minority carriers, and ionized dopants.

Opposite to electrons and holes, the ionized doping atoms in the semiconductor bulk are not mobile charges and, therefore, free carriers present in the semiconductor's interface come from the generated electron-hole pairs. In the case when the sign of the potential applied to the semiconductor is such that the majority carriers are drawn away from the interface and into the bulk, and the minority carriers are the ones present in the interface, this system forms a Space Charge Region (SCR) that extends up to

several tenths of microns or even more into the bulk of the semiconductor, depending on the doping concentration. In the physics literature, this is termed the *reverse bias* situation.

In silicon, the reverse bias is obtained when a positive potential is applied to $n-$type Si and, equivalently, a negative potential is applied to $p-$type Si. It is worth mentioning that under *forward bias* the SCR into the semiconductor would be much more reminiscent than that of reverse bias.

Hence, the current-voltage (I-V) characteristic of the silicon-electrolyte contact is approximated to the one of the Schottky diode. However, the I-V characteristic of the real Si-electrolyte interface exhibits features beyond that simple model. The I-V curve is shown in Fig. 3.2 and can be divided into four regions:

- In the cathodic regime, for both $n-$ and $p-$type material, silicon is normally stable, i.e. it does not dissolve. Under cathodic conditions, current in $p-$type silicon is is proportional to light intensity. In $n-$type Si there is no illumination effects in the I-V characteristic.

- In the anodic regime, current in $p-$type Si increases exponentially with increasing potential, while $n-$type Si requires the effect of the illumination to reach the same behavior. In these cases, current exhibits an $I_{ps}$ peak in the curve. This characteristic current peak is assumed to divide the experimental conditions into two domains: porous silicon formation and electropolishing.

- At anodic potentials below the potential of $I_{ps}$, silicon is considered to dissolve through direct transfer of Si atoms into the electrolyte, as remaining silicon between pores retains its original crystallinity. It is this region where porous silicon formation occurs.

- At anodic potentials above the potential of $I_{ps}$, the dissolution is thought to proceed through the formation of an intermediate oxide layer. The chemical reaction proceeds in two steps, first the electrode is anodically oxidized, and then the oxide is chemically dissolved in the electrolyte.[85–87] This finally results in electropolishing of the silicon surface.

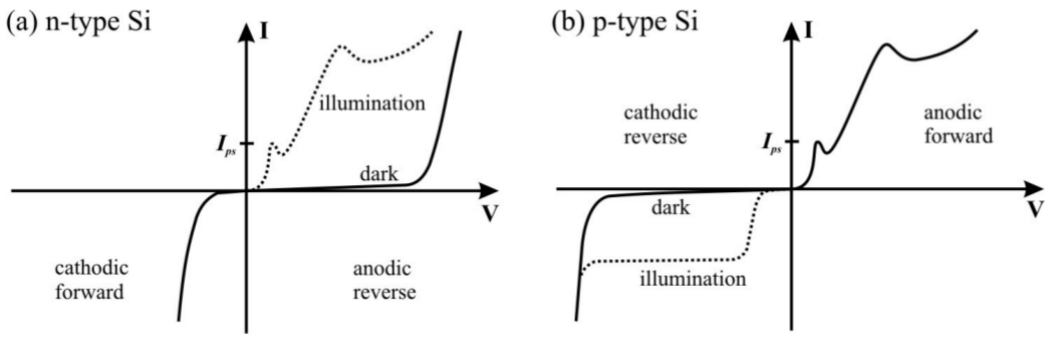


**Figure 3.2:** Typical current-voltage (I-V) characteristics for (a) $n-$type and (b) $p-$type silicon. The solid and dotted lines indicate the dark response and response under illumination, respectively. Extracted from [88].

### 3.1.2 The Lehmann's Model

Based on the previously presented semiconductor-electrolyte system, the basic assumption of the Lehmann's model[88] is that the macropore formation in low doped $n-$type silicon depend critically on whether the diffusion of reactants in the electrolyte or charge supply from the electrode is the rate-limiting step. In other words, the fundamental assumption in the Lehmann's model is that the current density at pore tips ($J_{tip}$) equals, for stable pore growth, the critical value $J_{ps}$.

At current densities higher than $J_{ps}$, the dissolution reaction is limited by the supply of reagents through diffusion in the electrolyte and a surface charge of excessive holes builds up. Silicon's surface is more exposed to the electrolyte and dissolves faster, which results in smoothening of the electrode surface (electropolishing).

At current densities below $J_{ps}$, every hole reaching the surface will be immediately consumed in the dissolution reaction. As electric field lines focus to surface dips, the dissolution is enhanced there, leading to pore formation, as illustrated in Fig. 3.3. The backside illumination generates electron-hole pairs in the bulk of the semiconductor. The holes diffuse through the wafer and reach the Si-electrolyte interface where they are consumed in the dissolution reaction. The holes do not penetrate the area between the pores, they are focused by the SCR mainly at the pore tips. This way, only the tips are electrochemically active while pore walls remain passivated against dissolution.

Based on the assumption $J_{tip} = J_{ps}$, Lehmann proposed a simple formula that relates the diameter of the pores with the applied current density in the system $J$. The

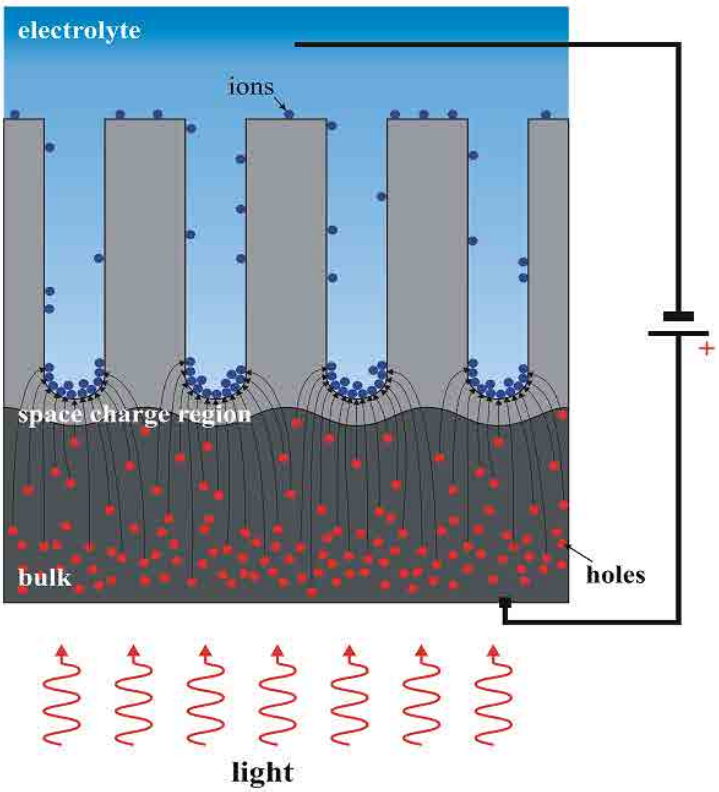


**Figure 3.3:** Schematic illustration of the macropore formation in low doped n-type Si. Extracted from[52].

etching current $I$ is the current density $J$ multiplied by the surface area of the pores ($A_{pores}$, the contact area between the silicon and the electrolyte). At the same time, as all charge transfer occurs via the pore tips, the etching current $I$ is the product of $J_{tip} = J_{ps}$ by the cross-sectional area of the pores $A_{cross-section}$:

$$I = J \cdot A_{pores} = J_{ps} \cdot A_{cross-section} \tag{3.1}$$

Let's consider first the case of cylindrical pores for simplicity: $A_{cross-section}$ is a constant value in depth, as well as $J_{ps}$, this last defined by the properties of the Si bulk and the electrolyte. As a consequence, the product $J_{ps} \cdot A_{cross-section}$ will be a constant value, forcing the current density of the system $J$ to decrease as the etching goes on and the porosity of the structure $A_{pores}$ increases. This behavior is presented in Fig. 3.4.

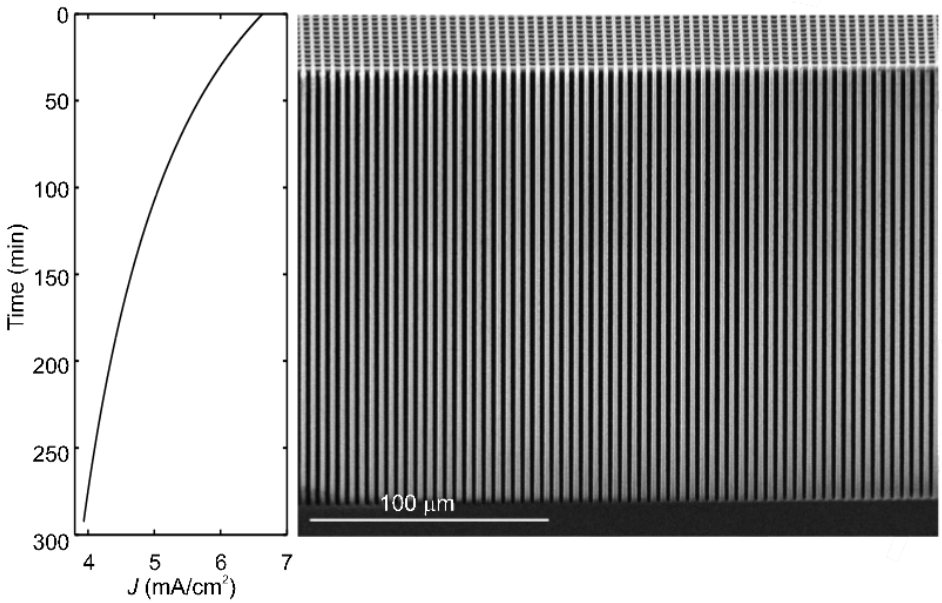


**Figure 3.4:** Current profile required to obtain a 2D array of pores with constant diameter.

Note $A_{pores}$ depends on time, increasing as the etching progresses, and $A_{cross-section}$ depends on the diameter of the pores at each depth. Hence, the above equation relates the pore diameter $d$, at each pore depth $L$, with the system's current density $J$, at each instant of time $t$. This way, the pore diameter $d(L)$ can be modulated in depth by controlling $J(t)$.

The relationship between $L$ and $t$ is found experimentally following a first, second or third order polynomial model to fit the growth rate. In addition, $J_{ps}$ is experimentally found depending on the HF concentration and absolute temperature of the electrolyte, moreover, $J_{ps}$ depends also on crystal direction and doping level of the silicon bulk.

To clarify the concept, Fig. 3.5 shows the dependency between pore diameter and the applied current density $J$ in the system with a fixed potential $V_{ps}$. It is observed how the system can be adjusted to reach any point of the hatched region.

As a final remark, it is worth mentioning that Lehmann's formula is only applicable to macropore formation in $n-$type Si with backside illumination with an applied potential above $V_{ps}$. Therefore, from the Lehmann's formula, the particular etching conditions that models the pore growth in every particular test case must be found experimentally, based on temperature conditions, electrolyte concentration, and the particular properties of the Si bulk.

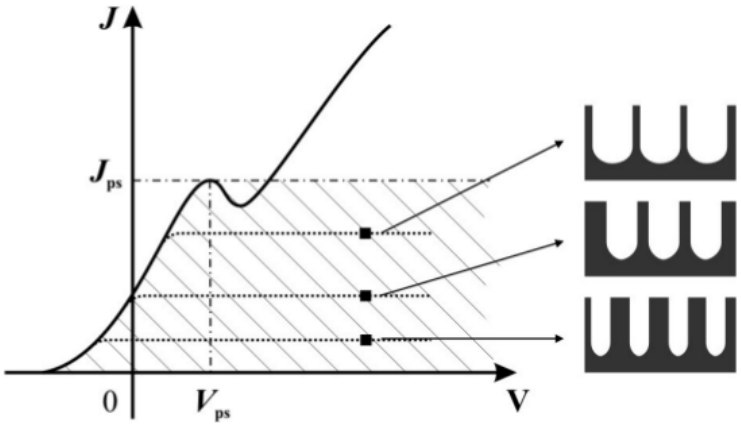


**Figure 3.5:** I-V characteristic of illuminated $n-$type Si electrode in aqueous HF solution. The dependency of pore diameter with applied $J$ is depicted. Extracted from[88].

### 3.1.3 Sample Preparation

If a flat, polished Si wafer is anodized in HF electrolyte, pores grow randomly across the silicon surface, with average pore diameters and spacing depending on the applied current and substrate resistivity. To get ordered pores we first need to prepare the sample to mark where pores should grow.

The simplified process sequence is given in Fig. 3.6. First, wafers are oxidized in order to grow a thin oxide film to act as a mask in a later anisotropic etch of silicon in Tetramethylammonium Hydroxide (TMAH) solutions. Standard photolithography is used to pattern the oxide layer with a square distribution of 2 $\mu$m pitch (1 $\mu$m resolution). The lithographic pattern is transferred into the oxide layer by Reactive Ion Etching (RIE) technique, and the patterned wafer is immersed in TMAH solution to make the defect sites onto the silicon surface. The TMAH etch is an anisotropic process, it means the resulting structure is a lattice of pyramidal notches (see Fig. 3.6) that serve as seeds for the pore growth. Afterwards, the oxide layer is removed by a short dip in HF.

Previous to all this process, an ohmic contact is created on the wafer backside to contact the samples electrically during the electrochemical etching. This is created by wafer implantation of a thin $n+$ layer. The implantation process strongly affects the crystalline character of bulk Si, and so the mobility of minority carriers and their lifetime. The crystalline properties are recovered during the initial oxidation step of sample

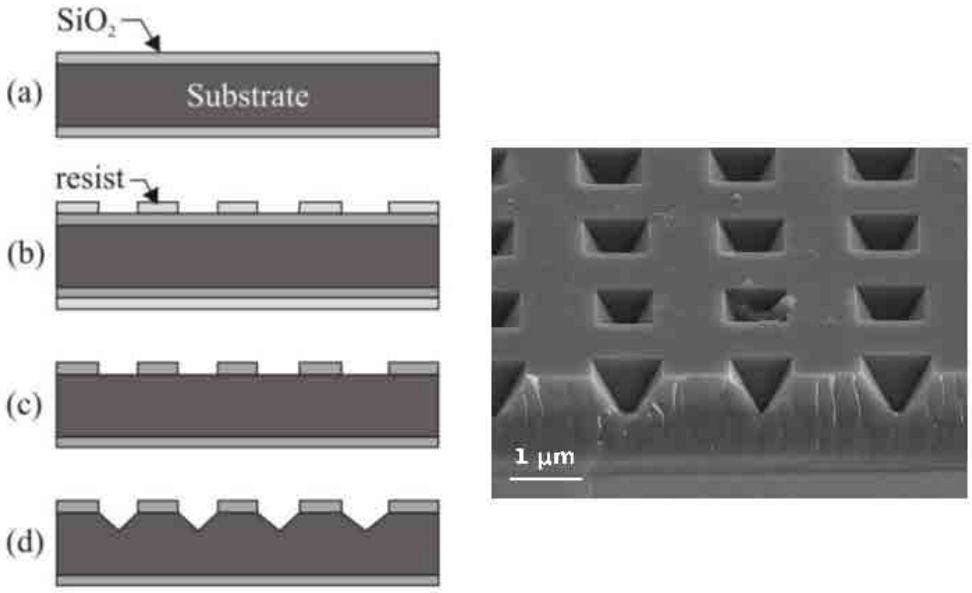


**Figure 3.6:** Main process sequence for sample preparation: (a) wafer oxidation; (b) photolithography; (c) window opening in the oxide film by dry etch; and (d) TMAH etch of the silicon to form pyramidal notches.

preparation thanks to the high temperature treatment (1040 °C for ∼90 minutes).

The prepared samples are clamped into the electrochemical etching setup where the patterned wafer side is in contact with the electrolyte (HF) and the wafer's backside is illuminated to generate the electron-hole pairs. The I-V of the system is controlled by a computer's program that defines the pores' shape as a function of time and depth.

The electrochemical set-up used for the growth of macropores is home-made and specifically designed for this purpose. The most important element is the electrochemical cell where the chemical reaction takes place. The cell is made of PVC, which is a material resistant to HF at low concentrations and can be easily mechanized. It is designed to process samples of 2.5x2.5 cm, with an area exposed to the electrolyte of 2.6 $cm^2$ (circular). A tightly packed array of LEDs is used for illuminating the backside of the sample, providing homogeneous generation of electron-hole pairs in the samples' backside. Fig. 3.7 shows an schematic of the electrochemical cell.

The starting material is $n-$type (phosphorus doped) Si wafers with (100) orientation and resistivity 0.5-0.6 Ωcm ($10^{16}$ $cm^{-3}$ doping level). It is worth mentioning that the resistivity (doping level) of the bulk is chosen attending to the desired period of pore

distribution (2 $\mu$m period). Smaller pore sizes require lower resistivities while bigger structures need higher resistivity samples. Wafers' thickness is between 350-380 $\mu$m in 4-inch wafers. Only CZ (Czochralski grown) wafers were used during the realization of this thesis as the quality of the material was enough for our purposes.

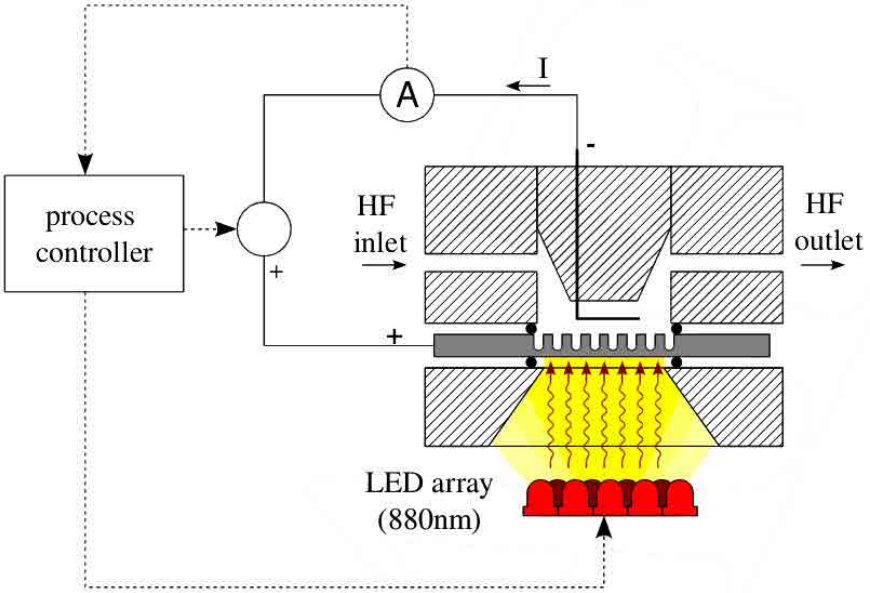


**Figure 3.7:** Schematic of the electrochemical etching cell.

## 3.2 Further Processing

Macroporous silicon allows the definition of a wide variety of photonic structures with independence among $\hat{\mathbf{x}}$, $\hat{\mathbf{y}}$, and $\hat{\mathbf{z}}$ crystal directions. However, silicon is the base material in all cases.

### 3.2.1 Pore Widening

As it was observed in Fig. 2.3, the dielectric contrast plays one of the most important roles in the definition of the optical properties of PhC (i.e. the maximum contrast will span the bandwidth of PBG). The dielectric contrast of originally etched mp-Si crystals can be increased by increasing the porosity of the structure. This is accomplished by isotropic pore wall erosion through a cyclic process of thermal oxidation and subsequent oxide-removal. This simple technique progressively widens the diameter of the pores by consuming Si atoms during the oxidation process and dissolving them when the $SiO_2$ layer is etched.

As the electrochemically etched structures do not present real three dimensional character, due to the smooth initial $\hat{\mathbf{z}}-$modulation, through a pore widening process the initial Si crystal is improved, achieving 3D character by making the pores interconnect laterally at their diameter maxima. The final widened structure resembles a 3D array of air bubbles embedded in silicon. Fig. 3.8 shows two mp-Si structures previous and after a pore widening process to illustrate the results.

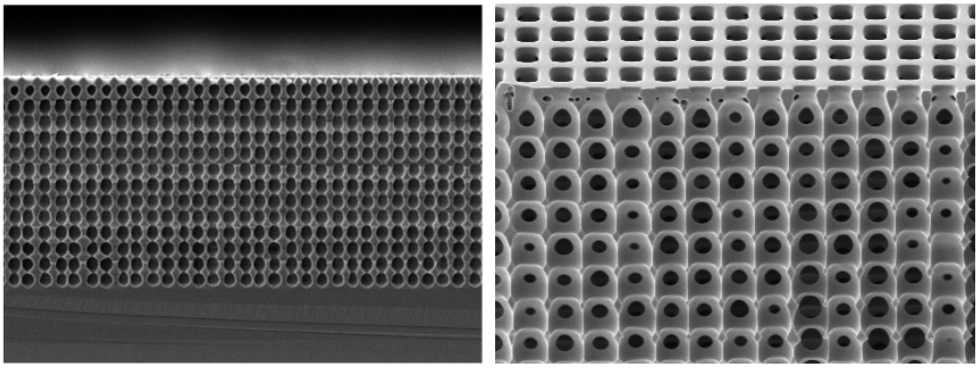

**Figure 3.8:** Original and resulting structures after the pore widening process.

The consumption of silicon in each oxidation cycle is around 44% of the grown oxide layer.[88] The typical number of cycles of oxidation and oxide-removal to achieve

three-dimensionality in the crystals was 4-5. The oxidation process was carried out in dry $O_2$ atmosphere at 1040 °C for 90 minutes. A thin high-quality conformal oxide layer growed under these conditions.

### 3.2.2 Multilayering Techniques

The optical response of the fabricated PhC depends entirely on the intrinsic properties of the present materials. This represents an enormous limitation in the case of mp-Si structures as silicon is always the base material. Various deposition techniques were studied to coat the original Si structure with dielectric materials and metals to take profit of the optical properties of the deposited layers.

The coating techniques used during this thesis were the following:

- *Thermal oxidation.* A $SiO_2$ layer is obtained by thermal oxidation of the original mp-Si structures in a furnace with $O_2$ atmosphere at 1040 °C for few minutes (5-30 minutes).

- *ALD.* Atomic Layer Deposition is a thin film deposition technique that is based on the sequential use of a gas phase chemical process. The process works with different gas chemicals, the so called precursors, which react with the sample's surface one at a time, depositing atomic layers. The thin film grows with extremely accurate rate control.

- *Sputtering.* This process consists in bombarding a solid target of material by high energy particles to eject material from the target and deposit it on the samples' surface. This process does not reach a conformal coating of the 3D structure, but it only coats its surface.

## 3.3 Optical Characterization

The optical properties of PhC are characterized through reflectance, transmittance and emittance measurements along the NIR and MIR spectral regions by Fourier Transform Infrared (FTIR) spectroscopy.

Reflectance and transmittance measurements were taken at room temperature in all cases. Thermal emittance was characterized by direct measure of the samples' radiation at different temperatures, comparing this radiation with that from a BB source at the same temperatures to calibrate the measure.

### 3.3.1 The Michelson Interferometer

The goal of any spectral characterization technique is to measure *how well* a sample reflects, transmits or absorbs light as a function of frequency. The most straightforward way to do this would be to illuminate the sample with infinite monochromatic light beams and measure the optical response for each beam. Fourier transform spectroscopy is a less intuitive but practical way to accomplish the same objective.

The working principle of the FTIR spectrometer is the Michelson interferometer.[89] In it, a broadband input light beam is divided into two halves at a beam splitter. Each half travels a different path, one fixed and one variable, before being reflected back to the beam splitter. When the two halves of the beam reencounter, they interfere due to the path difference. The result of the interference is directly related to the path difference at a particular light frequency. An schematic is presented in Fig. 3.9.

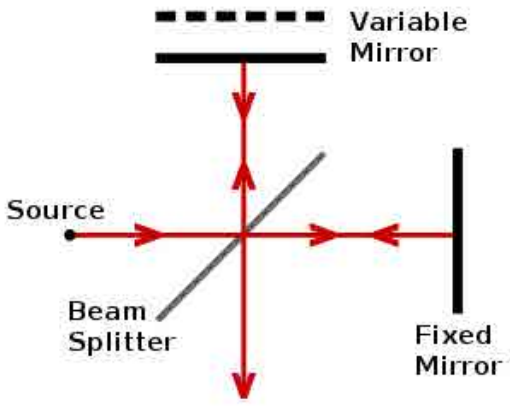


**Figure 3.9:** Michelson interferometer diagram.

The FTIR spectrometer calculates the interferogram of the sample's incoming light for the available set of path differences. The read power is obtained as a function of frequency by Fourier transform of the interferogram.

The optical characterization of the samples was performed using a Bruker Vertex 70 FTIR spectrometer. In both NIR and MIR spectral measurements, various sources, detectors and beam splitters were used. A *Globar source* (consisting in a SiC rod electrically heated up to ∼1500 K) with a KBr beam splitter and a DLaTGS detector were used for MIR characterization between 2.5 and 25 $\mu$m wavelength. Measurements at lower wavelengths between $1 - 15$ $\mu$m were performed utilizing a tungsten lamp as light source and a $CaF_2$ beam splitter with an MCT detector. In addition, a silicon photodetector was used to characterize the samples from 0.7 to 1 $\mu$m wavelength in the NIR.

The Bruker spectrometer was used to study the reflectance and transmittance properties at room temperature. Transmittance was directly read by measuring the amount of light passing through the samples and relating the measure to the source signal. These characterization showed the transmittance of the fabricated samples was negligible at the studied spectral range due to the thickness of Si and its doping level. Transmittance measurements became therefore superfluous.

Reflectance was a bit more complex characterization considering that the surface of the samples were microstructured in order to, indeed, affect the photon motion on the structure. Two classes of techniques were required to fully characterize the reflectance properties: specular and diffusive measurements. The specular reflectance setup consists in an angle resolved tool capable to read the reflection of samples from 13° to 83°. Diffusive reflectance measurements required the use of an integrated sphere with a dedicated detector. The integrated sphere is coated in gold to obtain maximum reflection (minimum absorption) at IR wavelengths.

During the characterization, reflectance was obtained as a function of light polarization and incident angle. Fig. 3.10 shows an schematic of the measure for both TE, or s-polarized light, where the electric field is contained in the plane perpendicular to the pores direction, and TM, or p-polarized light, where it is the magnetic field the one contained in the perpendicular plane.

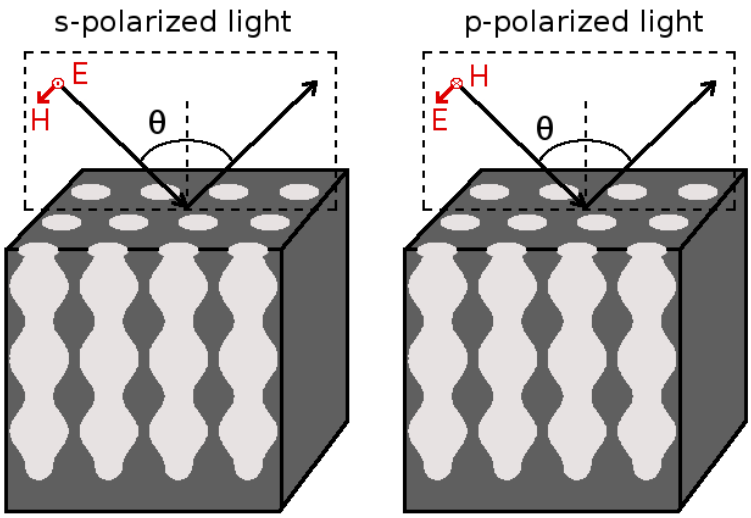


**Figure 3.10:** Schematic of the reflectance characterization for TE and TM polarization modes and as a function of the incident angle.

### 3.3.2 Direct Thermal Emission

As it has been already stated, the emittance properties of the fabricated samples can be advanced by indirect calculation from room-temperature reflectance and transmittance measurements. However, as optical properties of materials may change with temperature, an accurate and reliable characterization of the thermal radiation properties lies on direct emission measurements of the radiated energy when samples are at high temperatures.

Emittance measurements were obtained by coupling to the Bruker's FTIR spectrometer the high-temperature angle-resolved setup. The setup heats the samples up to 800 °C (1073 K). Any lower temperature can be programmed in the setup. The radiation emitted by the samples' surface is then focused into the interferometer by an optical system of gold mirrors.

Fig. 3.11 shows an schematic of the direct thermal emission setup coupled to the Bruker's spectrometer (see more details in Appendix B). At the focal plane of the spectrometer's mirror $M_1$ there is a diaphragm $D$ with controllable aperture. The size of this aperture determines the area over the sample's surface that is characterized. At 50 cm of the diaphragm there is a concave gold mirror $M_2$ with focal length $f = 25$ cm. The optical system is completed with a plane gold mirror $M_3$ that redirects the

radiation coming from the hot sample to the concave mirror. The distance between the sample and the concave mirror, through the plane mirror, is also 50 cm.

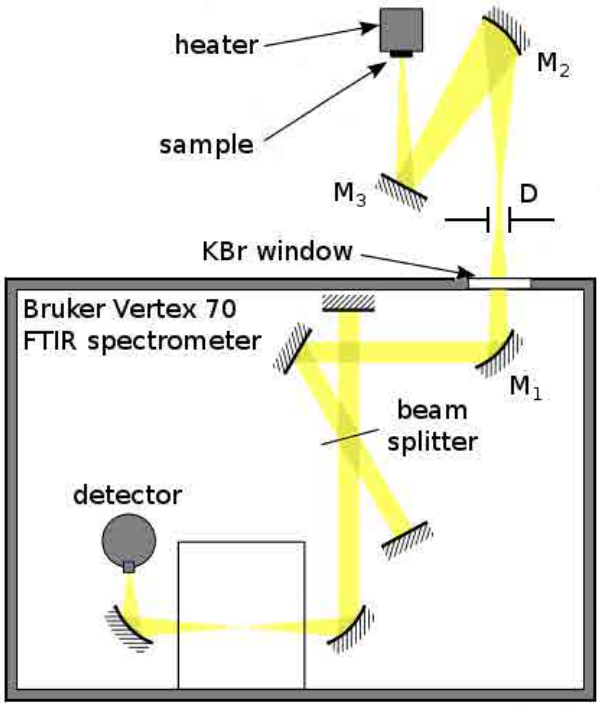


**Figure 3.11:** Schematic of the high temperature characterization setup. The heating setup is located outside the FTIR spectrometer. Samples' radiation is derived to the interferometer by an optical system of gold mirrors.

Note the distance between the samples and the concave mirror, and between this and the diaphragm, is two times the focal length of the mirror. This $2f - 2f$ configuration guarantees that the image of the emitting surface which incomes the FTIR spectrometer is not magnified and that the measured area on the samples' surface can be controlled by the aperture of the diaphragm.

On the other hand, the heating element is a Nickel-Chromium resistance electrically fed by Joule effect. A metallic plate is placed on the resistance to uniform the generated heat. Samples are clamped onto it. Angle measurements can be performed thanks to the assembly of the heater to a rotation platform (see pictures in Appendix B).

It is worth noting how the accuracy of the optical analysis strongly depends on the Signal to Noise Ratio (SNR) in the detector. Measure's accuracy dramatically reduces when approaching lower wavelengths if the temperature of the source is not high enough

to generate enough optical power at those wavelengths. The accuracy and reliability of the obtained direct thermal emission measurements is therefore limited by the sample's temperature. Within our setup capable to work up to 1073 K, the minimum spectral range of characterization is 1 $\mu$m wavelength.

#### Measure Calibration

The emission spectra directly obtained are not useful as they are strongly affected by the atmospheric absorption (mainly from water vapor and $CO_2$) and the background radiation. Also, several of the elements that conform the optical path, such as the detector or the beam splitter, are not linear elements, and their detectivity and efficiency depend on the frequency of incoming light. Consequently, calibration is necessary in order to compensate these effects and obtain an accurate emittance characterization.

Calibration consists in determining the instrument's response considering the non-linearity of its components and the background radiation. This is accomplished by measuring the known radiation of a BB system (IR-519, developed by Infrared System Corporation) with $> 0.99$ emittance from 0.5 to 99 $\mu$m wavelength. The BB source is placed at the same point as the samples for the calibration. The obtained measure, compared with the theoretical radiation of a BB thermal source at a given temperature, allows to determine the instrument's response.

### 3.3.3 Thermal Stability Tests

Thermal stability tests were conducted in two phases: a characterization phase and a thermal treatment phase. During the characterization phase, samples were clamped onto the heating setup, were heated and their thermal radiation was spectrally analyzed with the FTIR spectrometer at different temperatures. The heating up / cooling down ramps were 15 °C/min. The time the samples were at high temperature during characterization varied from few minutes to hours depending whether an angle-resolved characterization was performed or not.

During the thermal treatment phase, samples were left in a muffle oven, or a furnace, with controlled atmosphere (air, $N_2$ and vacuum) for 10 to 12 hours. The thermal treatment was conducted at different temperatures up to 1200 °C to study the integrity of the structures. Then, samples were characterized again to test the stability of the optical response after the thermal treatment. Heating ramps were also 15 °C/min.

## 3.4 Macroporous Silicon Structures

The work on macroporous silicon is based on the previous research group's experience.[52,53,55,56,90–93] Here we present a summary of the main achievements.

There is a limited variety of pore shapes that can be attained by electrochemical etching itself. In order to produce periodically arranged macropore arrays, Si wafers must be pre-structured prior to the etching to determine the nucleation sites where the pores should grow. This is done by lithography. Then, the patterned side of the wafer is exposed to the electrolyte during the electrochemical etching while wafer's backside is illuminated to generate the required electron-hole pairs. Fig. 3.12 shows SEM images of 2D square macropore array. The observed markers are used to measure the growth rate and thus, obtaining the necessary information for optimizing the etching process.

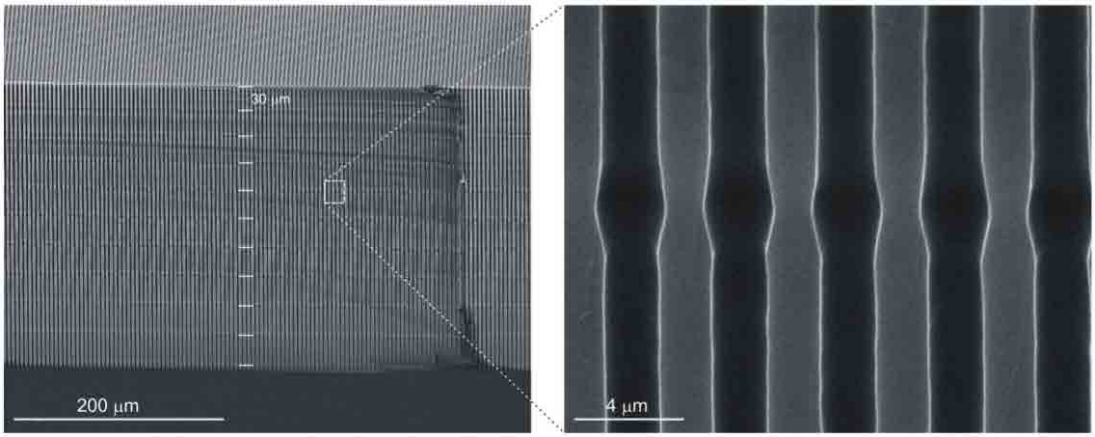


**Figure 3.12:** SEM images of electrochemically etched macropores. Pores, with a depth of 305 m, are distributed along a square pattern of 4 m pitch.

Fig. 3.12 suggests that pore diameter can be periodically modulated along the growing direction. This is a remarkable feature of the photo-assisted electrochemical etching process. As it was described in section 3.1, increasing the backside illumination intensity we cause a higher hole generation rate, which results in a greater etched pore diameter. To achieve periodic modulation of pore diameter, the light intensity must be varied periodically during pore growth. Fig. 3.13 shows some examples of modulated macropore arrays together with the correspondent etching current profile.

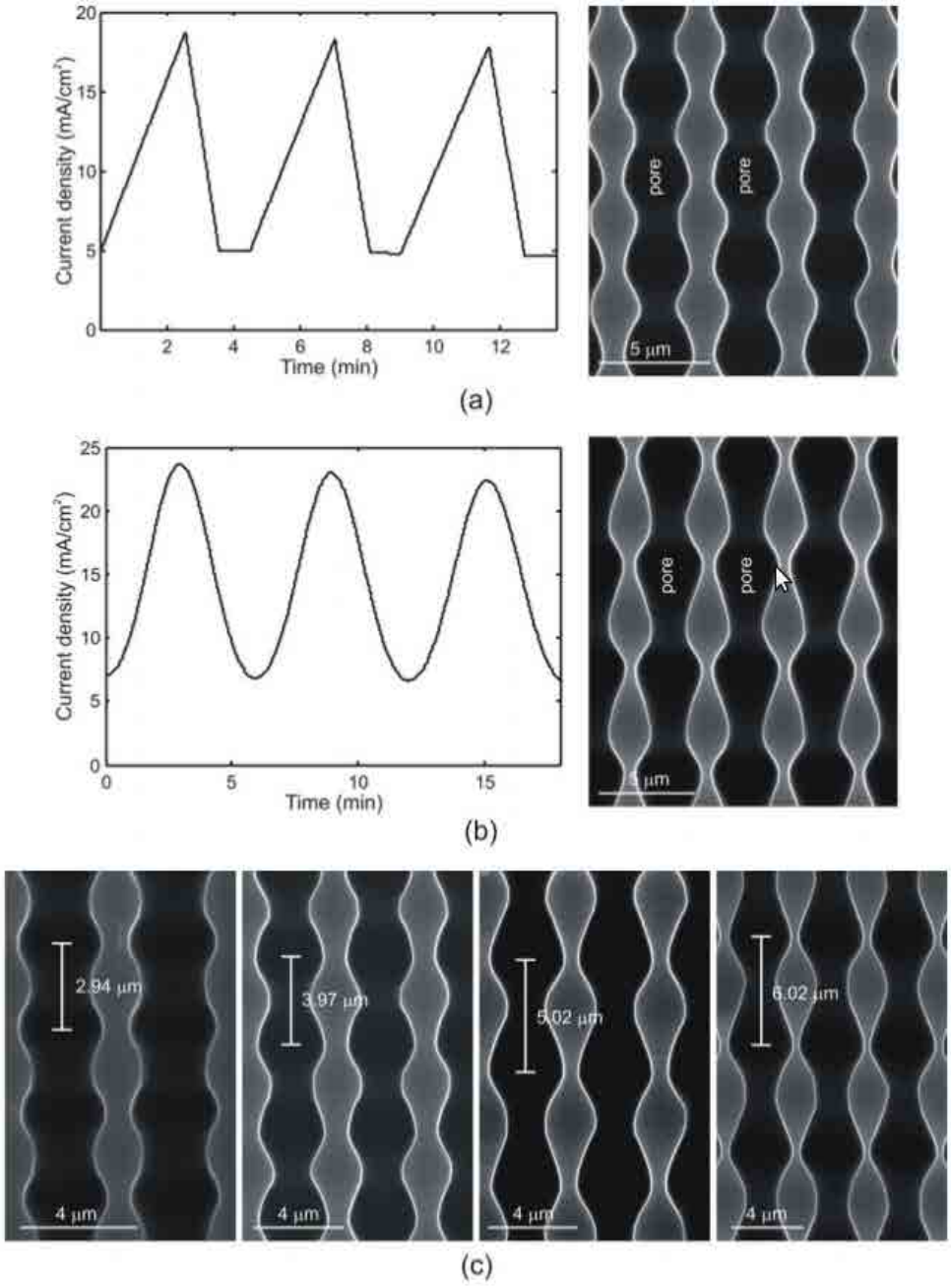


**Figure 3.13:** Examples of 3D macroporous silicon structures. Asymmetric current profile (a) leads to a sinusoidal modulation of pore diameter, while sinusoidal current profile (b) produces asymmetric pores. (c) SEM images of modulated pores with different modulation periods.

Note the sawtooth-like current profile has an asymmetrically varying shape while etched pores exhibit symmetrically modulated diameter. When the current profile is strongly symmetric, the resulting pore shape becomes asymmetric. This means the widening of pore diameter reduces the etching rate in the growth direction as pore grows laterally. As a consequence, the profile of etching current $J$ must be adjusted accordingly.

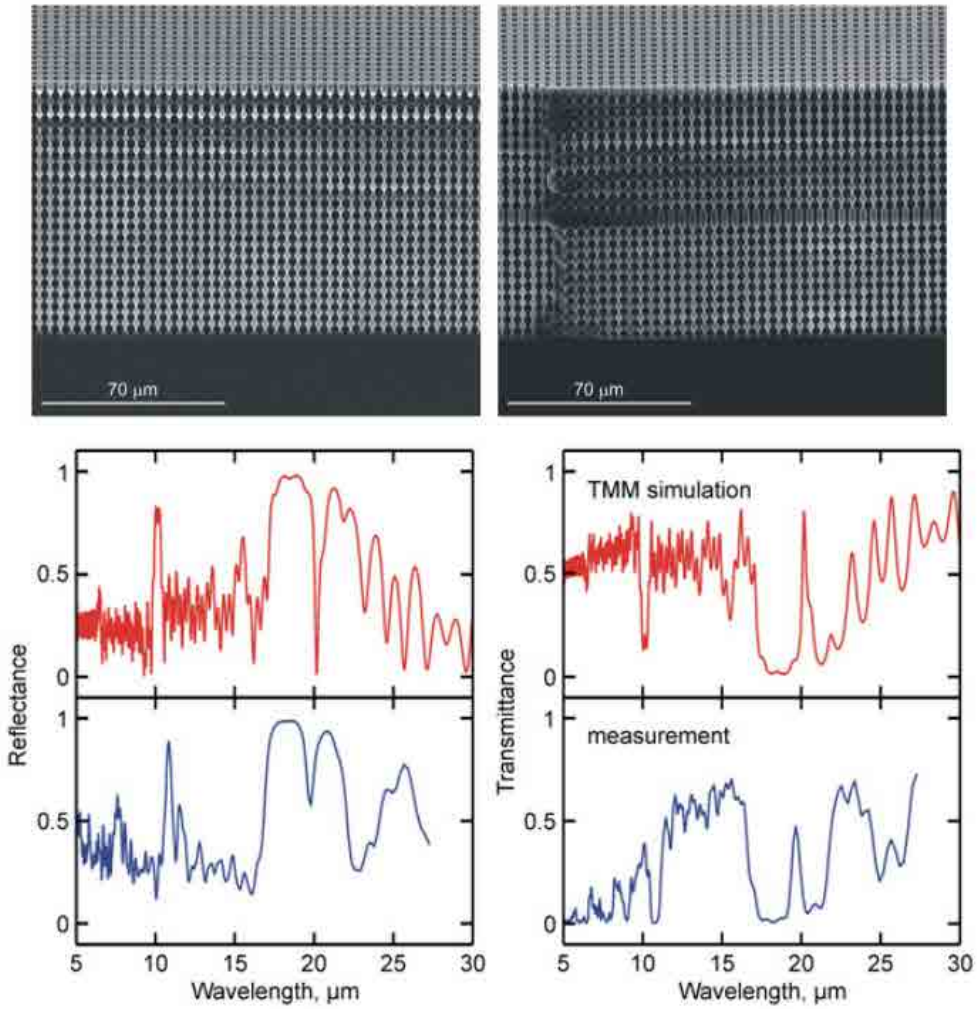


**Figure 3.14:** SEM images of an ideal 3D structure (left) and an embedded planar defect structure (right). The inclusion of a planar defect in a periodic crystal generates an allowed photonic state inside the PBG of the structure, which is observed in the reflectance and transmittance reponses (measure and simulation).

In addition to periodic structures, a wide variety of pore modulations can be

achieved thanks to the control of pore diameter in depth, by simply adjusting the backside illumination. The structure shown in Fig. 3.14 (right) shows a defect in the periodicity of the crystal. Planar defects are created by disturbing the periodic modulation when pores grow into the substrate. As a consequence, an allowed optical state turns up inside the forbidden gap. Fig. 3.14 shows the optical response of the embedded-defect-PhC. Measurements were obtained with the Bruker's FTIR spectrometer while simulations were performed with a TMM-based software.

In addition, let's remark that macroporous silicon structures with modulated pore diameter, although 3D structured, do not have a real 3D geometry. To reach it, pore widening post-processes are performed until neighboring pores start to overlap in the plane perpendicular to the pore axis. This can be accomplished by an oxidation process, as shown in Fig. 3.8, and also by TMAH anisotropic etching, as shown in Fig. 3.15. In the case of TMAH etching, the strong etching rate anisotropy with respect to crystal orientation makes adjacent pores to interconnect forming octagons or rectangles.

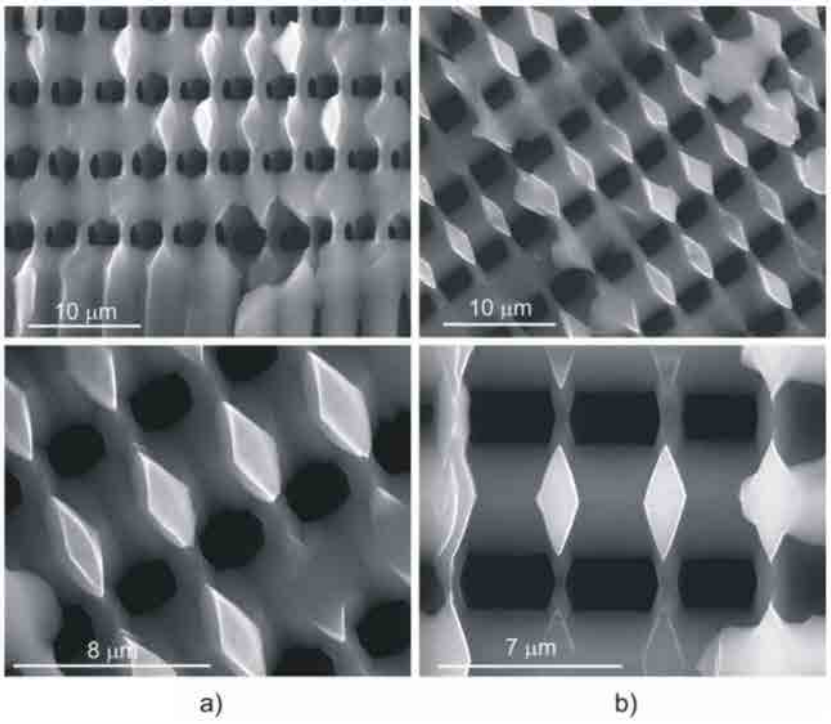


**Figure 3.15:** SEM images of 3D macroporous membrane after pore widening by (a) etching in 25% TMAH solution, 5 °C, 60 min; and (b) etching in 1% TMAH, 5 °C, 180 min.

The lateral interconnection of pores can be also achieved during the fabrication process of mp-Si by electrochemical etching. However, such high porosities would lead to a loss of pore's growth control, and the system would easily draw out from the steady-state regime.

# 4

# Selective Emitters based on Macroporous Silicon

This chapter presents the results on selective thermal emission of macroporous silicon based PhC. The goal of such emitters is the engineering of their structure to inhibit the maximum spectrum of radiation, i.e. spanning the PBG region the maximum in order to transform the broadband emission of Si at high temperatures into a selective thermal source.

## 4.1 Experimental

During the electrochemical etching of silicon, the applied current and voltage were controlled to produce periodically modulated pores in depth. A tilted sinusoidal I-V profile was applied to obtain symmetric periods with strong variation of pore diameter from 0.6 to 1.6 $\mu$m. The periodicity in depth was 2 $\mu$m, as the square in-plane distribution (i.e. pores' positions were patterned following a square distribution with $a_{xy} = 2$ $\mu$m). This way, the fabricated structures were equally periodic in all 3 dimensions. The total area of the fabricated samples was $\sim 3$ cm$^2$. Although larger areas up to wafer scale can also be accomplished,[94] this is enough for an accurate characterization of their structure and optical properties.

Fig. 4.1 shows the current-voltage profiles used to modulate the pores in depth. The I-V profiles were typically repeated for 20 periods ($\sim 40$ $\mu$m depth modulation). With this number of periods, the structure presents a formed PBG in the pores' direction.

Fewer periods cause a poor optical response in the crystal, with a poor gap formation as analyzed in section 2.1.4. More periods just add fabrication complexity as the structure grows deeper, without any gain in the optical response.

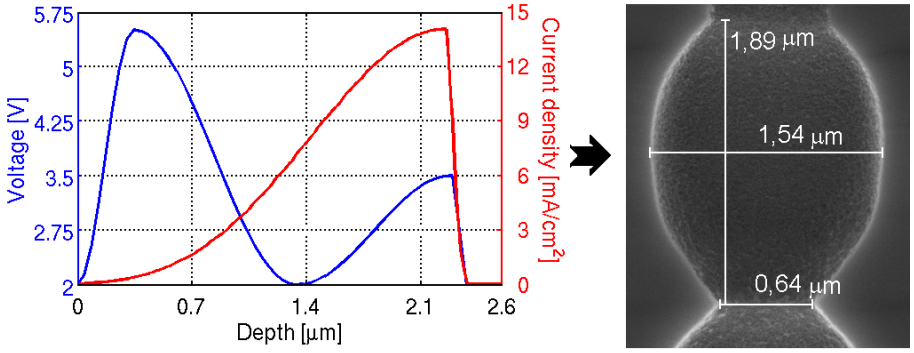


**Figure 4.1:** I-V profile of etched mp-Si structure and SEM images of the resulting pore formation.

To maximize the dielectric contrast in the pore direction the structures were etched to maximize the relation $\triangle d = d_{max} - d_{min}$. Note $d_{max}$ cannot surpass the lattice constant $a_{xy}$, otherwise pores will connect during the etching process and the pore growth would turn unstable. So, maximizing $\triangle d$ results in minimizing $d_{min}$, which was accomplished by the complex modulation of V profile (see Fig. 4.1).

To characterize the fabricated structures, the period length ($a_z$) and period diameters ($d_{max}$, $d_{min}$) of pore modulation were measured from Scanning Electron Microscope (SEM) images. This is plotted in Fig. 4.2. As it is observed, period length was maintained constant along the modulation, with the exception of a first period corresponding to the depth of the initial inverse pyramid created by the TMAH etching (see process in Fig. 3.6). However, it is observed how diameters shrunk as modulation went deeper, even though they were constantly programmed. This effect appears as a consequence of the exhausted electrolyte inside the pores, which is more difficult to be renewed as pores go deeper. The effect must be compensated during the design of the etching I-V profiles to obtain constant modulations of pore diameter.

The values shown in Fig. 4.2 were extracted from mp-Si samples cleaved at the middle of the etching area. It is important to remark that, during the fabrication process, shadow effects provoked by the electrochemical etching cell (Fig. 3.7) cause a smoother and narrower modulation of pore diameter in the edges of the etching area.

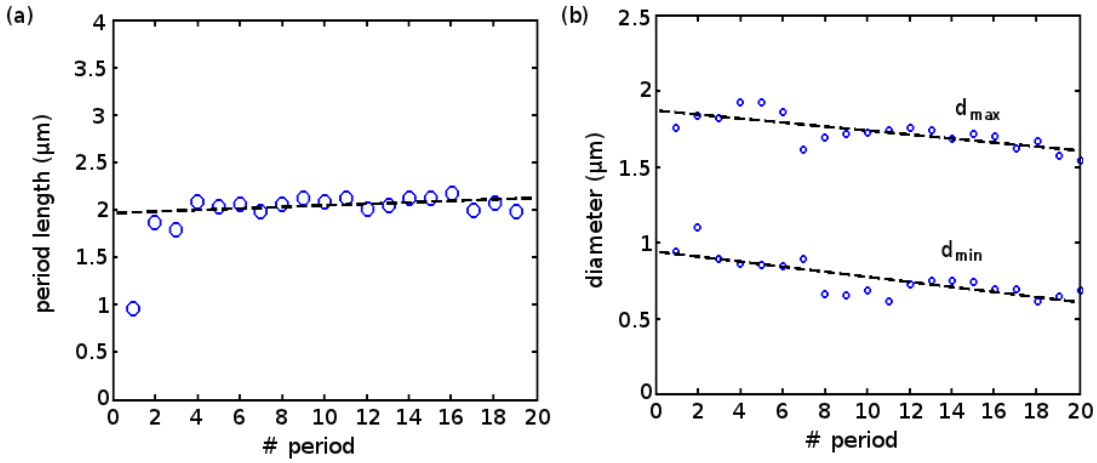


**Figure 4.2:** Period by period characterization of the (a) period length and (b) diameters of pore modulation. The values are extracted from SEM inspection of cleaved samples.

After the etching process, the porosity of modulated structures was increased until pores connected each other at their points of maximum diameter. This process was performed in order to improve the selective thermal emission properties along the three dimensions of the crystal.[56]

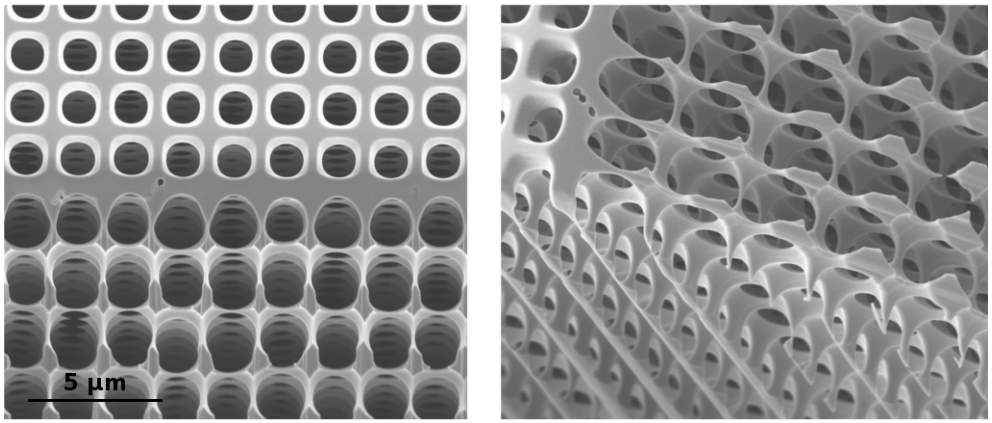


**Figure 4.3:** SEM images of fabricated highly porous silicon PhC. It is observed how pores get interconnected in their points of maximum diameter through the widening process.

The widening was accomplished through 5 consecutive cycles. Pore diameter increased around 500 nm. Fig. 4.3 shows SEM images of the resulting 3D crystal. The structure resembles overlapped air spheres embedded in Si.

## 4.2 Periodic Macroporous Silicon Structures

Results presented in this section firstly refers to macroporous silicon structures directly obtained by the electrochemical etching process. These structures are mainly 2D, presenting only a modulation of pore diameter without lateral interconnection of pores. The analysis of 3D interconnected pores will be presented in section 4.2.1.

After the electrochemical etching process, the obtained mp-Si structures do not open an absolute PBG for all light propagation directions and polarization modes. This is not surprising as the dielectric contrast in the $XY$ plane is much stronger than in the $\hat{\mathbf{z}}$ axis direction (the crystal is not 3D-periodic). In the plane, the dielectric constant alternates periodically between that of air and Si, while the periodic dielectric function variation in the pore direction comes from the smooth modulation of pores diameter.

Instead of an absolute PBG, two stop bands arise in the $\Gamma-$A and $\Gamma-$X directions of the crystal. This was numerically simulated using the MPB software to obtain the dispersion relation of the structures, through the irreducible Brillouin zone, by the PWE method (section 2.1.5). Results are shown in Fig. 4.4.

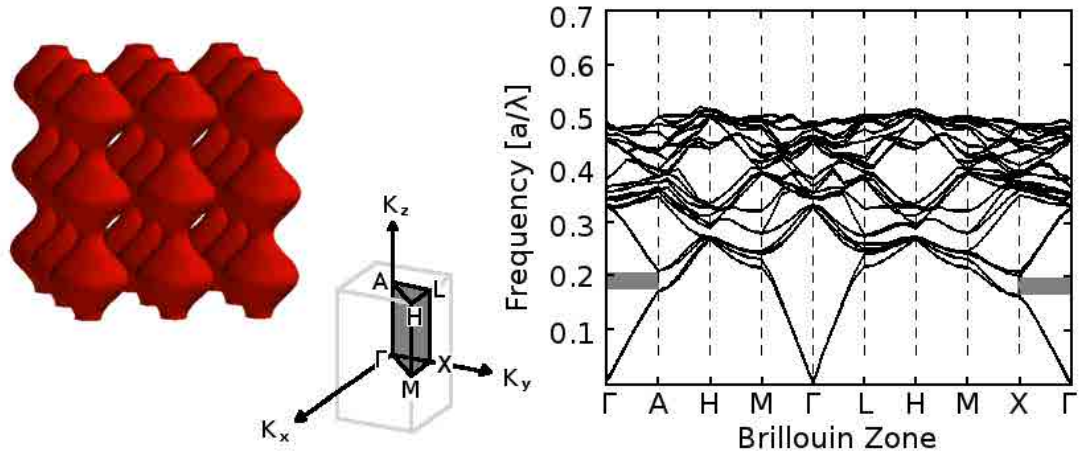


**Figure 4.4:** Dispersion relation of the original electrochemically fabricated mp-Si structure. Band gaps open at pore direction $\Gamma-$A and perpendicular to it ($\Gamma-$X). A draw of the simulated structure and the irreducible Brillouin zone for the tetragonal structure is included.

Note the dispersion relation for a given structure is obtained in terms of the normalized frequency $a/\lambda$. As previously commented, electromagnetism in PhC is scalable

and, as a consequence, the relative gaps observed at 0.19 $a/\lambda$ could be shifted to any frequency range by simply adjusting the lattice constant $a$ of the structure. We developed our crystals with $a = 2$ $\mu$m.

The results of the dispersion relation suggest that these macroporous structures can inhibit thermal radiation in the directions $\Gamma-$A and $\Gamma-$X, but they are unable to completely suppress spontaneous radiation from the surface, as no absolute PBG turns up. However, the suppression of the photonic DOS that can couple, through the surface, to light propagating in free space is enough to fully suppress thermal radiation from the sample's surface. In other words, the condition for an absolute PBG can be reduced to the mere build up of an Omnidirectional Total Reflection (OTR) band.[53]

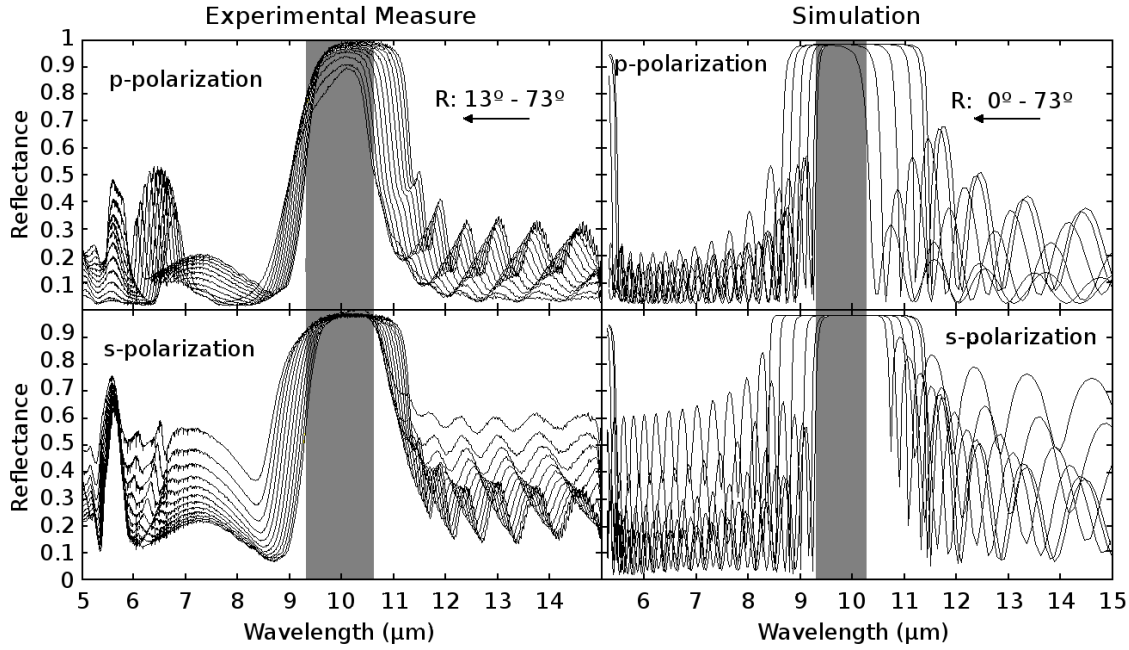


**Figure 4.5:** Room-temperature reflectance measurements (and simulation) of mp-Si PhC at different light incidence angles from 0° to 73°. Results for both $p-$ and $s-$polarization modes are plotted. The OTR band is highlighted in the figures.

The OTR band is calculated by imposing the light line to the dispersion relation of the PhC. All modes falling outside the light line cannot escape the surface and become guided modes inside the crystal and, therefore, spontaneous emission is inhibited as the allowed modes do only exist inside the material and cannot be radiated away. The OTR band was experimentally found, as its name suggests, by measuring the room-

temperature reflectance of the structures for different angles of light incidence from 0° (normal incidence) to 90° (perpendicular incidence). Results are plotted for both $p-$ and $s-$polarization modes in Fig. 4.5.

First, it is observed a shift of the gap position to lower wavelengths as the angle increases. Note the structure's dielectric contrast and periodicity the light "sees" for the different angles of incidence is different. This is a consequence of the tetragonal arrangement. Therefore, the optical reflectance of the structures changes as a function of the angle of incidence.However, we can always find a spectral region in which high reflectance is maintained for both polarization modes and all incident angles. This is the OTR band which is highlighted in gray between $\sim$ 9.5 and 10.5 $\mu$m wavelength.

Experimental measures were taken from 13° to 73° due to limitations in the characterization setup.

The same behavior was observed from simulation results using TMM, although bigger displacements and bigger reflectance values were obtained in the gap so that simulations worked with perfectly periodic structures. Fabrication inhomogeneities and misalignments between the real fabricated structure and the simulated one make the experimental measures to show a smaller shift of structure's gap position and, as a consequence, a wider OTR.

Note also the Fabry-Pérot resonances, which are the sinusoidal lobes at each side of the gap, appear more accentuated in the simulation results rather than in the experimental measures. These Fabry-Pérot resonances come from the various periodicities the tetragonal structure presents and, therefore, they represent a figure of the quality of the fabricated structure (i.e. the more clear the Fabry-Pérot resonances the more periodic the structures is).

When thermal measurements are to be considered, it must be pointed out that structure's emittance can be obtained from the reflectance by $\epsilon \approx 1 - R$. This is because mp-Si PhC show a negligible optical transmittance due to the high doping level of bulk silicon and absorption losses in the NIR and MIR spectral regions. This is observed in Fig. 4.6 where the normal emittance of the mp-Si crystal is plotted at different temperatures.

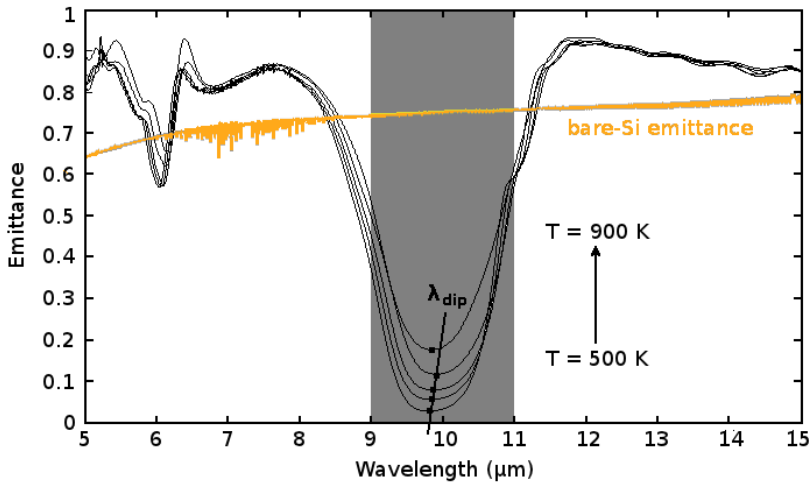


**Figure 4.6:** High temperature characterization of periodic mp-Si emittance between 500 K to 900 K. High temperature emittance of bare silicon is added for comparison.

The gap region, highlighted in gray, is found at the same spectral position than that obtained during the reflectance characterization of the crystal. Note this region does not correspond to the OTR band, which would be narrower as shown in Fig. 4.5, but to the relative gap at normal incidence. Outside the spectral region of the gap, emittance increases above the one of bare silicon. This redistribution of energy was already commented during the state of the art of PhC.

It was found, however, that spontaneous emission in the gap region increased with increasing temperature. The crystals efficiently inhibited thermal radiation in the spectral region 9-11 $\mu$m with a small emittance of 3% at 500 K; while emittance rose up to 17% at 900 K. A perfect suppression of radiation would only be obtained in perfectly periodic structures, a reminiscent emittance is always present as a consequence of fabrication imperfections.

It was also observed a small displacement of the gap dip position to larger wavelengths as increasing temperature. This was consequence of the structure's dilation with increasing temperature.

Even though the inhibition of thermal radiation in the gap region of mp-Si PhC is very efficient, the presented crystals do not fully behave as selective emitters due to the high emission obtained outside the PBG region. An improvement of the selective optical properties is considered in subsequent sections.

### 4.2.1 Symmetry Enhanced 3D Structures

The mp-Si structures presented so far do not meet the symmetry requirements to build a full PBG but present an OTR band. In addition, the formation of a stop band is not a sufficient condition to present selective emission properties. Further enhancing the crystals, through the already presented isotropic pore widening process, can increase the width of this OTR band[53] and generate a secondary gap. Between the primary and secondary gaps, a selective emittance band turns up.

The progressive wall erosion of the silicon-based PhC has two main effects on the photonic stop bands. First, the position is shifted toward higher frequencies. Second, the relative width of the bands changes as the structure is eroded. This is shown in Fig. 4.7 where the dispersion relation of a 3D mp-Si structure is plotted. Note the term "3D" refers to the mp-Si structure with pores interconnected at their points of maximum diameter.

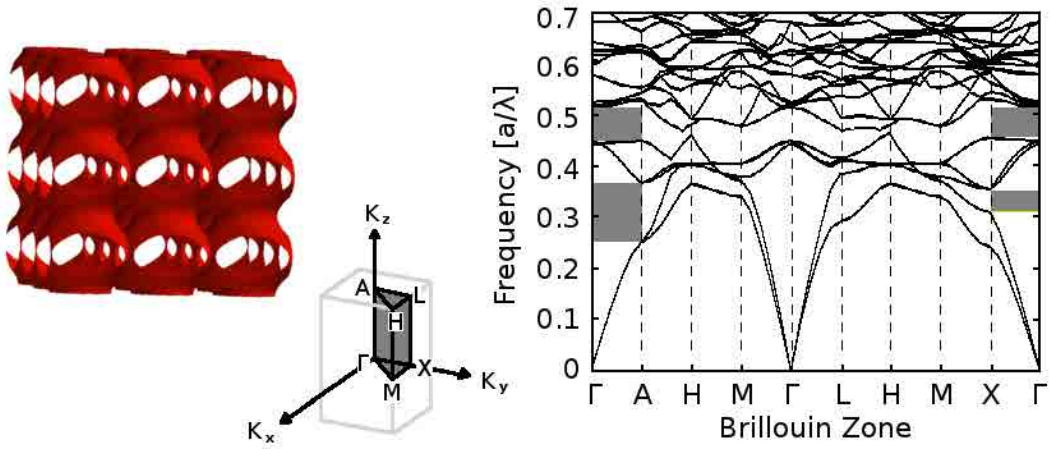


**Figure 4.7:** Dispersion relation of 3D mp-Si crystal. A displacement of gap positions to higher frequencies and the appearance of secondary gaps is observed. A draw of the simulated structure is included.

In the dispersion diagram, a displacement of the gaps' position is observed from 0.19 $a/\lambda$ (in Fig. 4.4) to 0.31 $a/\lambda$. The shift of gap position toward higher frequencies obeys the fact that the average refractive index of the structure is lowered as the porosity is increased. The appearance of a secondary gap, narrower than the primary, at 0.485 $a/\lambda$ is also observed. Note this optical response promotes the formation of an allowed frequency band between the two gap regions.

Room-temperature angle resolved reflectance measurements were performed on the 3D sample in order to study the evolution of the OTR band in highly porous structures. Results are shown in Fig. 4.8. It is observed how, regarding $s-$polarized light, the primary gap shifts to 6 $\mu$m wavelength and the secondary gap appears at 4 $\mu$m, as predicted by the dispersion relation analysis. However, the OTR band disappears as the gap is not maintained for all incident angles in $p-$polarized modes.

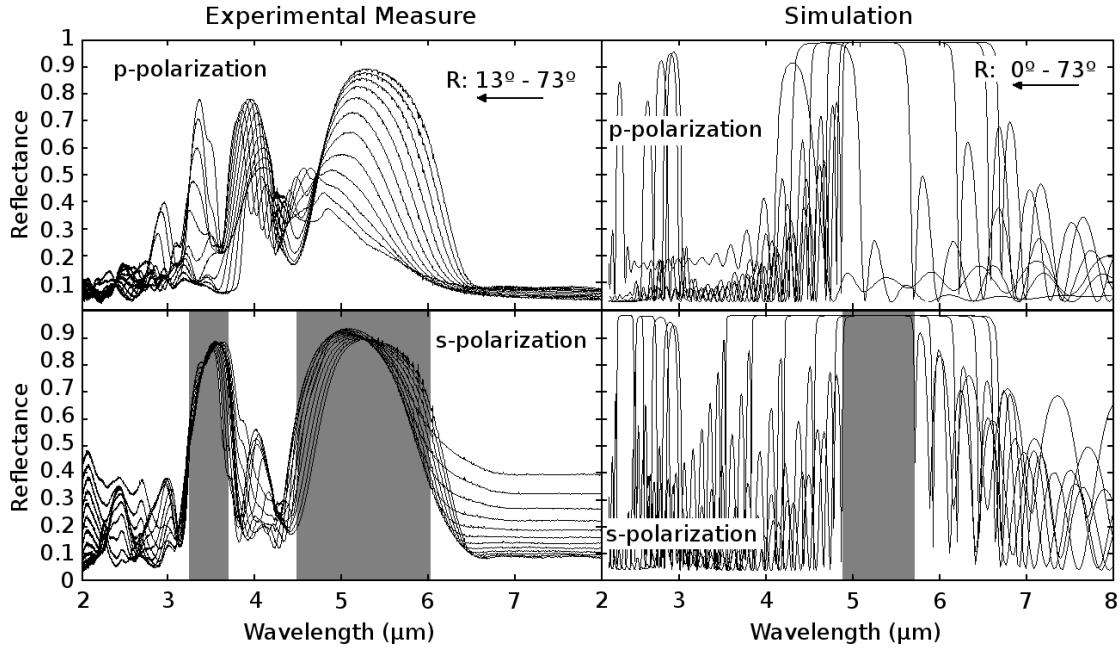


**Figure 4.8:** Reflectance measurements (and simulation) of 3D mp-Si PhC at different light incidence angles from 13° to 73°. The OTR band is no longer maintained due to the degradation of the reflectance response in $p-$polarized light with angle increase.

The same behavior was obtained during the numerical analysis of the 3D structure. Simulations showed that the OTR band was only maintained around 5.5 $\mu$m wavelength for $s-$polarized modes. In $p-$polarized light, the shifting effect of gap position is too strong, moving from 5.5 to 4 $\mu$m wavelength, and degrading its optical reflectance. As a consequence, no stop bands overlap for the different angles and no OTR forms.

As a result, a lower inhibition of thermal radiation is expected in the gap region as emission will not be suppressed at all angles for all light polarizations. In addition, there is no match between the spectral positions of the secondary gap among the $p-$ and $s-$polarized light.

Emittance is analyzed in Fig. 4.9. As it is observed, the ability of suppressing thermal radiation in the gap region is poorer in comparison with what we obtained in Fig. 4.6. In addition, the effect of temperature increase is more evident, affecting the effectiveness of inhibiting thermal radiation in the gap. However, now the influence of the secondary gap at 4 $\mu$m wavelength allows the formation of an emission band around 5 $\mu$m wavelength (with $\sim$1 $\mu$m bandwidth), surrounded by the two gaps. The crystal behaves as a selective emitter with an isolated emission band peaking 0.9 emittance at high temperature.

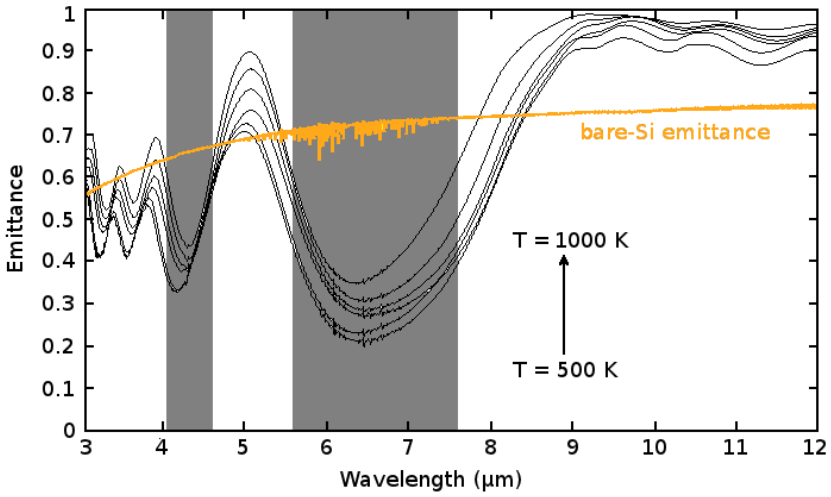


**Figure 4.9:** High temperature characterization of 3D mp-Si emittance after the pore widening process between 500 K to 1000 K. High temperature emittance of bare silicon is added for comparison.

### 4.2.2 Emitter Efficiency

In this section, we analyze the radiant efficiency of the presented 3D-mp-Si selective emitter. The radiant conversion efficiency, or emitter efficiency, is defined as the ratio between the in-band emitted power and the total power emitted at all frequencies at a given temperature. The frontier between the in-band and the out-of-band emission is delimited by the PBG in order to increase efficiency. This way, the high selective band is located within the in-band spectrum, and the inhibited band lays on the out-of-band spectrum. Regarding the working temperature, it is chosen to maximize the selectivity

of the emitter by making the peak emission of Plank's curve and the selective band match.

As it was obtained in Fig. 4.9, the threshold wavelength ($\lambda_{th}$) at which the PBG begins is 5.5 $\mu$m wavelength. This is the point that separates the in-band and the out-of-band regions. On the other hand, the selective band was found at 5 $\mu$m wavelength. Therefore, the working temperature was obtained by imposing $\lambda_{max} = 5\mu m$ to the Wien's displacement law:

$$\lambda_{max} \cdot T = b \tag{4.1}$$

where $\lambda_{max}$ is the peak wavelength of Plank's curve, $T$ is the absolute temperature of the black body, and $b$ is a constant of proportionality called *Wien's displacement constant*, equal to 2897.77 $\mu$m K. Applying the formula, the emitter's working temperature was obtained around 580 K.

The emitter efficiency was calculated at 580 K by integrating the emittance curve in Fig. 4.9 multiplied by the BB curve at 580 K. The resulting radiation curve is shown in Fig. 4.10.

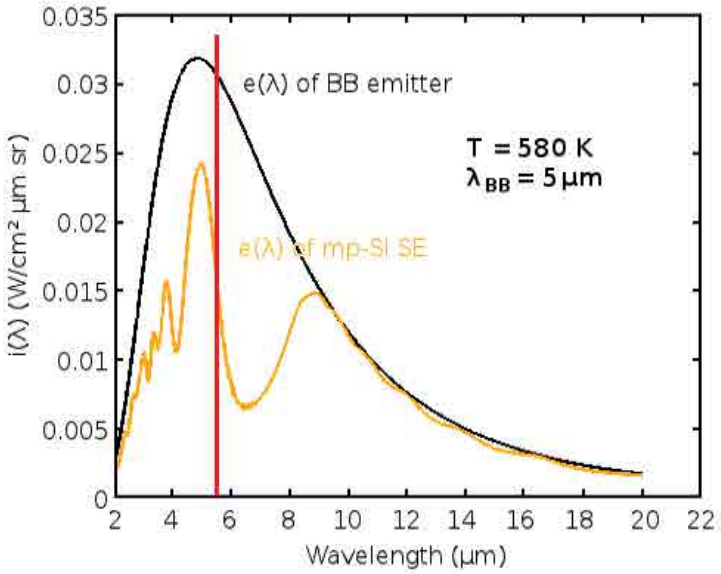


**Figure 4.10:** Spectral thermal radiation for the given 3D selective emitter and the BB at 580 K. $\lambda_{th}$ limiting the in-band/out-of-band regions is highlighted.

It is observed how the PBG region lays on wavelengths $> 5.5\mu$m, reducing the amount of total emitter power in the non-useful spectral region, and the selective band

at 5$\mu$m wavelength is enhanced by the effect of the emitter's temperature. With this, the emitter efficiency turned:

$$\eta_{SE} = \frac{\int_0^{\lambda_{th}} e_{SE}(\lambda)\partial\lambda}{\int_0^{\infty} e_{SE}(\lambda)\partial\lambda} = 0.3386 \tag{4.2}$$

In Fig. 4.10, we also plotted the BB radiation at 580 K for comparison. If we integrate it to calculate the radiant efficiency with the same conditions, the BB efficiency turns:

$$\eta_{BB} = \frac{\int_0^{\lambda_{th}} e_{BB}(\lambda)\partial\lambda}{\int_0^{\infty} e_{BB}(\lambda)\partial\lambda} = 0.379 \tag{4.3}$$

It is clear that the efficiency reached in the designed mp-Si SE is low, as it is indeed lower than that of a simple BB radiator (i.e. a piece of heated SiC). Two main factors influenced this result: the spectral width of the gap region and the energy radiated at wavelengths $< \lambda_{max}$.

The bandwidth of the PBG defines the amount of energy whose radiation is forbidden in the out-of-band spectral region. Maximizing this bandwidth increases the radiant efficiency of the emitter by reducing the amount of non-useful photons radiated. On the other hand, a BB emits a maximum of radiation in the in-band spectral region, while the mp-Si selective emitter is limited by the secondary gap of the crystal and the low emittance level ($\sim 0.6$) at wavelengths below it.

Note, however, this second factor is not a drawback of the design but a pretended consequence. As PV cells are more efficient at the band slightly above $E_g$, and higher energy photons do not produce more electricity as the excess of energy is thermally lost, it is desirable that a selective emitter in TPV systems concentrates thermal radiation in a band slightly above $E_g$, to increase the maximum the efficiency of the system.

As a final remark, it is worth mentioning that 580 K is a very low working temperature for a TPV emitter that would cause an hypothetic system to show a very low efficiency. In addition, an emission band at 5$\mu$m wavelength is far away the NIR spectral regions where most PV converters work (see table 1.1). However, the scalability of Maxwell's equations with the structure's periodicity allows to extrapolate the presented results to any smaller macroporous structure whose selective band matches commercial PV devices (and, hence, the working temperature increases with the decrease of $\lambda_{max}$).

The strategy must be the following:

1. From the chosen PV device, $E_g$ is obtained.
2. The macroporous structure's periodicity must be scaled to present the selective emission band slightly above the cell's $E_g$.
3. The PBG must be maximized in order to forbid the generation of non-useful photons with energy below $E_g$. This is analyzed in the following section.
4. The working temperature of the emitter must be chosen to optimize thermal radiation at the selective band, increasing the efficiency of the TPV system by matching the peak wavelength of Plank's curve with the selective band.

## 4.3 Spanning the PBG by Chirped Quasicrystals

A quasicrystal is a natural expansion of the idea of crystal in which translational periodicity is lost,[95] i.e. a shifted copy of a quasicrystalline structure will never match exactly the original. Since the experimental realization of materials exhibiting quasiperiodic ordering,[96] an increasing interest for electrical and optical applications has risen due to the unique field localization properties of quasicrystals.

Yablonovitch proposed in 1998 that, by chirping or grading the periodicity of a 1D Bragg reflector, the photonic gap could cover an arbitrarily wide spectral range.[97] Chirping is a general concept in which the frequency of repetition of an object is progressively increased or decreased. This way, at some depth in the quasicrystal's structure, any optical frequency would be reflected when finding just that layer spacing that satisfies the Bragg reflection condition. A huge spectral range can therefore be covered.

Fig. 4.11 shows an schema of the concept.

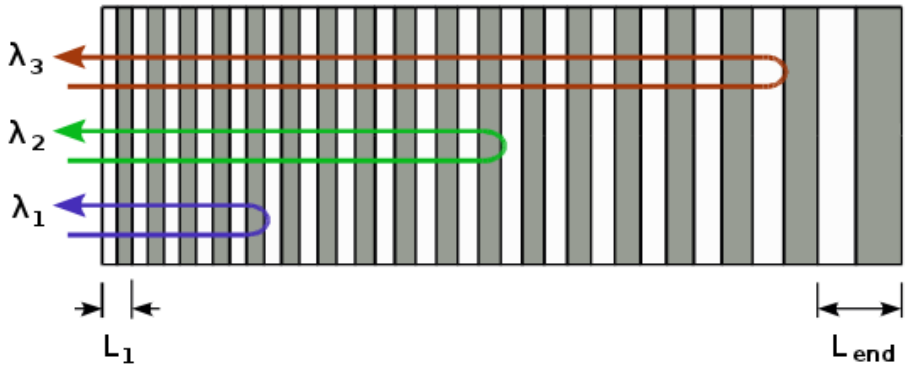


**Figure 4.11:** Schematic of a 1D chirped quasicrystal.

A 3D equivalent quasicrystalline structure was thoroughly analyzed by M. Garín based in mp-Si structures.[53,93] In these crystals, the period of the unit cell is smoothly increased, every period of pore modulation is slightly larger (or shorter) than the previous one. Macroporous silicon with the unit cell gradually varied along the pore axis presents large OTR bands within its optical response. Fig. 4.12 shows a SEM image of a mp-Si chirped quasicrystal with period length varied from 4 to 5 $\mu$m in 35 periods. As a result of the modulation, the PBG of the ideal periodic structure spans increasing

its bandwidth. This effect can be seen as a superposition of the stop-bands generated by the different periodicities contained in the chirped structure.

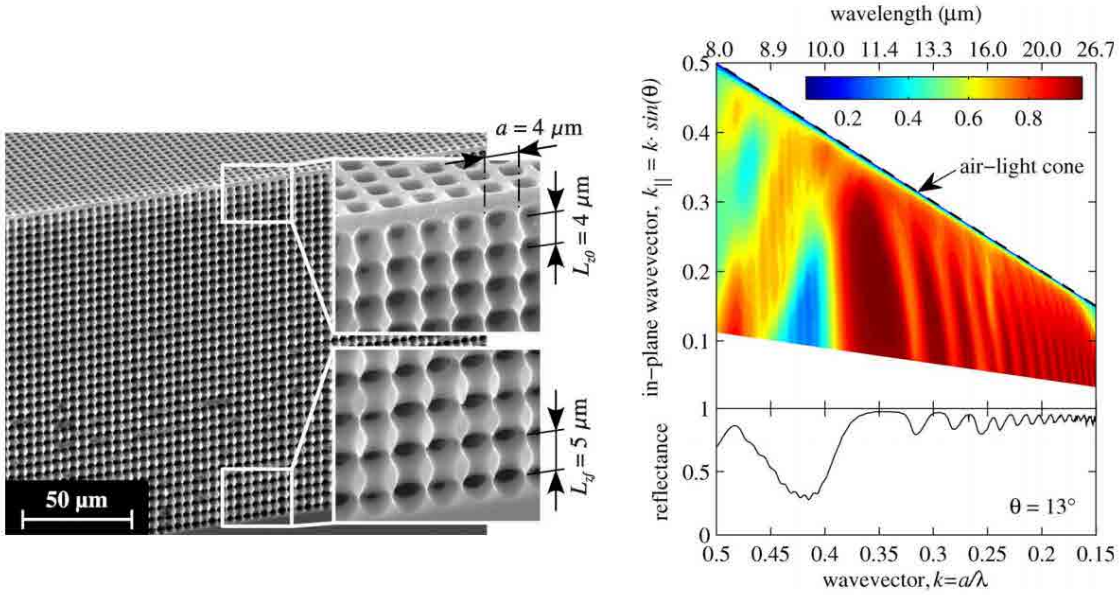


**Figure 4.12:** SEM image of a chirped quasicrystal and its reflectance map. The color bar indicates the reflectance scale. Extracted from[93].

This quasicrystalline structure locally acts as a periodic crystal as far as the transition between the different periods' lengths is smooth. As a result, the formed gap enlarges. However, there is the need for a large number of periods to obtain a wide PBG from the structure's chirping.

To improve these PhqC, and reach wide photonic gaps with the minimum number of periods, the pore modulation is discretely chirped, i.e. the first $n_1$ periods of pore modulation are designed with $a_{z1}$ period length, the subsequent $n_2$ periods are designed with $a_{z2}$ period length, the following $n_3$ ones, with $a_{z3}$, and so on. This way, the continuity of the chirping modulation is discretized and the PBG widens as a result of the superposition of each periodicity's independent gap.

Fig. 4.13 shows SEM images of the discretely chirped fabricated structures. Note the I-V profile utilized to etch the chirped crystals was equivalent to the one presented in Fig. 4.1, the difference lied on the expansion or contraction of the period length to control each periodicity block.

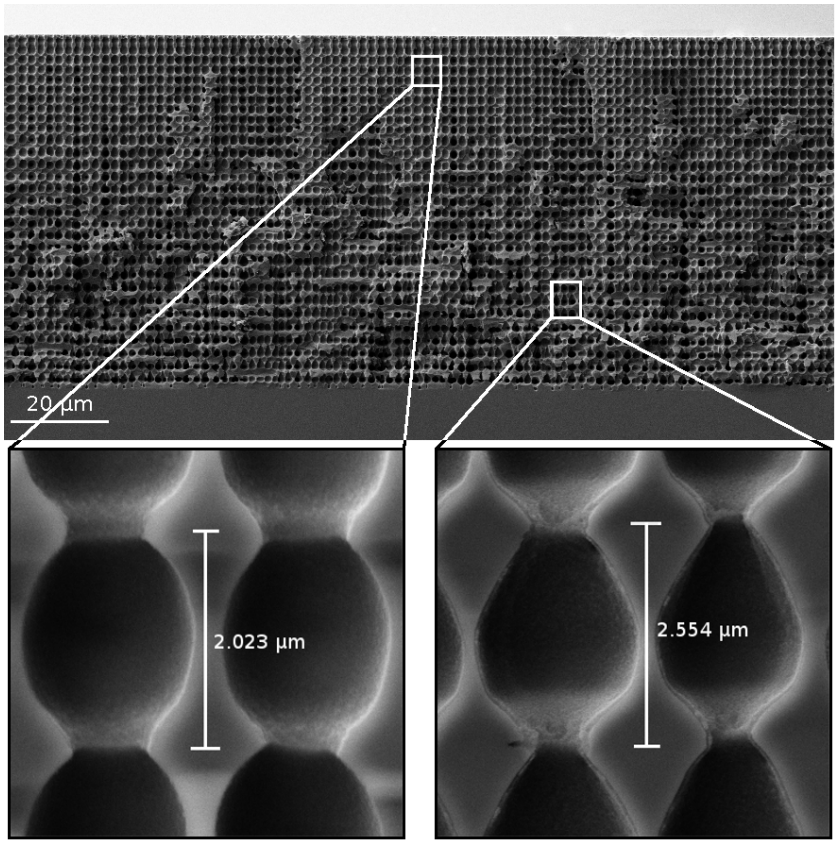


**Figure 4.13:** Discontinuous chirp modulation in mp-Si. Two blocks of periodicity are modulated, first 15 periods with 2 $\mu$m length in average, followed by 15 periods with 2.6 $\mu$m length in average.

### 4.3.1 Numerical Analysis

The optical properties of the discretely chirped PhqC were analyzed by TMM (see section 2.1.5).

For the simulations, a constant number of 10 periods was considered for each periodicity block. Although the number of periods in each block of periodicity, namely $n_i$, can be arbitrarily chosen, it was found that a small $n_i$ value between 8-10 periods was optimal to minimize the total depth of pore modulation, making pore growth more stable and uniform, and obtaining a good optical response of the structure.

From simulations, the gap diagram was obtained, i.e. the evolution of the PBG in function of a given parameter. This analysis is shown, for a 2-block configuration, in Fig. 4.14a as a function of the relation $a_{z2}/a_{z1}$ (considering $a_{z1} = a_{xy}$, the in-plane

periodicity). As it is observed, the bandwidth of PBG spans in frequency as we increase the period length of the second periodicity block. This behavior is maintained up to $a_{z2}/a_{z1} \approx 1.3$. From that point, the stop bands generated by the two blocks separate forming independent PBG regions. Note the enlargement of the gap width is gained on lower frequencies as a result of the enlargement of pores' periodicity $a_{z2}$ with respect to $a_{z1}$ ($a_{z2} > a_{z1}$).

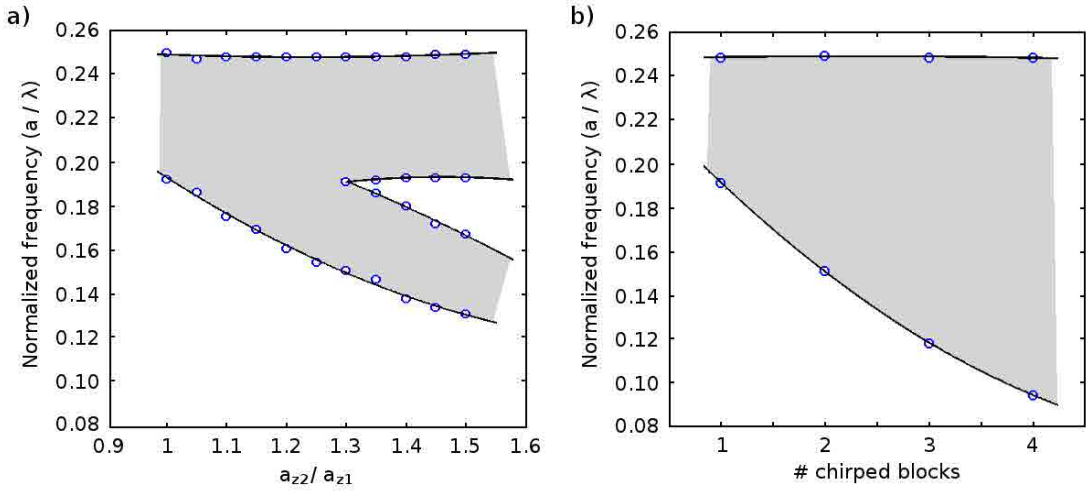


**Figure 4.14:** Gap diagram as a function of (a) the period length relation between two chirped blocks and (b) the number of chirped blocks with overlapping gaps.

From the optimal relation $a_{z2}/a_{z1}$ (1.3), the evolution of the structure's PBG as a function of the number of periodicity blocks ($n_i$) was obtained. Results are plotted in Fig. 4.14b. It is clear how the gap spans by incrementing the number of chirped periodicity blocks. Again, a constant number of periods per block ($n_i = 10$) was considered.

These results suggests the discrete chirped modulation can inhibit spontaneous emission in a great infrared area. As a figure of merit, a 4-blocks configuration considering $a_{z1} = a_{xy} = 2\mu m$ and a progressive increment of block periodicity of 1.3 would show a PBG from 8 to 20 $\mu$m wavelength in the infrared, a much larger gap than the one reached by periodic mp-Si structures (9 to 11 $\mu$m wavelength as shown in Fig. 4.6).

### 4.3.2 Optical Properties

Several experiments were performed in order to characterize the optical properties of real fabricated chirped structures. It is worth mentioning that, when characterizing the optical properties of real fabricated chirped structures, light scattering through the PhqC within the different periodicity blocks made it necessary to use an integrated sphere to jointly measure the specular and diffusive reflectance, to fully characterize the optical response of the crystals.

The first studied modulation was composed of two periodicity blocks presenting the following properties:

**Table 4.1:** Optical properties of a 2-block chirped modulation for different block lengths.

| **Block Periods Length ($\mu$m)** | 2 - 2.25 | 2 - 2.45 | 2 - 2.55 |
|---|---|---|---|
| **Gap Spectral Width ($\mu$m)** | 4.4 | 4.9 | 3.9 |
| **Optical Response Quality** | bad | see Fig. 4.15a | no overlap |

The optimal chirped response, as it is observed in Table 4.1, was obtained for a combination of periodicity lengths of $2 - 2.45\ \mu m$. This relation, 1.225, is found below the one predicted by the simulations, which was 1.3. In fact, the theoretical optimal relation predicted by the numerical analysis, $2 - 2.6\ \mu m$, showed two independent PBGs without spectral overlap. This result is not surprising as we may think that fabrication imperfections may limit the theoretically obtained values.

The optimal fabricated structure, with $2 - 2.45\ \mu m$ periodicity lengths, was characterized by FTIR spectroscopy. Results are plotted in Fig. 4.15a. It is observed that the PBG does not show a constant reflectance level along the whole spectral width. The quality of the obtained response was worse than the one obtained for periodic mp-Si structures (Fig. 4.5). Again, fabrication was a limiting factor. On the other hand, however, the PBG region spanned more than double in the MIR region, which is the effect we were looking for by chirping the crystal.

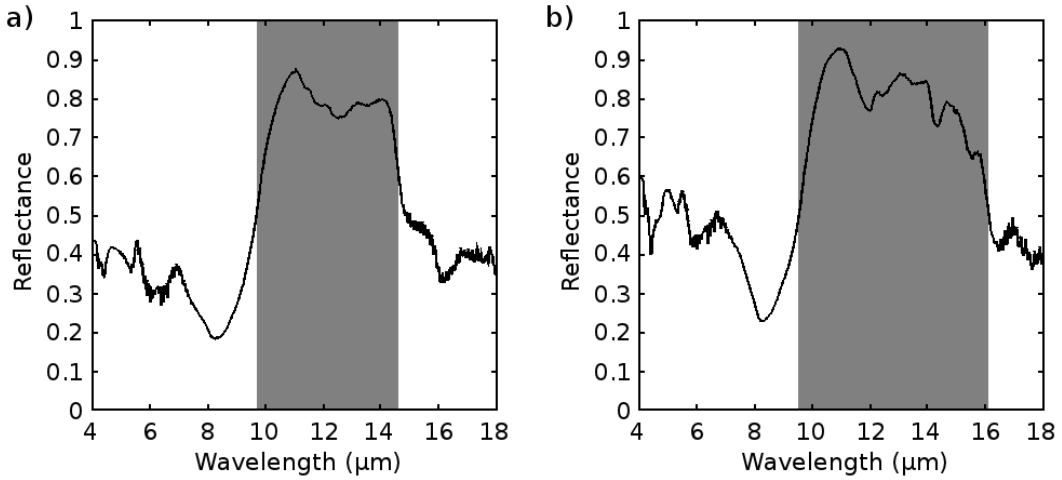


**Figure 4.15:** Reflectance of discrete chirped modulated mp-Si structures with (a) two and (b) three periodicity blocks.

Samples with 3 periodicity blocks were also fabricated. The analysis is shown in Table 4.2. As it is observed, the same behavior of PBG expansion was reached. The optimal response was found for the series of periodicity lengths $2-2.45-2.9$ $\mu$m (whose reflectance is shown in Fig. 4.15b). No gap overlap was reached for larger distances between periodicity blocks, and bad optical responses were reached for the shorter ones.

**Table 4.2:** Optical properties of a 3-block chirped modulation for different periods lengths.

| **Block Periods Length ($\mu$m)** | 2 - 2.15 - 2.3 | 2 - 2.25 - 2.5 | 2 - 2.45 - 2.9 | 2 - 2.6 - 3.15 |
|---|---|---|---|---|
| **Gap Spectral Width ($\mu$m)** | 2.9 | 4.8 | 6.4 | 8.4 |
| **Optical Response Quality** | bad | bad | see Fig. 4.15b | no overlap |

Analyzing the reflectance diagram in Fig. 4.15b, we see that a worse response was obtained from the 3-block fabricated crystal in comparison with the 2-block crystal. Although the PBG region spanned along more than 6 $\mu$m bandwidth, the increase of fabrication complexity, causing more imperfections in the structure as the depth of modulation increases, provoked a worse optical response.

A 4-blocks configuration was tried to be fabricated but no good optical responses could be reached. An improvement in the fabrication technique must be reached previous to face the fabrication of complex structures as a large chirped modulation like the one suggested.

### 4.3.3 Emitter Efficiency

The chirped quasicrystal shown in Fig. 4.15a was post-processed to gain three-dimensionality through the already described cycles of oxidation and oxide-removal. With this process, the primary gaps of the chirped structure were shifted to lower wavelengths and the secondary gaps were enhanced. The obtained radiation curve is plotted in Fig. 4.16.

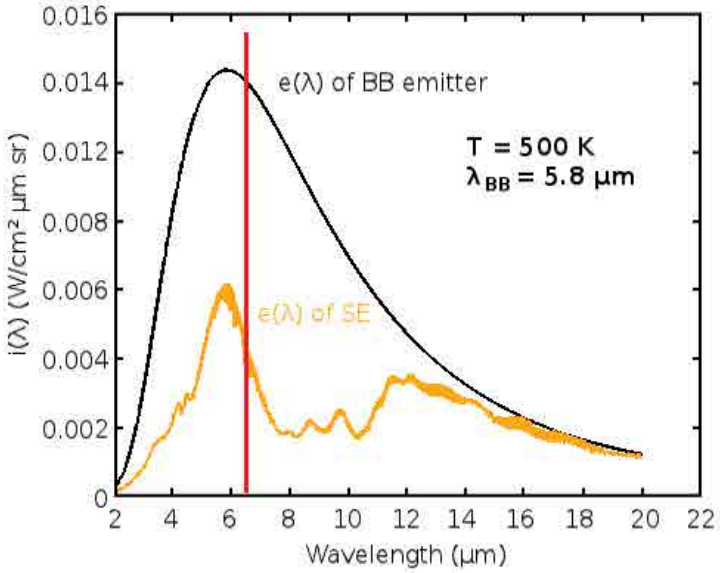


**Figure 4.16:** Spectral thermal radiation for the 3D discretely chirped selective emitter and the BB at 500 K. The in-band / out-of-band limit is highlighted.

Again, the frontier between the in-band and the out-of-band emission is delimited by the PBG generated by the chirped structure, and the working temperature of the emitter is chosen to match the peak emission of the BB to the selective band. The threshold wavelength is therefore 6.5 $\mu$m and the working temperature 500 K.

In comparison with the curve obtained in section 4.2.2, the chirped crystal is capable to inhibit a wider spectrum within the out-of-band region. However, due to fabrication imperfections, the emission spectrum we reach within the in-band region in the chirped crystal is much worse than the one obtained in the periodic crystal: the selective band emittance peaks 0.45, while it was 0.9 in the plot of Fig. 4.10.

This makes the emitter efficiency $\eta_{chirpSE}$ of the chirp structure to be 0.3, lower again than the BB efficiency, $\eta_{BB} = 0.36$, under the given conditions. As a figure of merit, if the selective band of the chirped crystal would maintain the same emittance

level than the periodic crystal (0.9), $\eta_{chirpSE}$ would have been 0.423, more than a 6% higher than $\eta_{BB}$. The limitation is found in the fabrication of such chirped structures, which made not possible to improve the optical response beyond the ones presented in this work.

### 4.3.4 Tunable Selective Emission Bands

An interesting feature of the discretely chirped PhqC is that the periodicity blocks can be chosen to leave in between a spectral region of allowed modes. This is a better approach to reach selective emission as the allowed frequency band can be located in between an arbitrarily number of overlapped primary gaps generated by the chirping. This way, the isolation we can reach is much better than the one obtained by periodic PhC between its primary and secondary gaps.

The spectral emittance of two chirped crystals with tunable selective bands is shown in Fig. 4.17 at 650 K. Both selective bands peaks at 9.5 $\mu$m wavelength. However, Fig. 4.17a corresponds to the emittance of a 2-blocks configuration, leaving the selective band in between, and Fig. 4.17b corresponds to the emittance of a 3-blocks configuration, leaving the selective band between the first and second blocks, and overlapping the second with third periodicity blocks to span this PBG.

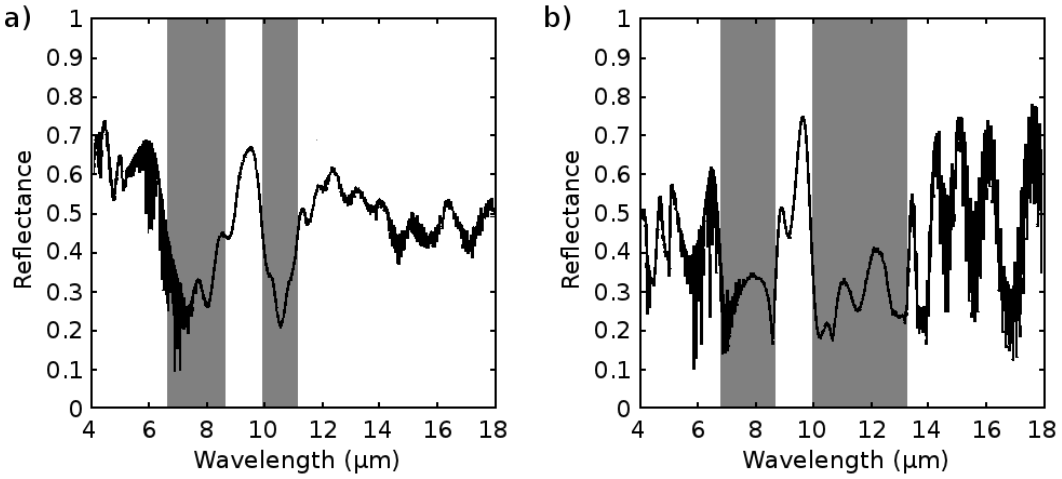


**Figure 4.17:** Emittance measured at 650 K of discrete chirped samples with selective band leaved in between of (a) two blocks of periodicity and (b) three blocks of periodicity.

Although the approach is promising, the selective band is far away the working spectral region of TPV systems. Other applications as IR-spectroscopy must be considered. Such application relies on the characteristic absorption of molecules to estimate the compound and its concentration, especially at wavelengths between 6 and 12 $\mu$m, the so-called fingerprint region, where measurements can be taken with the highest selectivity.

## 4.4 On Thermal Stability

Macroporous silicon PhC were evaluated through several day-cycles of thermal treatment at high temperature up to 1473 K. These stability experiments were conducted in a furnace with controlled $N_2$ atmosphere. Results proved that the mp-Si microstructures were perfectly stable at these high temperatures close to silicon's melting point (1687 K). No degradation of the PhC was observed during the experiments, either in the structure nor in the optical behavior.

The conservation of the optical properties and the thermal stability at high temperatures required, however, the work in a reduction atmosphere (i.e. an atmospheric condition in which oxidation is prevented by removal of oxygen and other oxidizing gases or vapors). In the presence of $O_2$, Si crystals oxidized at high temperatures in an uneven manner, loosing the desired optical response and suffering from thermal stress caused by the interface between Si and $SiO_2$.

Hence, it is required to work in reduction atmospheres (without $O_2$ presence) attending to thermal stability.

### 4.4.1 The Effect of a $SiO_2$ Layer

The radiant properties of mp-Si can be dramatically varied with the inclusion of a coating layer which complements the optical behavior of the silicon emitter. This is the effect of crystal oxidation causing the formation of a thin $SiO_2$ layer on the mp-Si pore walls. The oxide layer adds to the optical response absorption peaks coming from the resonant modes of the oxide.[98]

Thick pieces of $SiO_2$ are very transparent up to $\sim$5 $\mu$m wavelength. For larger wavelengths, the absorption of the oxide is high.[99] However, this property refers to thick pieces as thin films of $SiO_2$ are spectrally transparent in almost the whole spectrum but for some narrow absorption peaks in the vicinity of 9, 12 and 22 $\mu$m wavelength. These subtle peaks are unique of the thin film configuration,[100–102] and arise from transverse- and longitudinal-optical vibrational modes.

Generally, the strong absorption/emission of Si masks the absorption/emission peaks of $SiO_2$. However, if the PBG of the original Si crystal matches the spectral region of the oxide peaks, the gap creates a windowing effect releasing the sharp emission of $SiO_2$ and, due to the huge area and the morphology of the oxide layer along

the 3D structure, enhancing the emission of the thin film (that would be very low otherwise). This is investigated in Fig. 4.18.

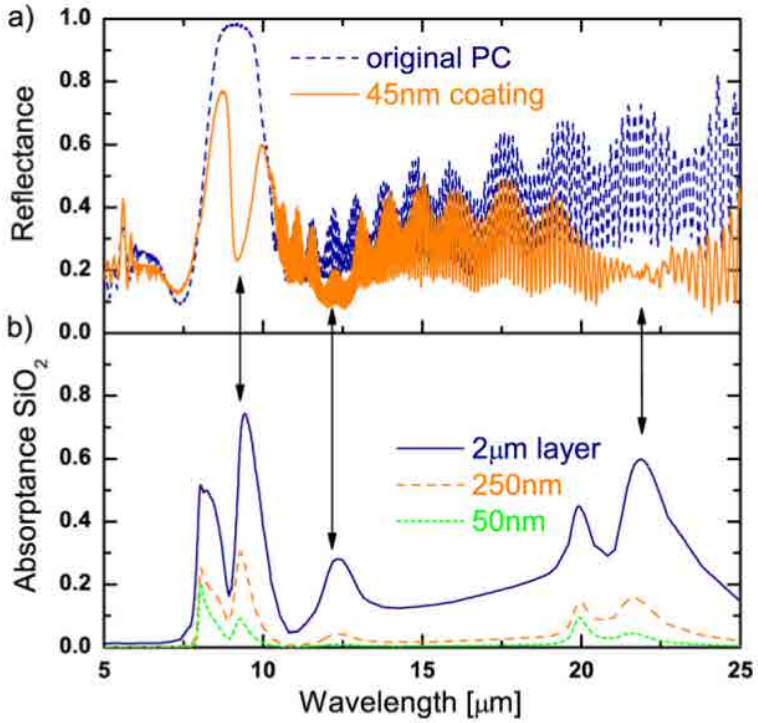


**Figure 4.18:** (a) Reflectance of mp-Si PhC before and after the oxidation process. (b) Simulated absorption of thin SiO2 layers for various thicknesses. Arrows indicate the principal spectral regions of correlation between reflectance decay and oxide absorption. Extracted from [98].

The spectral region with highest reflectivity around 9 $\mu$m wavelength in Fig. 4.18a corresponds to the PBG of the uncoated PhC. A strong decay in reflectivity was observed in the middle of the gap in the oxidized sample (at 9.2 $\mu$m wavelength, specifically). Several decays were also observed around 12 and 22 $\mu$m wavelength. These decays were correlated to the absorptance of $SiO_2$ (shown in Fig. 4.18b for different oxide thicknesses).

The effect of the oxidation might depend on the thickness of the oxide layer. Fig. 4.19 shows a comparison of the obtained reflectance spectra for 15, 25, 35, and 45 nm oxide thicknesses. Beyond the increment of absorption depth with oxide thickness, a small displacement of reflectance dip position was observed within the 9.2 $\mu$m absorption peak (see inset). This result was already stated by Philipp [100] and confirms that

absorption peaks are dominated by the thin film phenomena, stating a dependency of absorption peak position with film thickness. The inset also shows the minor influence of the 8.2 $\mu$m wavelength absorption band due to its location at the edge of the structure's PBG.

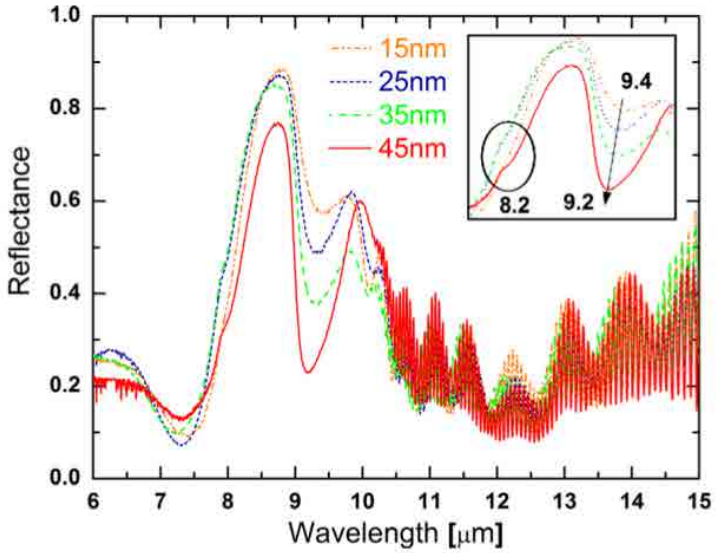


**Figure 4.19:** Reflectance of fabricated samples with various oxide thicknesses. Inset highlights the shift of the 9.2 $\mu$m peak as a function of oxide thickness and the minor influence of another 8.2 $\mu$m absorption peak. Extracted from[98].

When thermal emission measurements were taken, shown in Fig. 4.20, a narrow emission peak appeared in the middle of the gap. The emittance peak depends again on the oxide thickness. It was found that thicker oxide layers, beyond $\sim$ 50 nm, did not show stronger absorption peaks but the properties remained. A maximum of emittance peak was found for oxide thicknesses of 45-50 nm.

As it is observed in Fig. 4.20, there is no trace of the other oxide bands at 12 and 22 $\mu$m wavelength. As it has been commented, the high emittance of Si outside the PBG region masks the properties of the $SiO_2$ layer. Therefore, the effect of the coating is limited to the matching of the crystals' PBG to the intrinsic emittance peaks of the coating material. The effect must be considered in these cases as it might avoid the pretended emission inhibition in the PBG region.

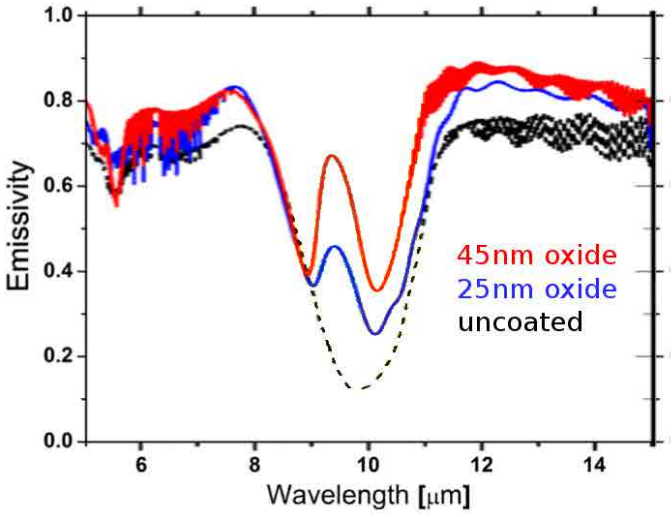


**Figure 4.20:** Direct thermal emission measurements taken at 700 K. It is compared the emittance of the original periodic mp-Si structure with the 25 and 45 nm oxidized samples. Selective emission is highlighted inside the PBG region. Extracted from [98].

### 4.4.2 Application of PBG Windowing

One of the first proposed SE were rare earth oxides. Due to their radiative transitions between energy levels, very sharp and high emittance peaks appear within the radiant spectrum. These selective peaks, as in the case of $SiO_2$, are not unique of rare earths but some other materials also present sharp and high emittance peaks due to similar radiative transitions within their crystalline structure. These materials, however, show their optical behavior only in their thin film configuration, as thicker pieces of material mask these sharp peaks by a broadband emittance/absorption spectrum.

Hence, a host material is needed to support the thin film configuration which must be capable to release (not to mask) the emittance properties of the thin film to exploit them. The solution is not trivial: a flat piece of supporting material with a thin coating on its surface will present little of the emittance properties of the thin film, a more complex 3D structure is therefore required to power up the optical response of the layer. However, such a complex structure will affect the motion of photons through it and, consequently, the spontaneous emission of the base material.

By the use of PBG materials, the properties of the thin film are released in the gap region (as we showed during the previous analysis of the effect of crystal oxidation).

The gap acts as a window and the emittance of the thin film appears as a narrow band.

### 4.4.3 On Absorption Enhancement

Note the effect of the 45 nm oxide layer on the crystal is correlated with the absorption of a 2 $\mu$m thick flat oxide layer (Fig. 4.18). This is a consequence of the porosity of the samples which creates an *effective oxide thickness* thicker than the coating, presenting stronger absorption depths for thin $SiO_2$ coatings.

From the optical properties of $SiO_2$,[99] the absorption of a thin film of $SiO_2$ with 45 nm thickness is calculated to be 8% at 9.2 $\mu$m wavelength. However, experimental results show around 80% absorption (Fig. 4.18a). This enhancement is believed to be caused by the multiple diffraction phenomena that light experiences in PhC. All the partial reflections and refractions the light suffers at each layer of the crystal increase the optical path of the light through the $SiO_2$ layer, increasing absorption.

# 5

# Metal Coated Macroporous Silicon Emitters

This chapter presents the study on metallic selective thermal emitters as a result of the coating with platinum of the well-studied macroporous silicon structures.

Because of their high electron concentration, metals have unique optical properties and are one of the most intensively studied topics in modern photonics to control the light within metallic micro- and nano-structures. For instance, metal-dielectric interfaces are able to support surface plasmon-polariton modes which - at frequencies comparable to a fraction of the metal plasma frequency - can be tightly localized around the metallic surface.[103,104] However, our case of study is slightly different. Due to the large scattering coefficient of metals, dielectric structures with thin coatings of metallic layers above the skin depth behave as entirely metallic structures and, therefore, the dielectric structure becomes a simple support.

The skin depth is a measure of how deep light can penetrate into a metal. It is defined as the depth at which the power of the radiation inside the material falls to $1/e^2$ (about 13%) of its original value at the surface. According to Beer-Lambert law, the intensity of an electromagnetic wave inside a material falls off exponentially from the surface as:

$$I(z) = I_0\, e^{-\alpha z} \tag{5.1}$$

Hence, if $\delta_e$ denotes the skin depth, we have:

$$\delta_e = \frac{2}{\alpha} \tag{5.2}$$

Fig. 5.1 shows the absorption coefficient $\alpha$ of Platinum (Pt) as a function of wavelength, and the corresponding skin depth. As it is observed, the skin depth is below 50 nm in the IR region of interest. Therefore, the structures presented in this chapter with a 50 nm Pt coating must be considered as metallic microstructures.

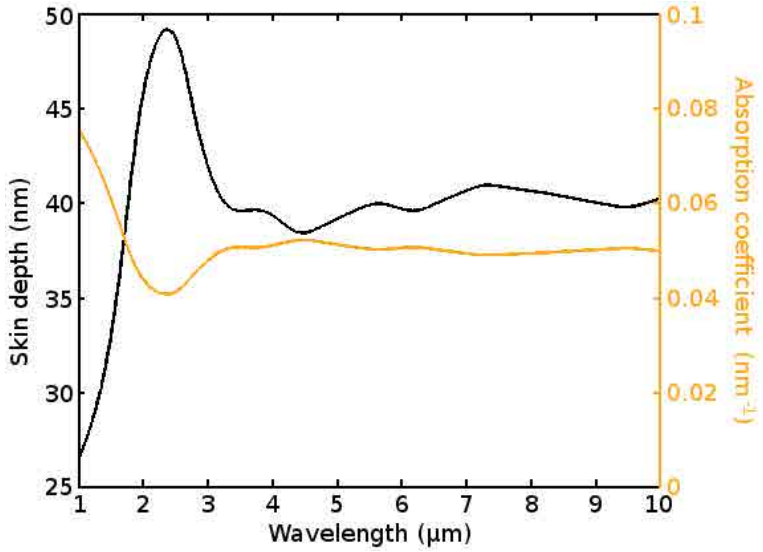


**Figure 5.1:** Skin depth (black) and absorption coefficient (red) of platinum as a function of wavelength in the IR spectral region.

In these crystals, a phenomena of enhancement of the metal's emission appears as a result of the coupling of standing waves in the metallic microcavities, the so-called microcavity effect.[46,105–108] By controlling the size and periodicity of the microcavities, the spectral region where thermal emission is enhanced can be controlled while maintaining in the remaining spectrum the natural low emissivity of metals.

## 5.1 Experimental

To fabricate the array of metallic microcavities we took the well-known macroporous silicon structures with 2 and 4 $\mu$m square periodicity as base material. These two periodicities were chosen to compare the response of the emitters. In these structures, pores act as metallic microcavities when the silicon is coated with Pt.

Even though the effect of metallic microcavity emission is transparent to pore modulation, as the effect comes from the cavity and not its modulation in depth, the 3D structure was created to give consistency and robustness to the conformal platinum coating.

Two different deposition techniques were also investigated: sputtering and ALD. Sputtering was used to coat the surface of the crystals. 50 nm of Pt were deposited at 90 W power in high vacuum conditions (6.5E-6 mbars). To improve the adhesion properties of Pt on the Si surface, a thin layer of 10 nm of titanium was firstly deposited.

Fig. 5.2 shows SEM images of a macroporous sample coated using the sputtering technique. The image shows a transverse view of the initial modulation of two pores after cleaving the sample at the middle of the etched area. As it is observed, the sputtering technique is only capable to coat the surface and the first nanometers of the pores, the ones corresponding to the initial inverse pyramids created by TMAH. No trace of Pt is found in the first period of pore modulation.

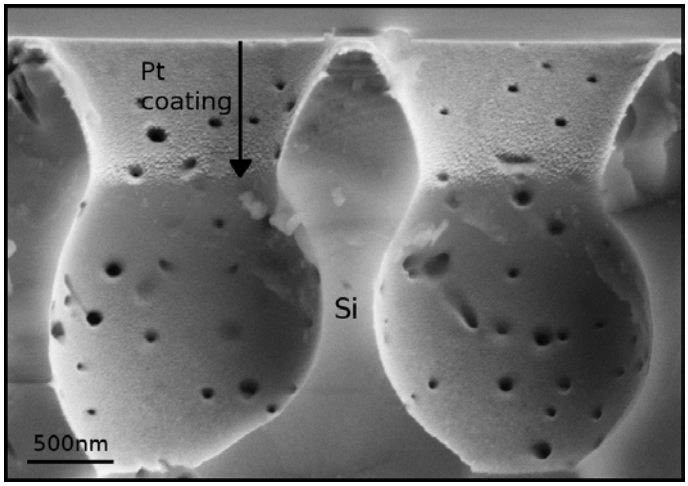


**Figure 5.2:** Transverse view of a cleaved mp-Si sample after a sputtering process to deposit 50 nm of Pt. The coat covered the surface of the sample and the walls of the initial inverse pyramid.

Note in the image pores are spiked with some holes that go through adjacent pores. This is caused by a bad optimization of the etching conditions during the electrochemical attack of silicon. Although this might be avoided in dielectric PhC to reach an accurate optical response, metallic structures are not affected as the optical phenomena that predominates is the microcavity effect.

On the other hand, ALD technique was used to coat a conformal layer on the whole porous surface and inside the pores of the macroporous structure. Half of the samples that were coated with ALD had a thin layer of $SiO_2$ created after a short duration oxidation. Although this did not affect the optical response of the metallic samples, it had its importance when thermal stability issues were evaluated.

The coating was accomplished using 4 precursors in two steps: a first coating of 5 nm of $Al_2O_3$, again for adhesion purposes, was deposited by 50 cycles of Trimethylaluminum (TMA) and water vapor precursors; then, 50 nm of Pt were grown by 1000 cycles of Me3MeCpPt(IV) and $O_2$ precursors.

Fig. 5.3 shows the result of the ALD coating. As it is observed, the ALD technique was capable to coat the whole 3D structure. The sample was cleaved after the deposition and characterized with SEM to differentiate between the silicon, which appears darker in the images, and the platinum, which appears brighter. As commented, the structure was chosen to be three-dimensional to give robustness to the metallic coating as the Pt layer interconnects in all points where pores from the original structure, at their points of maximum diameter, interconnect with their adjacent pores.

It is worth noticing how ALD deposits the coating layer in a granular manner. This is intrinsic of the technique. It was observed that this morphology did not affect the pretended optical response of the metallic microcavities.

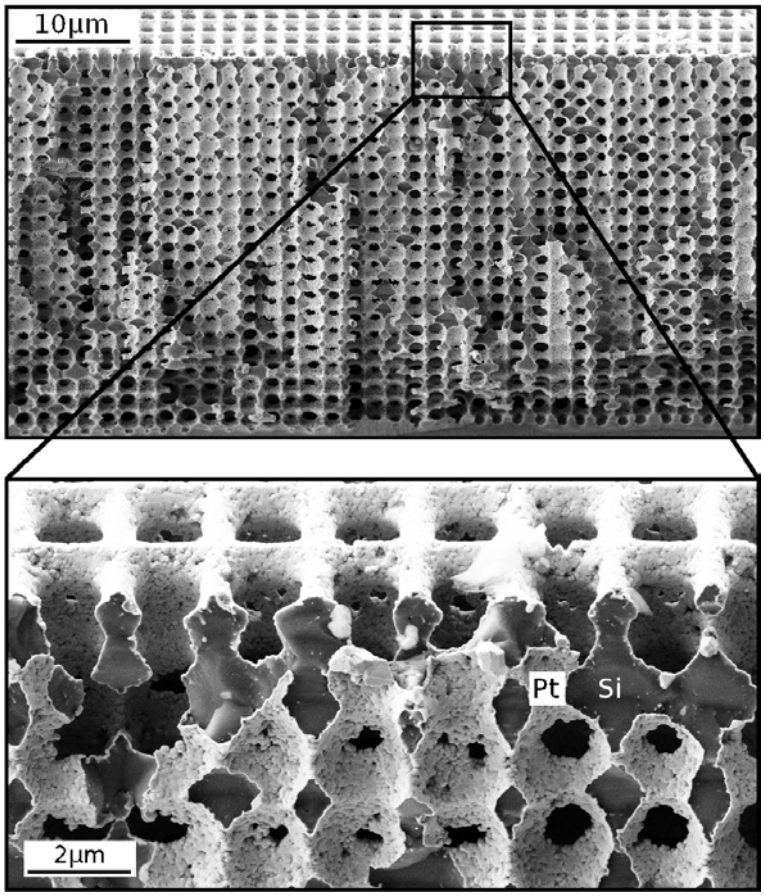


**Figure 5.3:** Bird's eye view of an ALD platinum coated 3D macroporous sample (above). Zoom into various cleaved pores (below). It is distinguished the areas with platinum with respect to the silicon areas of the original structure.

## 5.2 Resonant Absorption

Metallic structures are typically preferred as selective emitters as they naturally keep the emissivity low at long wavelengths, while it can be enhanced at shorter wavelengths through micro-structuring. Reflectance in metals is high for most wavelengths due to the high value of the extinction coefficient (the imaginary part of the metal's refractive index) and, therefore, emittance tends to be very low ($< 10 - 20$ %). This behavior can be tailored by micro and nanostructuring metallic surfaces in a periodic way, as it was presented in Fig. 1.8.

These structures usually rely in the use of refractory metals, such as tungsten and tantalum, in order to attain the desired emission selectivity and high-temperature sta-

bility.[49] Unfortunately, it has been found that metallic micro- and nano-structures are unstable at temperatures much bellow the melting point of these materials due, mainly, to surface diffusion effects and thermomechanical stresses between layers and interfaces. Even 3D layer-by-layer structures, such as tungsten woodpile PhC, contain multiple interfaces, thus making them fragile.[43,44,109]

Our approach, a silicon-metallic 3D structure, exploits both the high thermal stability of silicon and the high spectral selectivity of microstructured metal based in the microcavity effect. The bandgap edge of the crystal can be tailored to theoretically any wavelength of interest, limited only by fabrication limits, by controlling the cavity's resonant frequency and the sidewall thickness that must be thicker than the skin-depth of the metal to preserve the wavelength selectivity of the emitter.

An optical cavity or optical resonator is an arrangement of mirrors that forms a standing wave cavity resonator for light waves. Light confined in the cavity reflect multiple times producing standing waves for certain resonance frequencies. In general, the enhancement in emission in the microstructured array of metallic cavities is achieved by this coupling into resonant electromagnetic modes. In such systems, the threshold (or cut-off) wavelength is approximately given by the fundamental mode of the cylindrical metallic cavity at wavelength double the cavity size.[47,110,111]

For radiation with wavelengths shorter than the fundamental cavity resonant mode, enhanced absorption occurs due to the increased interaction time with the absorptive metal through evanescent waves. On the other hand, radiation with wavelengths larger than the fundamental mode is forbidden from entering the cavities, thus maintaining the desired wavelength selectivity.[112] In this regime, we can easily shift the cut-off wavelength by selecting the appropriate cavity size.

Resonant absorption might only affect to the emittance at wavelengths close to or smaller than the periodicity, whereupon diffracted plane waves and surface plasmon modes start to appear. Because the enhancement in emittance is dominated by the Q-matched electromagnetic cavity modes, surface plasmons can safely be ignored in the analysis.[113]

## 5.3 Optical Properties

As it was discussed in previous section, the resonant absorption of light in the metallic microcavities depends on the periodicity and the width of the cavity. In mp-Si crystals, this refers to the surface diameter of pore modulation. Fig. 5.4 shows SEM images of the 2 $\mu$m periodicity samples coated with Pt. The initial inverse pyramid created by TMAH makes the cavities to present an outer diameter (surface) of 1.58 $\mu$m and an inner diameter (previous to pore modulation) of 1.12 $\mu$m.

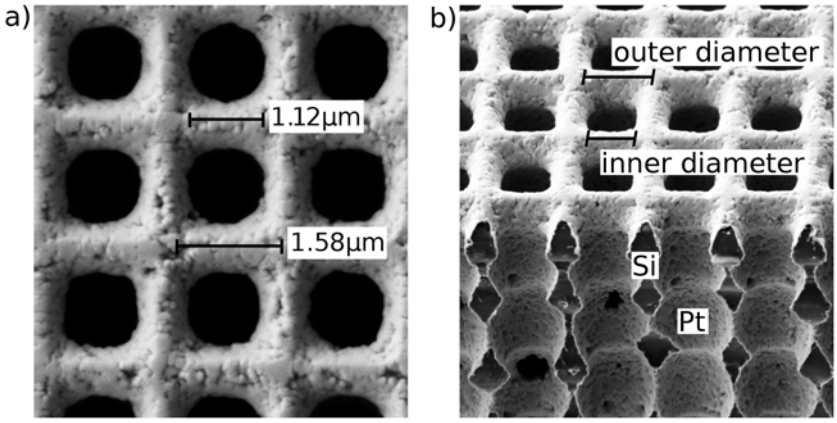


**Figure 5.4:** SEM images of a Pt-coated 2 $\mu$m periodicity sample. (a) Surface and (b) cross section.

With this cavity width from 1.12 to 1.58 $\mu$m, the resonant modes must therefore be found at wavelengths between 2.24 and 3.16 $\mu$m for the 2 $\mu$m periodicity samples (and at double wavelengths, between 4.48 and 6.32 $\mu$m, for the 4 $\mu$m periodicity samples as the structure's size is double). Reflectance measurements of the fabricated samples are plotted in Fig. 5.5 showing a strong reflectance decay centered at 2.75 and 5.22 $\mu$m wavelength for the 2 and 4 $\mu$m periodicity, respectively. These results confirmed the spectral control over the reflectance response with periodicity and cavity size. This effect, already reported in the literature by "all-metallic" structures,[44,46] is demonstrated to be equivalent in our "metal-coated" macroporous structures.

The specular reflectance of a plane Pt surface (a polished piece of Si with a thin layer of Pt on top) is also plotted in Fig. 5.5a for comparison. It is observed how Pt has a high reflectance in the whole NIR and MIR spectral regions. In addition, a sharp absorption peak is observed in the figure around 5 $\mu$m wavelength. This corresponds to

the atmospheric absorption of $CO_2$. As it was commented in section 3.3, atmospheric absorption mainly from water vapor and $CO_2$ is always present in the measurements.

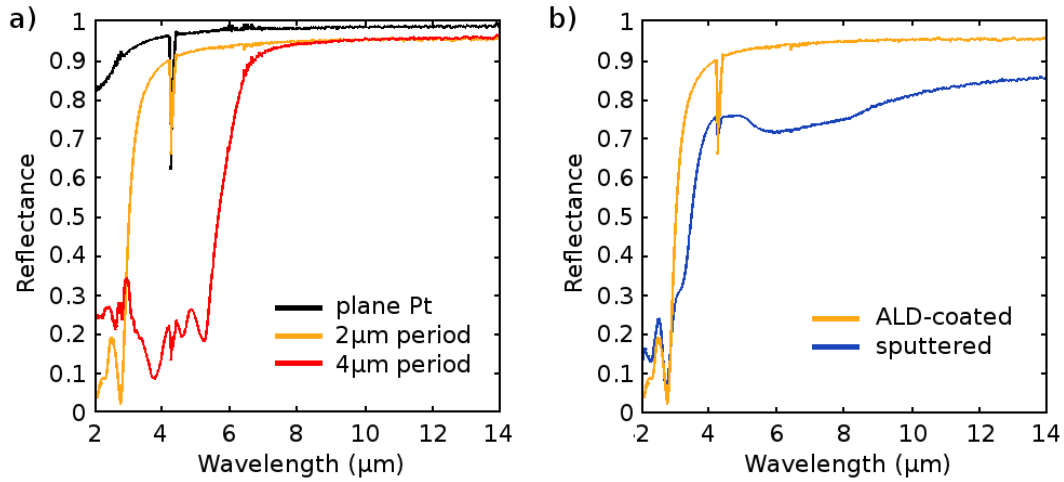


**Figure 5.5:** (a) Reflectance of the ALD-coated Pt microstructures with 2 and 4 $\mu$m periodicity in comparison with the reflectance of plane Pt surface. (b) Reflectance of the ALD-coated sample vs. the sputtered sample for the same periodicities (2 $\mu$m).

It is worth mentioning that the same reflectance decay behavior around 3 $\mu$m wavelength was observed in both sputtered and ALD-coated samples (Fig. 5.5b). However, in comparison, the ALD-coated sample shows a better reflectance for larger wavelengths as a consequence of the whole coating of the 3D macroporous structure.

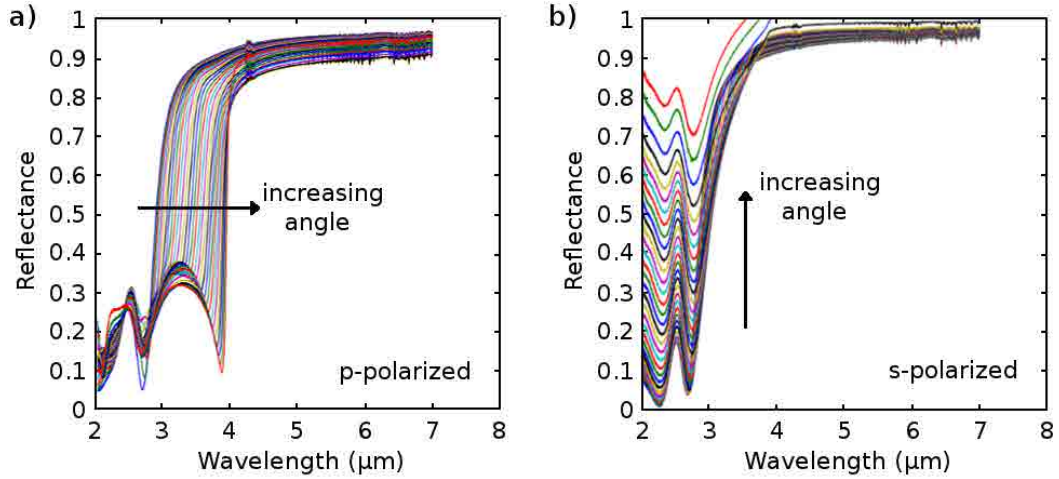


**Figure 5.6:** Reflectance of the ALD-coated Pt microstructures with 2 $\mu$m periodicity as a function of the angle from 13° to 73°. (a) P-polarized light and (b) S-polarized light.

The analysis of the optical reflectance of Pt crystals with incident angle and light polarization is presented in Fig. 5.6. We found the same spectral response at normal incidence (13°) for both $p-$ and $s-$polarized light. As the angle of incidence increased, however, the reflectance dip position shifted from 2.75 to 3.9 $\mu$m wavelength in the $p-$polarized modes. On the other hand, $s-$polarized light experimented an increase of the spectral reflectance with incident angle at wavelengths below the resonant absorption region around 2.75 $\mu$m wavelength.

High temperature emittance was investigated on the 2 $\mu$m periodicity samples as the enhancement of the emissivity is found closer to the NIR spectral region. Fig. 5.7 shows the emittance of the sample at 1073 K. This was the limit temperature of the setup to characterize the platinum PhC. We found the same emittance selectivity at all tested temperatures up to 1073 K.

In Fig. 5.7 it is observed how the typical low emittance of the metal in the MIR region is maintained below 0.2 for wavelengths $> 3\mu$m. Then, a strong enhancement of the emittance arised, as analyzed in the reflectance measures, at wavelengths $< 3$ $\mu$m. Emittance showed maximums at 2.75 and 2.3 $\mu$m wavelengths peaking 0.95 at 1073 K. Below 2.3 $\mu$m wavelength, emittance decreased below 0.7.

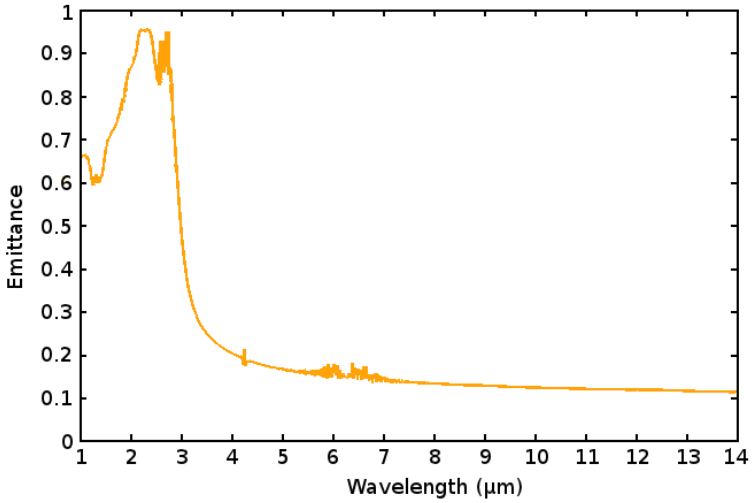


**Figure 5.7:** Emittance of the Pt-structure with 2 $\mu$m periodicity at 1073 K. The selectivity of the radiation spectrum is clear.

### 5.3.1 Emitter Efficiency

From the emittance response in Fig. 5.7, it is observed that metallic microstructures behave as highly efficient selective thermal emitters. The suppression of a maximum of spontaneous radiation in the out-of-band spectral region, that we pursued by chirping the pore modulation of mp-Si samples, is here accomplished by the natural low emission of the metal. In addition, the emittance in the in-band region is as high as it was reached with periodic 3D mp-Si, $> 0.9$, and at lower wavelengths the emittance decreases concentrating the maximum of radiation in a narrow spectral region between 2-3 $\mu$m wavelength.

In addition, the selective emission band in these metallic PhC is located at lower wavelengths peaking 2.75 $\mu$m. The optimal emitter's working temperature for this given emission wavelength, applying again the Wien's displacement law (eq. 4.1), is 1054 K. This temperature is enough to reach good conversion efficiencies in TPV systems thanks to the high spectral selectivity, although conventional TPV systems usually work at higher temperatures.

The radiation curves for both the selective emitter and the BB at 1054 K are plotted in Fig. 5.8. The in-band/out-of-band threshold wavelength is 3 $\mu$m.

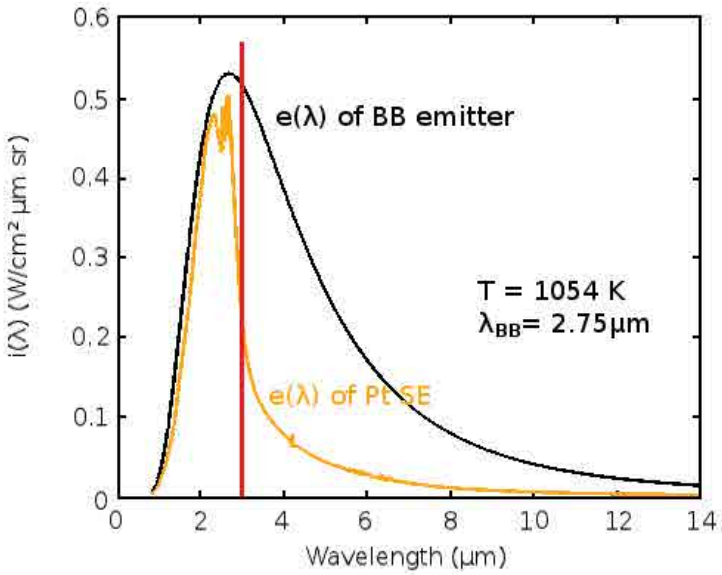


**Figure 5.8:** Spectral thermal radiation for the 2 $\mu$m periodicity Pt PhC and the BB at 1054 K. The in-band / out-of-band limit is highlighted at 3 $\mu$m wavelength.

From the curves in Fig. 5.8, the emitter efficiency was calculated at 1054 K: the metallic microstructure showed $\eta_{metallicSE} = 0.66$ and the BB showed $\eta_{BB} = 0.32$. This great efficiency improvement is caused by the features analyzed at the beginning of the section: high spectral selectivity, low emittance at large wavelengths and high emittance around $\lambda_{th}$.

## 5.4 On Thermal Stability

In previous section it was discussed that, during the analysis of the emittance properties of Pt crystals, we obtained the same selective response at different temperatures and for both the ALD coated and the sputtered samples. However, this is not completely true attending to the emittance temperature and thermal stability.

Samples with an ALD coating were thermally stable during characterization in air atmosphere from room temperature up to 1073 K, conserving the properties shown in Fig. 5.7. Many thermal cycles of heating up / cooling down were performed to fully characterize the samples. In these cycles, samples were at high temperature during thirty minutes to one hour, no degradation of the Pt layer was observed. This guaranteed the thermal stability of ALD coated samples up to 1073 K in air atmosphere for these short periods of time.

On the other hand, the optical response of the sputtered samples was lost when samples were heated beyond 823 K. After few minutes at high temperature, the sputtered structures rapidly degraded by the metallic layer forming small droplets. Therefore, selective emittance disappeared as the metallic layer on the silicon surface agglomerated.

This is indeed a well-known effect caused by annealing at high temperatures on thin Pt films deposited on top of dielectric substrates.[114] Various fabrication processes are actually based in this high temperature annealing to obtain nano- and micro-metallic droplets.

To analyze the limit temperature at which ALD coated samples were thermally stable, temperature tests were carried on in a muffle oven with atmospheric control. The muffle experiments included thermal annealing in vacumm, $N_2$ and $O_2$ (air) atmospheres for 8 to 12 hours at constant temperature. Samples with a thin oxide layer between the platinum and the silicon were tested together with the samples without that $SiO_2$ layer.

During these temperature tests, the degradation of the metallic layer in ALD-coated samples was observed at higher temperatures than that established for the sputtered samples. This is believed to be caused by the complex 3D structure (shown in Fig. 5.3) with interconnecting pores. The limit temperature for ALD samples was found to depend on the atmosphere and on the $SiO_2$ layer. Fig. 5.9 summarizes the resulting optical responses after the thermal annealing tests.

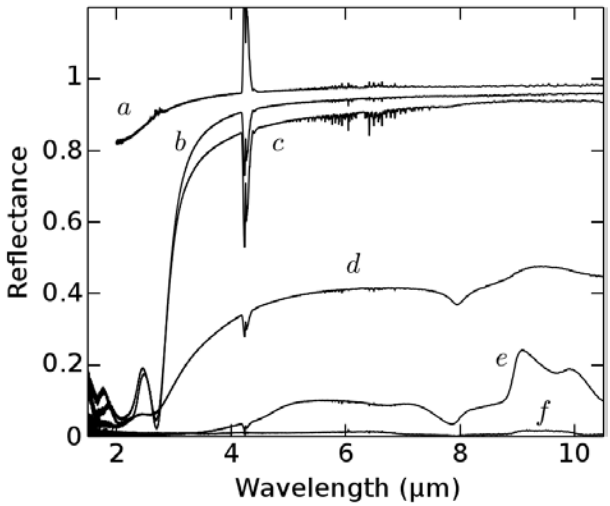


**Figure 5.9:** Reflectance of (a) Pt; (b) Pt-PhC after 8 hours at 1000 K in $N_2$ atmoshpere; (c) Pt-PhC with $SiO_2$ layer after 8 hours at 1100 K in $N_2$ atmosphere; (d) Pt-PhC without the thin $SiO_2$ layer after 8 hours at 1100 K in $N_2$ atmosphere; (e) Pt-PhC with $SiO_2$ layer after 12 hours at 1273 K in air; (f) Pt-PhC without the thin $SiO_2$ layer after 12 hours at 1273 K in air.

As it is observed, the optical properties of samples with a thin oxide layer between the silicon and the platinum showed to be thermally stable up to 1100 K, if a controlled $N_2$ atmosphere is maintained. Samples without the thin oxide degraded after the thermal annealing at 1100 K for 8 hours. All samples degraded beyond 900° (1173 K) no matter if the reduction atmosphere was maintained.

Fig. 5.9 also shows the resulting optical response when the metallic coating is destroyed. This is seen in the response of samples (e) and (f) after 12 hours annealing in air atmosphere at 1273 K.

We believed the interconnection of the metallic layer through millions of points in the structure brought more thermal stability to the samples in comparison with the sputtered ones, although a limit temperature is finally reached.

The degradation of the metallic layers, ALD coated or sputtered, could be observed at first glance as samples' surface turned black. This is consequence of the metallic layer agglomerating. In addition, once the metallic coating was destroyed, the underlying Si was exposed to oxidation and the thermal stress between the formed Si-$SiO_2$ layer bended the samples. This is shown in Fig. 5.10.

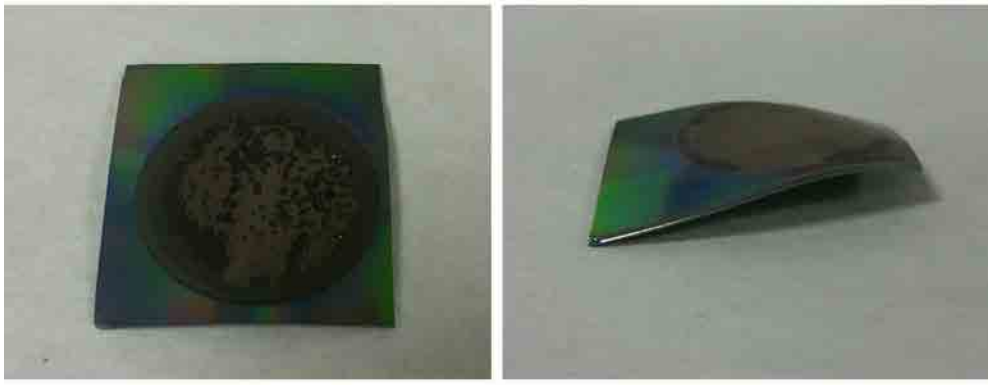

**Figure 5.10:** Degradation suffered by ALD-coated sample after 8 hours at 1200 K in air atmosphere.

The effect of metal agglomeration on the silicon's surface is shown in the SEM images of Fig. 5.11. The exposure of silicon after the Pt agglomerated in droplets is observed.

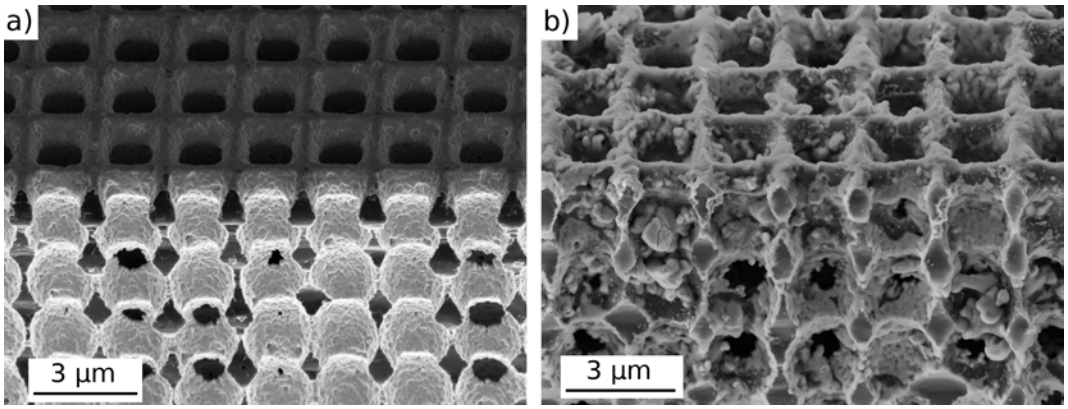


**Figure 5.11:** ALD coated mp-Si sample with platinum (a) previous and (b) after thermal annealing at 900°C for 8 hours.

# 6

# Conclusions & Future Work

In this thesis we have studied the thermal emission properties and the high temperature thermal stability of various macroporous silicon structures. Different modulations of pore diameter and different coating layers were analyzed looking for the most spectrally selective thermal radiation. Macroporous silicon was demonstrated to be a very versatile material that allows for cost-effective fabrication of large area 2D and 3D photonic crystals. Quasi-periodic structures could be produced just by changing the current profile during the electrochemical process. This versatility and the natural high refractive index of silicon makes of porous silicon an optimal candidate for engineering the radiant response of photonic structures. In addition, since crystalline silicon can withstand temperatures close to its melting point (1687 K) without structural deformation, it was used not only as selective emitter but a scaffold for 3D metallic structures.

Macroporous silicon PhC were demonstrated to be a material whose thermal radiation could be inhibited in the PBG region. By matching the optical response of these structures with the PV cell's $E_g$, expanding or contracting the scale of the crystals, the gap region can be placed into the out-of-band spectrum (energies below $E_g$) inhibiting the radiation of useless energy from the emitter.

Besides, the high emittance selective band, located between the primary and secondary gaps when three-dimensionality is reached in the porous structures, was centered in a spectral region slightly above $E_g$, making an hypothetic energy conversion in the PV cell more efficient.

To increase the selectivity of the thermal emitter, the working temperature was chosen so that the peak wavelength of the BB (Plank's curve) matched the selective band of the structure.

Experimental measurements, however, showed low emitter efficiency values in comparison with a BB radiator. This was a consequence of the narrow PBG region obtained in periodic structures. Therefore, macroporous silicon quasicrystals were proposed to span the PBG in order to increase the emitters' efficiency by suppressing thermal radiation in a wider spectrum within the out-of-band region. Although this objective was accomplished, fabrication proved to be a limiting factor to reach efficient emitters. Imperfections during the fabrication process made those structures to present a poor radiant response within the in-band spectral region, limiting the emitter's efficiency.

The main advantage of such structures is their high thermal stability. Samples were tested for days at 1473 K showing no degradation in the structure or the optical response when reduction atmospheres are utilized. In presence of $O_2$, however, it must be considered that oxidation effects can modify the emission spectrum as $SiO_2$ has particular absorption bands at some points of the MIR spectrum. In addition, thermal stress in the Si-$SiO_2$ interface can bend and break the sample.

To achieve the maximum inhibition of spontaneous radiation in the useless IR region of a TPV system, a different approach was also pursued, instead of suppressing (in the region $\lambda > \lambda_g$) the spontaneous radiation of a thermal element with a natural high emittance, we enhanced (in the region $\lambda < \lambda_g$) the thermal radiation of an element with a natural low emittance, like metals.

Metals arise as materials capable to work at high temperatures, beyond 2000 and 3000 K in the case of refractory metals, with a natural low emittance. Periodic metallic structures consisting in an array of microcavities can be designed to enhance emission at any desired frequency range by simply adjusting size and periodicity in the microcavities. Actually, there is no need for metallic structures as the large scattering coefficient of metals makes of very thin metallic coatings on dielectric scaffolds a composite that behaves entirely as a whole metallic structure.

A 50 nm coating of platinum on 3D macroporous silicon samples showed excellent selective emission properties, enhancing the radiant emission of the metal at wavelengths $< 3$ $\mu$m and leaving it at the natural low level below 0.2 emittance at larger

wavelengths. The shifting of the cut-off frequency with structure's periodicity was demonstrated. The achieved thermal efficiency doubled the one from the BB radiator.

The main drawback of such structures was found in their thermal stability at high temperatures. Although the structures were thermally stable up to 1073 K, the metallic coating degraded after continuous work at 1173 K. Degradation made the platinum layer to agglomerate and the optical selective response of the samples was lost.

## 6.1 Emitter Temperature, Selectivity and Efficiency

In this thesis, we have discussed so far that the working temperature of the emitter must be the one that makes the peak's emission of Planck's curve to match the selective emittance band of the photonic crystal. Although this is true in terms of improving the spectral selectivity of the radiated energy, it must be considered that the higher the temperature of the emitter the higher the emitted energy and, therefore, the electrical energy we can extract from an hypothetic TPV system. This is analyzed in this section.

Summarizing the results obtained in this work, Table 6.1 compares the three kind of analyzed selective emitters.

**Table 6.1:** Summary of results obtained on selective emission.

| **Emitter** | **$\lambda$ cut-off** | **Working T** | **$\eta_{SE}$** | **$\eta_{BB}$** |
|---|---|---|---|---|
| mp-Si PhC | 5.5 $\mu$m | 580 K | 0.34 | 0.38 |
| chirped PhqC | 6.5 $\mu$m | 500 K | 0.30 | 0.36 |
| Pt PhC | 3 $\mu$m | 1054 K | 0.66 | 0.32 |

We will center the analysis in the Pt crystals as the ones working at the highest temperatures in comparison with the mp-Si ones. These metallic PhC will be compared with the BB radiator, and two theoretical selective emitters named $SE_A$ and $SE_B$ which follow the below rules:

$$\epsilon_{SE_A} = \begin{cases} 1 & (\lambda < 3\mu m) \\ 0 & (\lambda > 3\mu m) \end{cases} \tag{6.1}$$

$$\epsilon_{SE_B} = \begin{cases} 0 & (\lambda < 2.5\mu m) \\ 1 & (2.5\mu m < \lambda < 3\mu m) \\ 0 & (\lambda > 3\mu m) \end{cases} \tag{6.2}$$

Fig. 6.1 shows the thermal efficiencies of the analyzed emitters as a function of the radiant temperature. These emitter efficiencies are compared with the theoretical efficiency that would be achieved in an ideal PV cell placed in front of such emitters at the different radiant temperatures. Here, emitter efficiency was calculated as defined, the ratio between the in-band to the total emitted power, and the PV efficiency was taken considering that half of the produced photons in the emitter reach the PV converter and half are recycled into the thermal emitter.

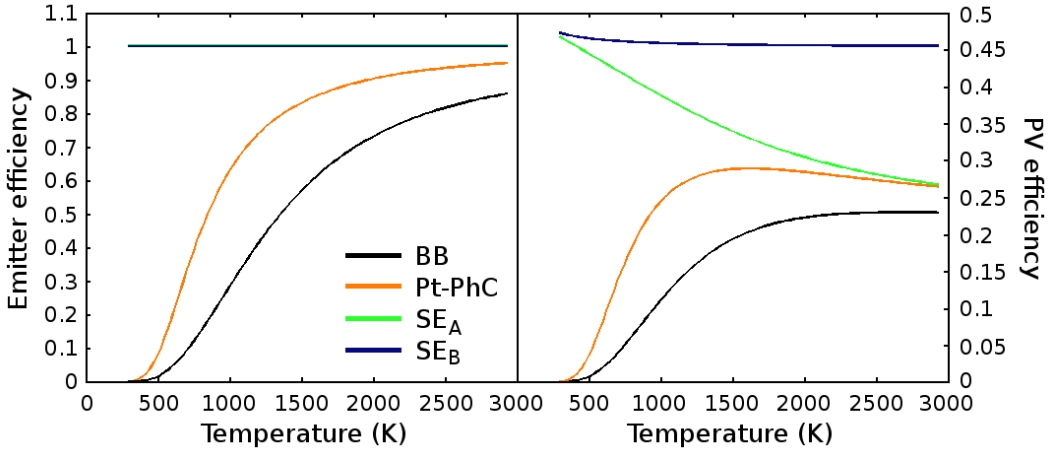


**Figure 6.1:** Emitter and photovoltaic efficiencies as a function of emitter's temperature for different configurations: a BB source, the fabricated platinum-PhC and the theoretical selective emitters $SE_A$ and $SE_B$.

As it is observed in Fig. 6.1, the platinum PhC have always a better emitter efficiency than the BB source, independently of the working temperature. This is due to the low emittance of the metal in the out-of-band spectral region ($\lambda > 3\mu$m). In these emitters, the efficiency increases with temperature due to the production of a higher amount of high energy photons at wavelengths $\lambda < 3$ $\mu$m, following the Planck's law. On the other hand, selective emitters $SE_A$ and $SE_B$ show 100% efficiency at all temperatures as the emittance of these theoretical emitters is completely suppressed at wavelengths beyond 3 $\mu$m.

Considering these emitters as input radiation sources to a theoretical and ideal PV cell with gap wavelength $\lambda_g = 3$ $\mu$m, we observed in Fig. 6.1 how the PV efficiency decreases with temperature. Higher temperatures penalize the conversion efficiency in the cell as the production of high energy photons far away $E_g$ produce an excess of optical energy which is not converted into electricity.

Again, the platinum PhC produce higher conversion efficiencies than the BB source at all temperatures. Note the selective radiation spectrum of the metallic emitter allows it to work at lower temperatures, as the Pt emitter reaches a maximum PV conversion efficiency at 1600 K, while the BB source needs to work at 2700 K to achieve its maximum. This behavior has a limit in the theoretical selective emitter $SE_A$ which is capable to emit like a BB at wavelengths $\lambda < 3$ $\mu$m, and completely suppress radiation above it. In this case, it is observed the highest conversion efficiency is reached at the lowest working temperature, decreasing as the temperature goes up.

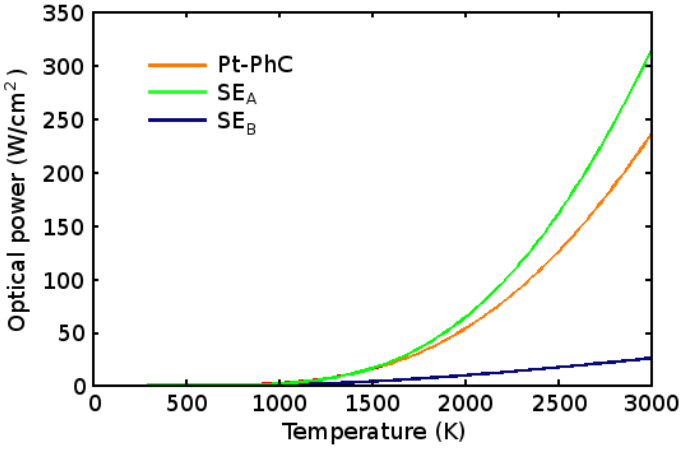


**Figure 6.2:** Emitted power as a function of emitter's temperature for the platinum-PhC and the theoretical selective emitters $SE_A$ and $SE_B$.

Finally, it is worth mentioning that the ideal selective emitter $SE_B$ which emits in a very narrow spectral region achieves the maximum PV conversion efficiency. This is maintained for all temperatures. This thermal source, which resembles the optical behavior of rare earth oxides, finally emits a very low optical power in comparison with the Pt selective emitter or the ideal emitter $SE_A$. This is shown in Fig. 6.2.

So, as it was commented in the beginning of the conclusions, a trade-off should always be considered when designing a SE for TPV applications.

## 6.2 Future Work

From the presented results, three main research lines arise to be followed to complete the study which has been carried out in the thesis work:

1. The fabrication of macroporous silicon structures with precise control of pore modulation is still challenging. This must be improved, especially in the presented quasi-crystals, in order to achieve the highest spectral inhibition of spontaneous radiation within the PBG region, while maintaining a maximum emittance outside.

   The big advantage of silicon PhC is the high thermal stability at high temperatures close to silicon's melting point. However, to take profit of this, the sizes of the structures must be reduced. By shrinking the fabricated crystals, the PBG region will shift to lower wavelengths and the emitter's working temperature will increase as the cut-off frequency increases.

   Pursuing this objective of shrinking the PhC sizes to shift the gap, an interesting research line was initiated on self-assembled colloidal structures. These structures allows to tune the optical properties in an easier way by simply choosing the proper size of the colloids. The advances reached during this thesis are presented in Appendix A. We preferred not to include them in the main text as no thermal radiation measurements were possible to be obtained so far.

2. Metallic photonic structures are highly selective. Their spectral region of enhanced emittance can be easily shifted to match any desired frequency band and various techniques can be utilized to fabricate the crystals.

   The main drawback of such structures is their thermal instability beyond 1100 K. Some researchers have reported on the improvement on thermal stability of metallic microstructures by the coating with a thin $HfO_2$ layer.[49,50]

   It would be desirable to investigate it to check the feasibility of our platinum structures to work at higher temperatures in presence of oxygen.

   Besides, metallic microcavities reported in the literature refer to cylindrical or cubic etched holes by means of, for instance, RIE technique. In our approach, microcavities start with an inversed pyramid configuration followed by a complex

3D porous structure. More research must be conducted to analyze in depth the effect of the macroporous array.

3. An important property of thermal sources is that they radiate following a Lambertian pattern, i.e. they radiate at all angles following a $\cos^2\theta$ distribution. It is known the radiation pattern of an emitting surface can be modified by the structuring of a diffraction grating.

   We propose to investigate this in our selective emitters in order to focus the radiated energy in a directive way into the PV converter.

# Appendix A

# Selective Emitters based on Self-Assembled PhC

Self-assembled photonic crystals offer a huge versatillity in terms of materials and crystal periodicity. Dozens of different colloids have been synthesized in the last years by the chemical industry capable to behave as photonic crystals through any of the various self-assembly tecniques. This allows to easily tune the optical properties of such structures in the whole optical range by simply controlling the size of the colloids.

The process of self assembly of finely divided materials is seen from the perspective of the arrangement into ordered structures like PhC. Contrary to mp-Si structures, whose pattern is fully controlled during the fabrication process, minimizing the residual disorder in colloidal self-assembled crystals is a major goal. This is never fully accomplished and a partial disorder is always present diminishing the optical response of the crystals. On the other hand, the size of colloids can be almost arbitrarily chosen to obtain 3D self-assembled crystals (namely opals) with optical properties in any spectral region.

Among the wide variety of techniques for PhC fabrication based on self-assembled structures, two techniques will be presented in this appendix as a result of the collaborations undertaken during the realization of this thesis. In collaboration with the ICMM, with the *Alvaro Blanco*'s group, the *Vertical Deposition Method* was characterized. In collaboration with *PhD Arnau Coll*, from the MNT group of the UPC, the *Electrospray Technique* was characterized.

A review in colloids fabrication can be found elsewhere.[59]

## A.1 Experimental

We must state that the synthesis of direct and inverse opals was achieved in collaboration with the previously mentioned research groups. The characterization of such structures is the scope of the thesis.

### A.1.1 The Vertical Deposition Method

Vertical deposition has become the most widespread method to grow self-assembled photonic crystals, specially when a thick sample is to be grown (as for instance opaline structures). Denkov et al.[115] first developed this method for monolayers and it has been extended to 3D opal based PhC, specially since 1999.[116]

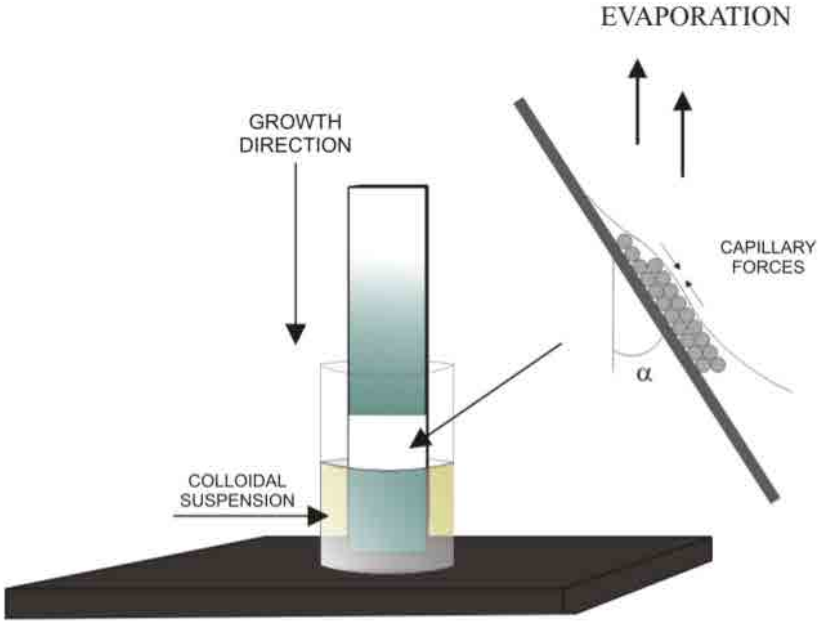


**Figure A.1:** Diagram of the vertical deposition method.

The standard procedure to grow the crystal consists in placing a flat substrate in a vial containing the colloidal suspension of monodisperse spheres (see Fig. A.1). A meniscus is formed at the interface between the substrate, the air and the liquid. At the point where the meniscus is thinner than the diameter of the spheres these are pulled against the substrate and between them by capillary forces and the ordering process begins.[117] As evaporation takes place, the flow of solvent to the meniscus moves the

spheres to the growth region and incorporates them to the lattice. As the solvent evaporates the lattice of spheres remains over the substrate forming the self-assembled structure. If the concentration of spheres is high enough a 3D structure will be grown which total amount of layers will be mainly dependent on the concentration of the dispersion.[117] An example of the obtained structures is shown in Fig. A.2.

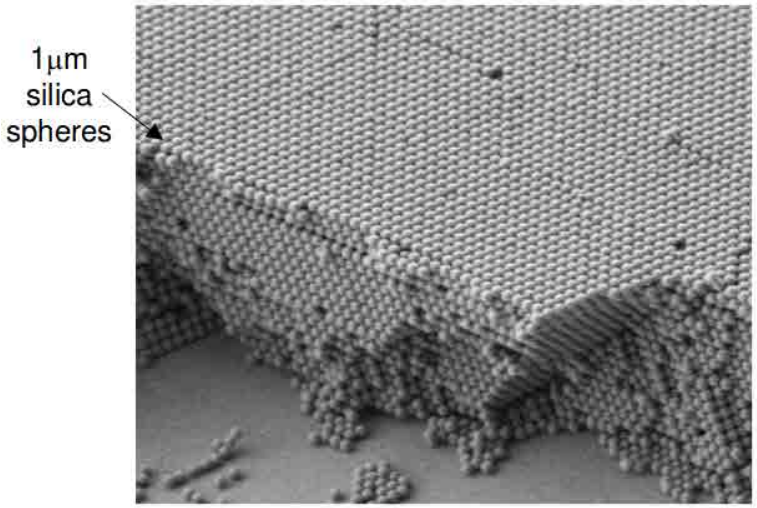


**Figure A.2:** SEM image of the resulting opaline structure obtained employing the vertical deposition method.

As it can be deduced from the mechanism explained, the main parameters determining the appropriate growth are the colloidal suspension concentration and the temperature and humidity of the environment. The later two account for the growth velocity of the lattice and the first one determines the thickness of the main structure, though all parameters have some effect on growth velocity and sample quality.

Samples were fabricated by vertical deposition method using slides of Si wafers of approximately 1x2 $cm^2$. The slides were plunged into glass vials filled with chromic mixture. This methodology allows the hydrofilization of the silicon and the vials' walls so that later the colloids may adhere easily.

This method was used to form $SiO_2$ opals. The silica precursor consisted of a mixture of ethanol, hydrochloric acid and tetraethyl orthosilicate which, for convenience, will be named TEOS from now on. A volume of 9.75 ml of distilled water was mixed with 50 $\mu$l of TEOS and 250 $\mu$l of commercial spheres' suspension.

The as prepared colloids were homogenized in an ultrasound bath for few seconds. The vials were placed in a climatic chamber, with 20% humidity, and the Si substrate suspended inside at 45°. The crystal is formed after approximately 62 hours.

### A.1.2 Electrospraying Colloidal Structures

Electrospray technique consists in producing a fine aerosol by dispersion of a liquid by application of a high electric field between an emitter, usually a thin needle, and a flat electrode. Above a given voltage threshold, a Taylor cone develops[118] and the liquid tip becomes unstable, breaking into small droplets. Finally, only the colloids reach the target surface, with no presence of water, and get ordered by the electrostatic forces present among the charged particles. Using this technique, tens of 3D-ordered layers can be formed in few minutes over areas of centimeters with good optical quality behaving as PhC.[119]

In the electrospraying deposition of particles on a substrate, several forces and physical phenomena are involved. In the short range, electrostatic forces are important, in addition to surface tension and capillarity, to explain particle adhesion to surfaces and particle self-assembly. Coulombic and multipolar dielectrophoretic forces contribute to the total force acting on the particles,[120] which depends on the values of the permittivity of the particle and of the medium.

The first efforts are devoted to get a stable Taylor cone at the tip of the needle. This involves optimizing the distance between the needle and the substrate and changing the bias conditions. A stable cone is created when the distance is typically between 10 to 15 cm and the applied voltage $> 7.5$ kV.

The electrospray setup consists of an infusion pump, a 5 ml syringe, a Hamilton needle of 130 $\mu$m inner diameter and a high-voltage bipolar source between 15 to +15 kV. The target deposition area is placed inside a glove box with controlled $N_2$ atmosphere. Humidity is controlled $< 20\%$. Figs. A.3 and A.4 show an schematic of the experimental setup and SEM images of the typical structures that are obtained.

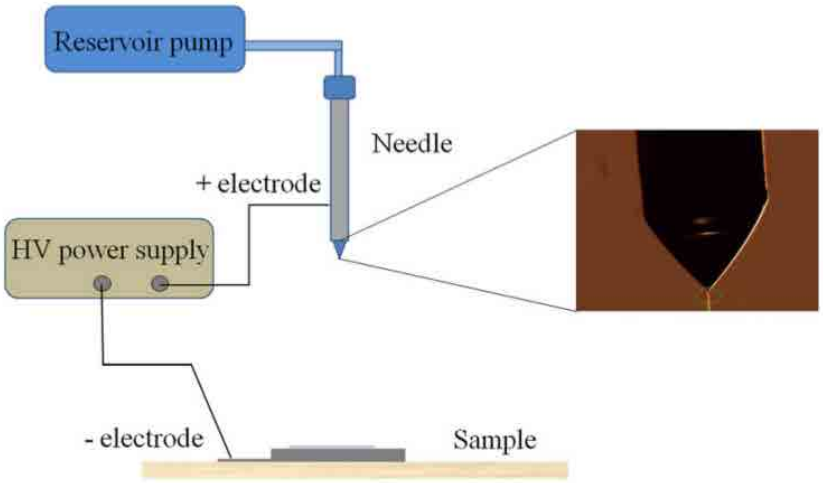


**Figure A.3:** Schematic view of the electrospray setup. The enlarged image shows the tip of the needle with a Taylor cone and a jet of 4 $\mu$m. Extracted from [119].

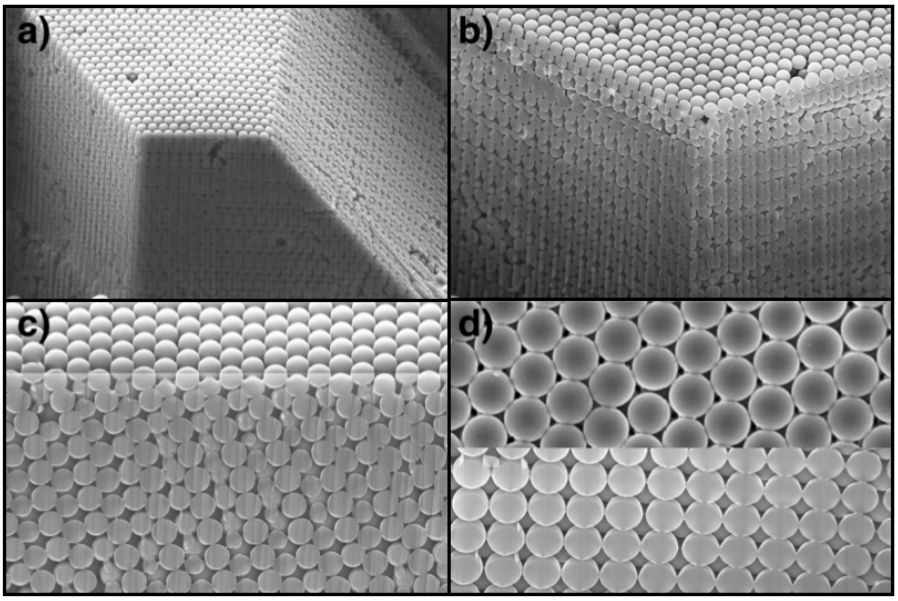


**Figure A.4:** SEM images of the resulting colloidal crystals obtained from polystyrene nanoparticles solution. Extracted from [119].

A thin layer of typically 100 nm of aluminum or ITO was patterned on the substrates' surface by a lithographic and subsequent lift-off process. The metallic patterns concentrates the electric field of applied voltage and, therefore, become the target for electrospray deposition. These samples were used for the deposition of polystyrene

opals.

It is worth mentioning that no effects on the order of the deposited layers are found by just changing the solution concentration or the material present in the dissolution. Once the conditions to get a stable Taylor cone are satisfied, only the pumping rate and solution conductivity seem to play an important role on the final 3D-ordered structure.

### A.1.3 Inverse Opals

Bare opals, either common $SiO_2$- or polymer-made, are frequently used as templates for the production of replicas in different nanomaterials for a number of distinct applications. This is due to the fact that opals' low dielectric contrast provides weak photonic effects, and they cannot open a full PBG.

When Sözüer et al.[121] demonstrated the existence of a full PBG for FCC lattices providing a dielectric contrast $> 8.7$, the challenge was to modify the materials composing the opals to fulfill those requirements. This was finally achieved in silicon inverse opals.[122]

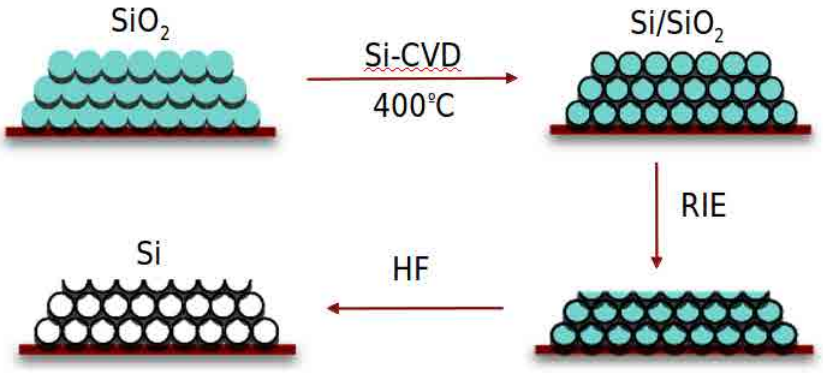


**Figure A.5:** Schematic of the inverse opal formation process: (a) self-assembling of polymer beads; (b) the template is infiltrated by CVD or ALD; (c) the original structure is reached; (d) template is etched away.

Fig. A.5 shows an schematic of the fabrication process of inverse opal structures from FCC templates. Made of polystyrene or $SiO_2$, the template is infiltrated with a thin layer of Si or $SiO_2$, typically, by Chemical Vapour Deposition (CVD) or ALD. These techniques produce very conformal layers around the spheres of the template, with very accurate thickness control. Afterwards, the template can be removed by calcination (if plastic templates are used) or a short dip in HF solution (if $SiO_2$ beads

are utilized). This finally gives the inverse opal structure in the infiltrated material as a result.

This technique pursues improving the optical response of the self-assembled PhC by modifying the dielectric contrast. In addition, the inverse opal technique from templates allows to choose the deposition material (within the limitations of CVD and ALD techniques). A SEM image of the final inverse opal structure that is obtained is shown in Fig. A.6.

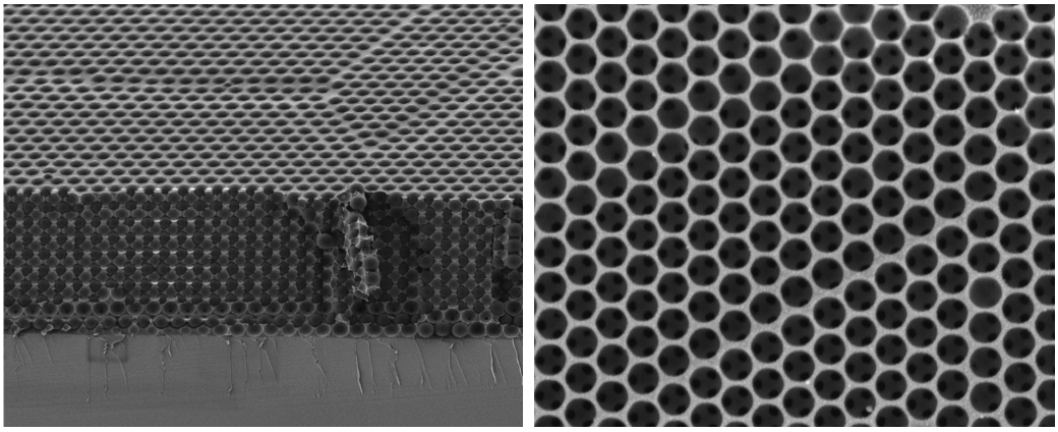

**Figure A.6:** SEM images of Si inverse opal structures synthesized by chemical infiltration techniques such as ALD.

It can be appreciated that the opallic structure is preserved in spite of the treatments the samples are subjected to. The typical area of the crack-free opal depends on the fabrication technique of the original opal.

## A.2 Optical Properties

Bandgaps tend to appear in structures with a high dielectric contrast. The more significant the scattering of light, the more likely a gap will open up. This is hard to find in three-dimensional crystals, where complete PBG are rare. The gap must smother the entire three-dimensional Brillouin zone, not just any one plane or line. For example, macroporous silicon crystals did not open complete 3D gaps but OTR bands, and this required achieving a very high porosity in the structures.

In case of opal structures, an FCC lattice of close-packed dielectric spheres in air does not show complete PBG no matter how large the dielectric contrast is (e.g. with silicon spheres, $\varepsilon = 13$). However, the same dielectric spheres organized following a diamond structure shows a complete PBG with a 29% gap-midgap ratio when the diameter of the spheres is 65% the lattice constant.[39]

The structures analyzed in this thesis, fabricated by either the vertical deposition method or electrospray, showed a combination of FCC and Hexagonal Close-Packed (HCP) lattices. Fig. A.7 shows an schematic of the lattices for a better understanding.

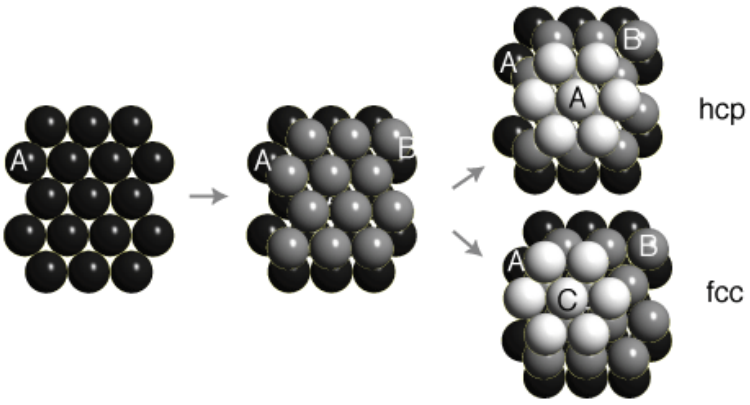


**Figure A.7:** FCC and HCP lattices. A combination of both is present in the analyzed self-assembled PhC.

The quality of the samples finally obtained refers to how much the real structure differs from the ideal lattice, diminishing the optical response (i.e. the quality of the obtained PBG). In addition to the mix of lattices, the most common experimental sources of disorder in the final self-assembled structures are: vibrations during fabrication, temperature changes and the tolerances in the initial sizes of the colloids. Such can

lead to different thicknesses within the sample, producing separations between different domains of the structure (cracks).

These cracks were especially found in the samples prepared by the vertical deposition method. The electrospray technique allowed for a more uniform assembly of the colloids. In addition, larger areas and higher thicknesses were obtained with this technique easing the optical characterization of the samples. Hence, the analysis was centered in the samples obtained by electrospray technique, discarding the $SiO_2$ opals and the subsequent silicon inverse opals obtained by the vertical deposition method.

*It is not the intention of this work to compare or analyze the pros and cons of the different fabrication methods for self-assembled crystals. Our pretensions are to characterize the feasibility of using such structures as selective thermal emitters.*

Fig. A.8a shows the reflectance of a colloidal crystal with 360 nm polystyrene nanoparticles. As it is observed, a gap region turned up at the vicinity of 950 nm wavelength peaking 0.8 reflectance. The peak reflectance and the bandwidth of the obtained gap was a bit worse than what it was obtained for periodic mp-Si samples due to the commented disorder found in self-assembled structures. However, the advantage is that the spectral NIR position is easily reachable with the technology.

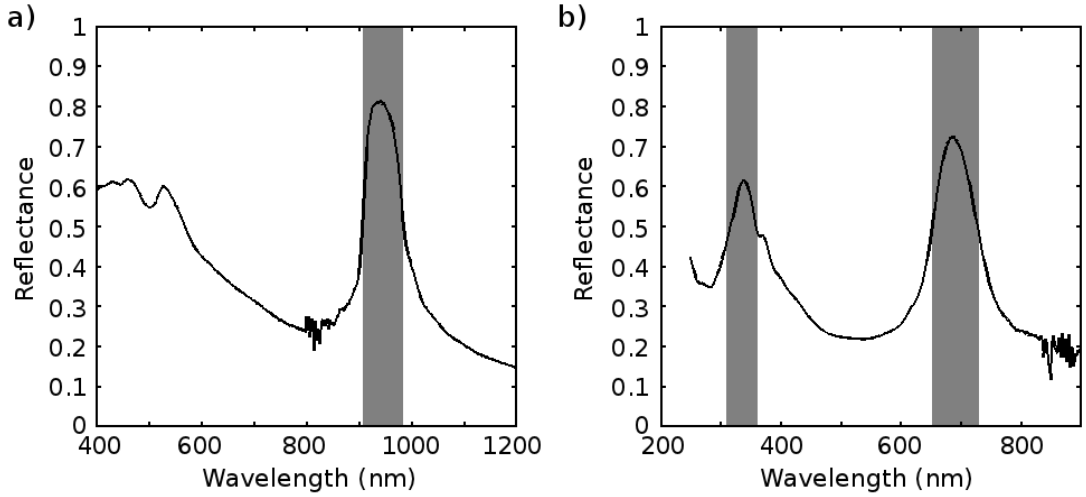


**Figure A.8:** Reflectance at normal incidence, using an integrated sphere for the measurements, of (a) self-assembled 360 nm polystyrene nanoparticles and (b) its corresponding $Al_2O_3$ inversed opal.

However, polystyrene nanoparticles are not capable to withstand with high temperatures. Hence, colloids were post-processed by ALD of $Al_2O_3$ and calcination in order to obtain alumina inverse opals (capable to work at high temperatures). The reflectance of the alumina inverse opal is shown in Fig. A.8b. The primary gap shifted from 950 nm to ∼700 nm wavelength, and a secondary gap arose at around 330 nm wavelength. This gap evolution is equivalent to the one obtained for mp-Si structures in section 4.2.1 when the porosity of those macroporous structures were increased. Here, the increase in porosity is reached by making the inverse structure from the opals.

## A.3 Conclusions

Self-assembled structures and their derived inverse opals bring the optical properties of PhC to the NIR and visible spectral regions in the simplest fabrication manner. Very large ordered areas and high thicknesses can be obtained with the different available fabrication techniques. Future research is needed to characterize the fabricated opals and inverse opals at high temperature. However, some conclusions can be extracted form the observed reflectance patterns.

In the reflectance we observed the same drawback described for periodic mp-Si PhC: a small bandwidth that would provoke very low efficiencies in comparison with BB radiators due to the small spectral region where spontaneous emission would be inhibited in such samples.

Despite the ease for obtaining tunable PBG by just adjusting the size of the colloids, we may think in a way of expanding the bandwidth of these PBG to increase efficiency in the suppression of samples' radiation. PhqC structures equivalent to the ones analyzed in section 4.3 are proposed by a sequential deposit of colloids with different particles size.

# Appendix B

# High Temperature Characterization Setup

Fig. B.1 shows a general view of the temperature characterization setup. The central element is the FTIR spectrometer (1). The spectrometer analyzes the radiation coming from the samples which are heated outside. Two heaters were used during the realization of the thesis, a low-temperature one (2) which attaches to the backside of the FTIR, and a high-temperature one (3), calibrated by a BB system (4). The high-temperature setup requires an optical path composed of gold mirrors (5) to focus the radiation of the samples into the spectrometer.

As it was already commented in section 3.3, the FTIR spectrometer is a Bruker Vertex 70 with the detectors, filters and beam splitters required to analyze the IR spectrum from 0.7 to 25 $\mu$m wavelength.

Heaters are zoomed in Fig. B.2. The low-temperature heater (2) is an accessory of the Bruker's FTIR spectrometer that is screwed in a rear window of the interferometer. Samples are clamped onto a heating surface which is inside the observed ceramic case $C$. The radiation of the heated samples comes out through the circular aperture $A$ which is observed in the middle of the ceramic case. This low-temperature heater reaches 673 K. The calibration of the measure is done with a piece of polished silicon, or a thin layer of carbon, whose thermal radiation is known beforehand.

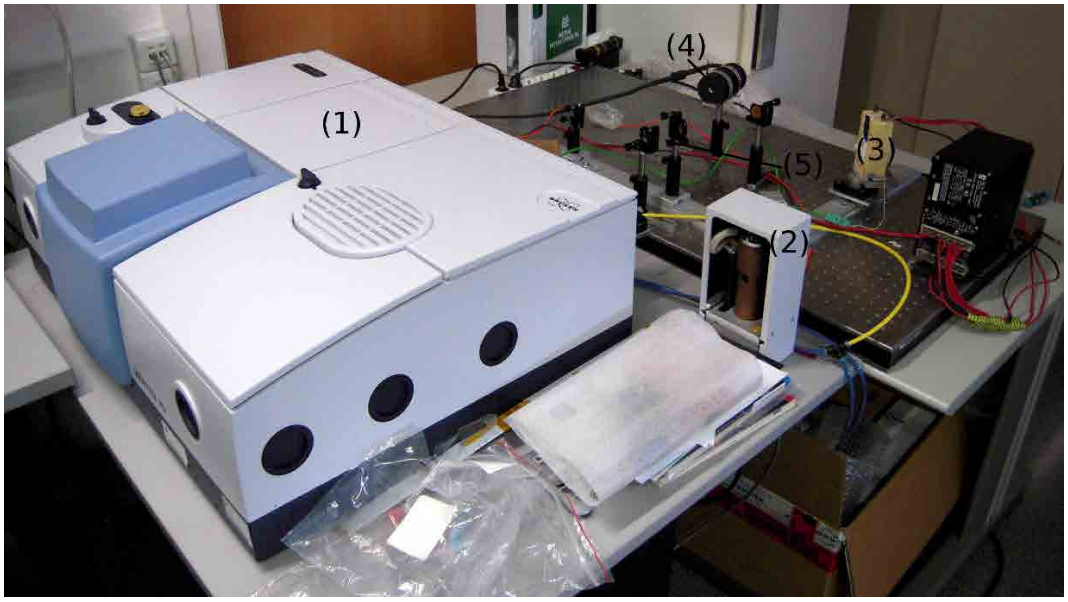


**Figure B.1:** Temperature characterization setup: (1) FTIR; (2) low-temperature heater; (3) high-temperature heater; (4) BB; (5) optical path.

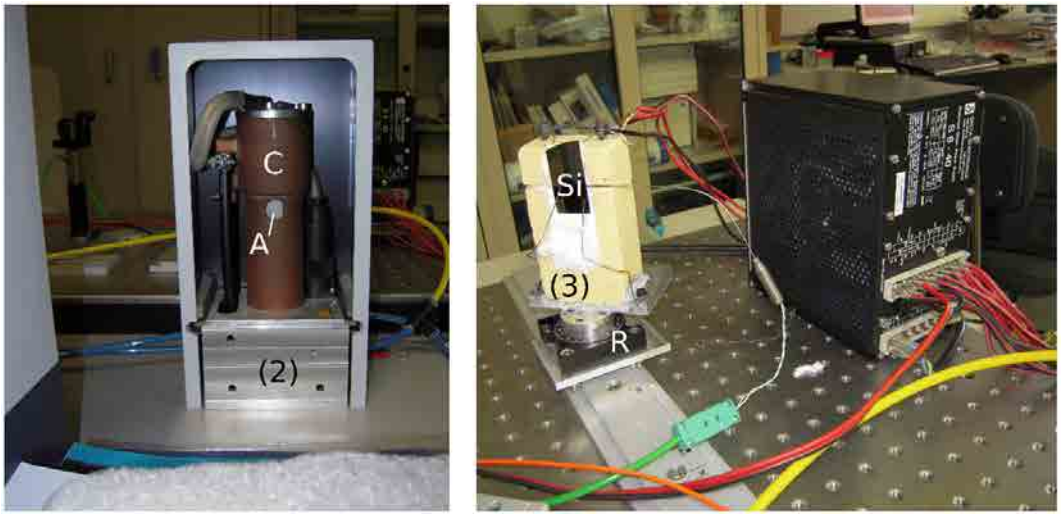


**Figure B.2:** Low temperature heater (left). High temperature heater (right).

The high-temperature heater (3), which is managed on an optical board, is a hand-made piece of $ZrO_2$ with an electrical *Ni-Cr* resistance clamped on its surface. A temperature-uniforming metallic surface is put in contact of the resistor and samples are put in contact with this metallic surface in order to receive the heat. A piece of

silicon is observed in the heater in Fig. B.2.

The resistor is connected to a high current source and, although it can be heated up to 1373 K, heat losses in the samples and in the metallic surface used to distribute the heat uniformly, limit the maximum temperature to be reached on samples' surface to 1073 K. In addition, this high-temperature heater is capable to manually resolve the angular radiation of the emitter as the $ZrO_2$ case is screwed on top of a rotation platform $R$.

The calibration of the samples' radiation coming from the high-temperature heater is performed using a true BB source (zoomed in Fig. B.3). It is an Infrared System Corporation's IR-519 with $> 0.99$ emittance from 0.5 to 99 $\mu$m wavelength. The BB is put on the optical board at the same distance of the spectrometer's rear windows as the high-temperature heater is. This way, we can assure the light coming from both sources, the sample and the BB, will suffer an equivalent atmospheric absorption and the same attenuation with distance.

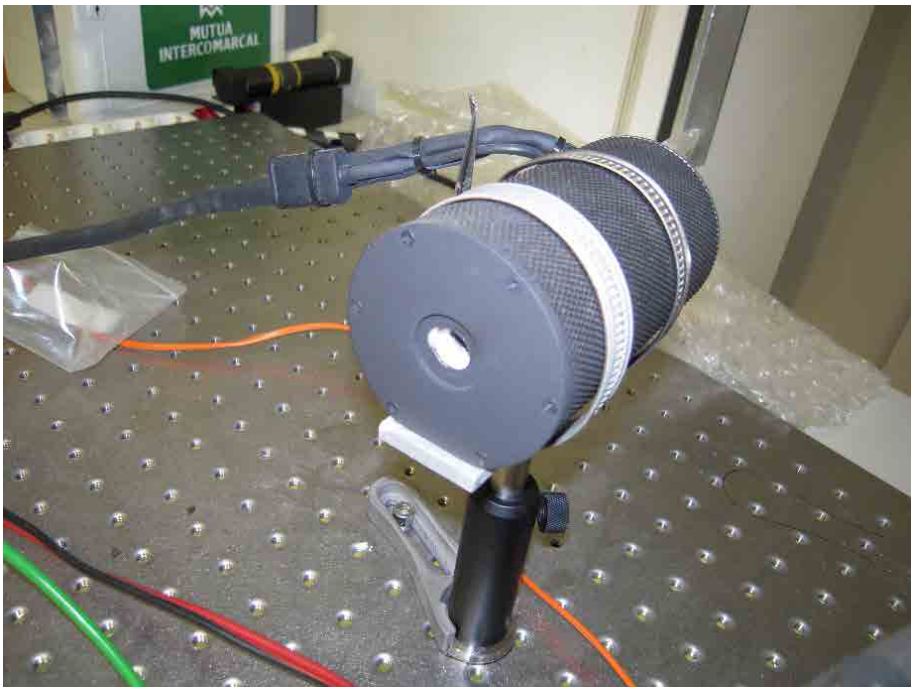


**Figure B.3:** IR-519 BB system.

Finally, the optical path focuses the radiation coming from the samples and the BB system into the Bruker's FTIR spectrometer. As it is observed in Fig. B.4, the optical path is composed of gold mirrors $M$, capable to direct IR radiation with the minimum losses, and an iris aperture $I$ in front of the rear window of the spectrometer, to define the radiation area which enters the FTIR. Iris position is controlled with an XYZ microtranslation stage. Iris aperture can be controlled from 1 to 12 mm.

*Note a piece of carton is placed behind the iris covering any other possible incoming path for external radiation.*

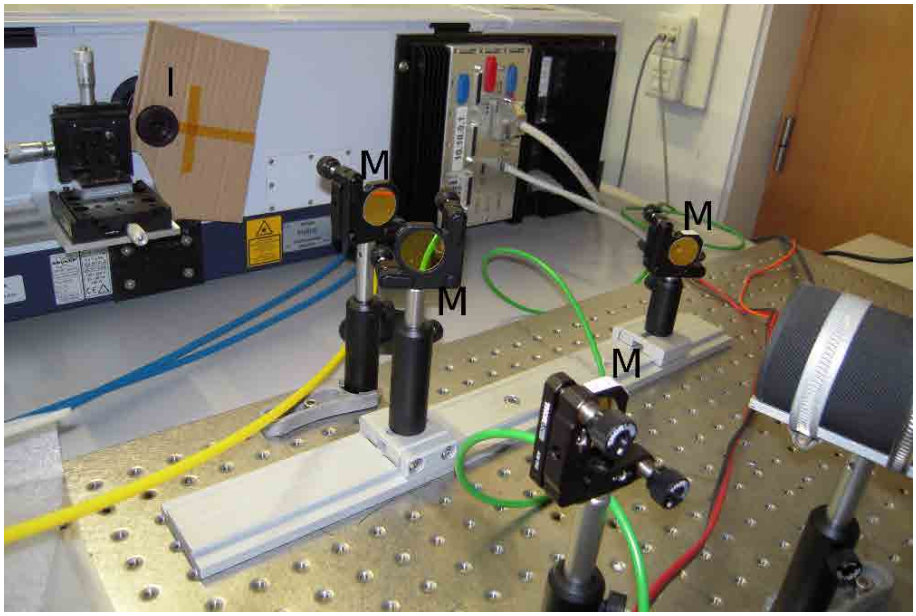


**Figure B.4:** Gold mirrors and a micropositioned iris are utilized to focus the radiation of the samples into the FTIR spectrometer with controlled analysis area.

## B.1 On Measuring Samples' Surface Temperature

Two main challenges were faced during the design of the high-temperature setup: how to heat samples to high temperatures and how to measure the temperature at which samples were.

The first challenge was faced as a conductivity problem. Heat can flow through conduction, convection or radiation. The most effective transfer is reached by conduction when a hot and a cold material are put in contact. Heat, like electricity, tends to flow through thermal conductive materials while its flow is reduced in thermal insulator elements. This way, the electrical resistor that acts as the heater of the system is completely insulated by the $ZrO_2$ ceramic and rockwool, except for the contact points with the metallic plate which acts as thermal distributor to uniform the heat. At the same time, during measurements, the characterized samples are bigger in area than the metallic plate, in order to avoid heat dissipation in the plate.

With this configuration, the center of the characterized samples is always hotter than the edges of the samples. This is not a problem as PhC are always fabricated in the middle of the samples and the remaining area is just a support.

The second challenge is far more difficult to solve. Typically, there are two ways of measuring the temperature of a body: by contact or contactless techniques. Contactless techniques are based in the Planck's principle that relates the temperature of the body with the peak emission wavelength of its radiation spectrum. As PhC are indeed deemed to the modification of their emission spectrum, contactless techniques will report wrong temperature measurements.

Contact techniques, at high temperatures, are based in the electrical properties of two different conductors put in contact on the hot surface. The device is called thermocouple. The main drawback of thermocouples is that we never read the temperature of the body but the temperature at which the thermocouple is:

- By placing the thermocouple on the surface of the hot sample, half of the thermocouple is in contact with air and half is in contact with the sample. The final measure is an average of temperatures and the thermocouple reports a much lower temperature than the real one at which the sample's surface is.

- By placing the thermocouple between the sample and the metallic plate, we obtain a far more accurate measure of the sample's surface temperature. However, two additional problems arise: first, when we heat the metallic plate we generate an electrical current by Seebeck effect which will be collected by the thermocouple distorting the measure of the temperature; second, we are actually separating the sample from the metallic plate, loosing efficiency in the conductive transfer of heat and decreasing the final temperature in the sample's surface.

  The first challenge was easily overcome by oxidizing the plate before its usage.

- By placing the thermocouple on the metallic plate's rear surface we do not distort the heat transfer. However, the measured temperature is again far away the correct one.

Finally, the most accurate process to measure samples' temperature was the use of an indirect calibration with the BB system and a piece of silicon of the same size than the sample we pretended to characterize. In a first phase, we heat the piece of silicon to a predefined temperature controlled by the thermocouple. As the emissivity of silicon is known, we obtain the real temperature at which the silicon sample's surface is by calibrating with the BB source (whose temperature is considered genuine and therefore is taken as reference). In a second phase, the sample to be measured is placed instead and the same temperature is reached, controlled again by the thermocouple placed exactly at the same position that during the calibration phase.

# Scientific Contributions

## Journal Articles

**D. Hernández**, D. Lange, T. Trifonov, M. Garín, M. García, A. Rodríguez and R. Alcubilla, *3D metallo-dielectric structures combining electrochemical and electroplating techniques*, Microelectronic Engineering **87**:1458-1462, 2010.

M. Garín, T. Trifonov, **D. Hernández**, A. Rodríguez and R. Alcubilla, *Thermal emission of macroporous silicon chirped photonic crystals*, Optics Letters **35**:3348-3350, 2010.

**D. Hernández**, M. Garín, T. Trifonov, A. Rodríguez and R. Alcubilla, *Emissive properties of $SiO_2$ thin films through photonic windows*, Applied Physics Letters **100**:091901, 2012.

A. Coll, S. Bermejo, **D. Hernández** and L. Castañer, *Colloidal crystals by electrospraying polystyrene nanofluids*, Nanoscale Research Letters **8**:26, 2013.

**D. Hernández**, T. Trifonov, M. Garín and R. Alcubilla, *"Silicon millefeuille": From a silicon wafer to multiple thin crystalline films in a single step*, Applied Physics Letters **102**:172102, 2013.

## Patents

Alcubilla González, Ramon, **Hernández García, David**, Trifonov, Trifon, Garín Escrivá, Moisés, *"Procedimiento para la obtención de múltiples capas de silicio cristalino a partir de una oblea de silicio"*, ES2438415 A1, 16 de Enero de 2014.

## Communications

**D. Hernández**, D. Lange, T. Trifonov, M. Garín, M. García, A. Rodríguez and R. Alcubilla, *Template fabrication of 3D metallic microstructures by electrochemical etching and electroplating*, 6th Rencontre Chimique et Physique de l'État Solide (March 17-19, 2010, Tarragona, Spain).

**D. Hernández**, T. Trifonov, M. Garín and R. Alcubilla, *Controlling the optical properties of macroporous silicon structures*, II Conferencia Española en Nanofotónica (June 15-18, 2010, Segovia, Spain).

**D. Hernández**, T. Trifonov, M. Garín, D. Vega, A. Rodríguez and R. Alcubilla, *Optical properties of $Al_2O_3$ and $TiO_2$ coated 3D macroporous silicon photonic crystals*, 8th Spanish Conference on Electron Devices (February 8-11, 2011, Mallorca, Spain).

**D. Hernández**, T. Trifonov, M. Garín, A. Rodríguez and R. Alcubilla, *Macroporous silicon structures in thermophotovoltaics*, EMRS 2011 Spring Meeting Bilateral Energy Conference (May 9-13, 2011, Nice, France).

**D. Hernández**, A. Blanco and R. Alcubilla, *Inverse opals as highly efficient thermal emitters*, Meeting of the Nanophotonics for Energy Efficiency (N4E) Network of Excellence (June 1-2, 2011, Stockholm, Sweden).

**D. Hernández**, M. Garín, T. Trifonov and R. Alcubilla, *Selective emission properties of macroporous silicon microstructures*, Eurotherm91 -Microheat Transfer III- (August 29-31, 2011, Poitiers, France).

A. Coll, **D. Hernández**, S. Bermejo, A. Blanco, J. F. Galisteo-López, C. López, L. Castañer and R. Alcubilla, *Angle emission properties of complex colloidal nanostructures for energy efficiency applications*, III Conferencia Española en Nanofotónica (CEN 2012) (October 1-4, 2012, Carmona, Sevilla, Spain).

# References


[1] D. C. White, B. D. Wedlock, and J. Blair. **Recent advance in thermal energy conversion**. In *Proc. 15$^{th}$ Power Sour. Conf.*, pages 125–132, 1961.

[2] B. D. Wedlock. **Thermal photovoltaic effect**. In *Proc. 3$^{rd}$ IEEE Phot. Spec. Conf.*, number III, pages A4.1–A4.13, 1963.

[3] V. P. Khvostikov, V. D. Rumyantsev, O. A. Khvostikova, et al. **Thermophotovoltaic cells based on low-bandgap compounds**. In *AIP Conf. Proc.*, number 738, pages 436–444., 2004.

[4] C. H. Henry. **Limiting efficiencies of ideal single and multiple energy gap terrestrial solar cells**. *J. Appl. Phys.*, **51**:4494–4500, 1980.

[5] J. M. Gee, J. B. Moreno, S.-Y. Lin, and J. G. Fleming. **Selective emitters using photonic crystals for thermophotovoltaic energy conversion**. In *Proc. 29$^{th}$ IEEE Phot. Spec. Conf.*, pages 896–899, 2002.

[6] P. Bermel, M. Ghebrebrhan, W. Chan, et al. **Design and global optimization of high-efficiency thermophotovoltaic systems**. *Opt. Express*, **18**:A314–A334, 2010.

[7] Alejandro Datas Medina. *Development of solar thermophotovoltaic systems*. PhD thesis, Universidad Politécnica de Madrid, 2011.

[8] M. Planck. *The theory of heat radiation*. P. Blakiston's Son & Co., Philadelphia, U.S., 1914.

[9] C. Schlemmer, J. Aschaber, V. Boerner, and J. Luther. **Thermal stability of microstructured selective tungsten emitters**. In *AIP Conf. Proc.*, number 653, pages 164–173, 2002.

[10] S.-Y. Lin, J. G. Fleming, D. L. Hetherington, et al. **A three-dimensional photonic crystal operating at infrared wavelengths**. *Nature*, **394**:251253, 1998.

[11] L. Broman. **Thermophotovoltaics bibliography**. In *Prog. Photovolt: Res. Appl.*, number 3, pages 65–74, 1995.

[12] J. Werth. **Operation of photovoltaic cells at high power densities**. In *Proc. 3rd IEEE Phot. Spec. Conf.*, number II, pages A6.1–A6.3, 1963.

[13] W. Shockley and H. J. Queisser. **Detailed balance limit of efficiency of p-n junction solar cells**. *J. Appl. Phys.*, **32**:510–519, 1961.

[14] A. E. Becquerel. **Mémoire sur les effets électriques produits sous l'influence des rayons solaires**. *C. R. Acad. Sci.*, **9**:561–567, 1839.

[15] C. E. Fritts. **New form of selenium cell, with some remarkable electrical discoveries made by its use**. In *Proc. Amer. Assoc. Advance. Sci.*, number 33, page 97, 1883.

[16] R. S. Ohl. **Light-sensitive electric device**, $27^{th}$ May 1941. U.S. Patent 2402662.

[17] R. S. Ohl. **Light-sensitive electric device including silicon**, $27^{th}$ May 1941. U.S. Patent 2443542.

[18] M. A. Green, K. Emery, Y. Hishikawa, W. Warta, and E. D. Dunlop. **Solar cell efficiency tables (v. 41)**. In *Prog. Photovolt: Res. Appl.*, number 21, pages 1–11, 2013.

[19] K. Tanabe. **A review of ultrahigh efficiency III-V semiconductor compound solar cells: multijunction tandem, lower dimensional, photonic up/down conversion and plasmonic nanometallic structures**. *Energies*, **2**:504 530, 2009.

[20] C. A. Wang, H. K. Choi, D. C. Oakley, and G. W. Charache. **Recent progress in GaInAsSb thermophotovoltaics grown by organometallic vapor-phase epitaxy**. *J. Cryst. Growth*, **195**:346–355, 1998.

[21] M. G. Mauk and V. M. Andreev. **GaSb-related materials for TPV cells**. *Semicond. Sci. Tech.*, **18**:S191S201, 2003.

[22] V. P. Khvostikov, O. A. Khvostikova, P. Y. Gazaryan, et al. **Photoconverters for Solar TPV systems**. In *Proc. 32nd IEEE Phot. Spec. Conf.*, number 1, pages 667–670, 2006.

[23] V. M. Andreev. **An overview of TPV cell technologies**. In *AIP Conf. Proc.*, number 653, pages 289–304, 2002.

[24] M. G. Mauk. *Mid-infrared semiconductor optoelectronics*. Springer Series in Optical Sciences. Springer-Verlag, London, U.K., 2006.

[25] M. W. Dashiell, J. F. Beausang, H. Ehsani, et al. **Quaternary InGaAsSb thermophotovoltaic diodes**. *IEEE T. Electron. Dev.*, **53**:2879–2891, 2006.

[26] V. M. Andreev, V. P. Khvostikov, and A. Vlasov. *Solar thermophotovoltaics*. Springer Series in Optical Sciences. Springer-Verlag, London, U.K., 2007.

[27] J. Baxter, Z. Bian, G. Chen, et al. **Nanoscale design to enable the revolution in renewable energy**. *Energ. Environ. Sci.*, **2**:559–588, 2009.

[28] Heon Ju Lee. *Thermal stability of nano-structured selective emitters for thermophotovoltaic systems*. PhD thesis, Massachusetts Institute of Technology, 2012.

[29] D. L. Chubb. *Fundamentals of thermophotovoltaic energy conversion*. Elsevier B.V., Oxford, U.K., 2007.

[30] D. L. Chubb. **Reappraisal of solid selective emitters**. In *Proc. 21st IEEE Phot. Spec. Conf.*, number 2, pages 1326–1333, 1990.

[31] D. L. Chubb and R. A. Lowe. **Thinfilm selective emitter**. *J. Appl. Phys.*, **74**:5687–5698, 1993.

[32] G. E. Guazzoni. **High temperature spectral emittance of oxides of Erbium, Samarium, Neodymium and Ytterbium**. *Appl. Spectrosc.*, **26**:60–65, 1972.

[33] R. E. Nelson. **Rare earth oxide TPV emitter**. In *Proc. 32nd Power Sour. Conf.*, pages 95–101, 1986.

[34] C. R. Parent and R. E. Nelson. **Thermophotovoltaic energy conversion with a novel rare earth oxide emitter**. In *Proc. 21st Intersoc. Energy Conv. Eng. Conf.*, number 2, page 1314, 1986.

[35] B. Bitnar, W. Durisch, J.-C. Mayor, H. Sigg, and H. R. Tschudi. **Characterisation of rare earth selective emitters for thermophotovoltaic applications**. *Sol. Energ. Mat. Sol. C.*, **73**:221–234, 2001.

[36] H. J. Wang, H. Ye, and Y. Z. Zhang. **Preparation and performance evaluation of $Er_2O_3$ coating-type selective emitter**. *Sci. China Tech. Sci.*, **57**:332–338, 2014.

[37] B. G. Wybourne. *Spectroscopic Properties of Rare Earths*. Interscience Publishers, New York, U.S., 1965.

[38] G. H. Dieke and H. Crosswhite. *Spectra and energy levels of rare earth ions in crystals*. Interscience Publishers, New York, U.S., 1968.

[39] J. D. Joannopoulos, S. G. Johnson, R. D. Meade, and J. N. Winn. *Photonic crystals: molding the flow of light*. Princeton University Press, Princeton, New Jersey, U.S., 2nd edition, 2008.

[40] E. Yablonovitch. **Inhibited spontaneous emission in solid-state physics and electronics**. *Phys. Rev. Lett.*, **58**:2059–2062, 1987.

[41] S. John. **Strong localization of photons in certain disordered dielectric superlattices**. *Phys. Rev. Lett.*, **58**:2486–2489, 1987.

[42] E. Yablonovitch. **Photonic crystals: semiconductors of light**. *Sci. Am.*, **285**(6):47–51, 2001.

[43] S.-Y. Lin, J. Moreno, and J. G. Fleming. **Three-dimensional photonic-crystal emitter for thermal photovoltaic power generation**. *Appl. Phys. Lett.*, **83**(2):380–382, 2003.

[44] J. G. Fleming, S.-Y. Lin, I. El-Dady, R. Biswas, and K. M. Ho. **All-metallic three-dimensional photonic crystals with a large infrared bandgap**. *Nature*, **417**:52–55, 2002.

[45] S.-Y. Lin, J. G. Fleming, and I. El-Kady. **Three-dimensional photonic-crystal emission through thermal excitation**. *Opt. Lett.*, **28**:1909–1911, 2003.

[46] H. Sai, H. Yugami, Y. Akiyama, Y. Kanamori, and K. Hane. **Spectral control of thermal emission by periodic microstructured surfaces in the near-infrared region**. *J. Opt. Soc. Am. A*, **18**:1471, 2001.

[47] H. Sai and H. Yugami. **Thermophotovoltaic generation with selective radiators based on tungsten surface gratings**. *Appl. Phys. Lett.*, **85**:3399–3401, 2004.

[48] H. Sai, Y. Kanamori, K. Watanabe, and H. Yugami. **Spectral control of thermal radiation by metallic surface relief gratings**. In *Mat. Res. S. C.*, number 1162, pages 10–21, 2009.

[49] V. Rinnerbauer, Y. X. Yeng, W. R. Chan, et al. **High-temperature stability and selective thermal emission of polycrystalline tantalum photonic crystals**. *Opt. Express*, **21**:11482–11491, 2013.

[50] V. Stelmakh, V. Rinnerbauer, R. D. Geil, et al. **High-temperature tantalum tungsten alloy photonic crystals: Stability, optical properties, and fabrication**. *Appl. Phys. Lett.*, **103**:123903, 2013.

[51] L. T. Canham, K. G. Barraclough, and D. J. Robbins. $1.3-\mu m$ **lightemitting diode from silicon electron irradiated at its damage threshold**. *Appl. Phys. Lett.*, **51**:1509–1511, 1987.

[52] Trifon Todorov Trifonov. *Photonic bandgap analysis and fabrication of macroporous silicon by electrochemical etching.* PhD thesis, Universitat Rovira i Virgili, 2004.

[53] Moisés Garín Escrivà. *Engineering the thermal emission of macroporous silicon.* PhD thesis, Universitat Politècnica de Catalunya, 2009.

[54] S. Matthias, F. Müller, C. Jamois, R. B. Wehrspohn, and U. Gösele. **Large-area three-dimensional structuring by electrochemical etching and lithography**. *Adv. Mater.*, **16**:2166–2170, 2004.

[55] T. Trifonov, M. Garín, A. Rodríguez, L. F. Marsal, and R. Alcubilla. **Tuning the shape of macroporous silicon**. *Phys. Stat. Sol. (a)*, **204**:3237–3242, 2007.

[56] M. Garín, T. Trifonov, A. Rodríguez, et al. **Improving selective termal emission properties of three-dimensional macroporous silicon through porosity tuning**. *Appl. Phys. Lett.*, **93**:081913, 2008.

[57] M. Garín, T. Trifonov, A. Rodríguez, and R. Alcubilla. **Infrared thermal emission in macroporous silicon three-dimensional photonic crystals**. *Appl. Phys. Lett.*, **91**:181901, 2007.

[58] U. Gasser. **Crystallization in three- and two-dimensional colloidal suspensions**. *J. Phys.: Condens. Matter.*, **21**:203101, 2009.

[59] J. F. Galisteo-López, M. Ibisate, R. Sapienza, et al. **Self-assembled photonic structures**. *Adv. Mater.*, **23**:30–69, 2011.

[60] V. N. Astratov, V. N. Bogomolov, A. A. Kaplyanskii, et al. **Optical spectroscopy of opal matrices with CdS embedded in its pores: Quantum confinement and photonic band gap effects**. *Nuovo Cimento D*, **17**:1349–1354, 1995.

[61] S. G. Romanov, A. V. Fokin, and R. M. de la Rue. **Anisotropic photoluminescence in incomplete three-dimensional photonic band-gap environments**. *Appl. Phys. Lett.*, **74**:1821, 1999.

[62] J. Zhou, Y. Zhou, S. Buddhudu, et al. **Photoluminescence of ZnS:Mn embedded in three-dimensional photonic crystals of submicron polymer spheres**. *Appl. Phys. Lett.*, **76**:3513, 2000.

[63] H. Noh, M. Scharrer, M. A. Anderson, R. P. H. Chang, and H. Cao. **Photoluminescence modification by a high-order photonic band with abnormal dispersion in ZnO inverse opal**. *Phys. Rev. B*, **77**:115136, 2008.

[64] D. N. Chigrin. **Radiation pattern of a classical dipole in a photonic crystal: Photon focusing**. *Phys. Rev. E*, **70**:056611, 2004.

[65] D. N. Chigrin. **Spatial distribution of the emission intensity in a photonic crystal: Self-interference of Bloch eigenwaves**. *Phys. Rev. A*, **79**:033829, 2009.

[66] K. A. Arpin, M. D. Losego, A. N. Cloud, et al. **Three-dimensional self-assembled photonic crystals with high temperature stability for thermal emission modication**. *Nature Communications*, **4**:2630, 2013.

[67] K. Qiu and A. C. S. Hayden. **Thermophotovoltaic generation of electricity in a gas fired heater: Influence of radiant burner configurations and combustion processes**. *Energ. Convers. Manage.*, **44**:2779–2789, 2003.

[68] K. Qiu and A. C. S. Hayden. **Thermophotovoltaic power generation systems using natural gas-fired radiant burners**. *Sol. Energ. Mat. Sol. C.*, **91**:588–596, 2007.

[69] K. Qiu and A. C. S. Hayden. **Development of a novel cascading TPV and TE power generation system**. *Appl. Energ.*, **91**:304–308, 2012.

[70] W. Durisch, B. Bitnar, J. C. Mayor, et al. **Small self-powered grid-connected thermophotovoltaic prototype system**. *Appl. Energ.*, **74**:149–157, 2003.

[71] L. M. Fraas, J. E. Avery, and H. X. Huang. **Thermophotovoltaics: heat and electric power from low bandgap "solar" cells around gas fired radiant tube burners**. In *Proc. 29$^{th}$ IEEE Phot. Spec. Conf.*, pages 1553 – 1556, 2002.

[72] A. Lenert, D. M. Bierman, Y. Nam, et al. **A nanophotonic solar thermophotovoltaic device**. *Nature Nanotechnology*, **9**:126–130, 2014.

[73] N. W. Ashcroft and N. D. Mermin. *Solid State Physics*. Saunders College Publishing, Philadelphia, U.S., 1976.

[74] M. Kolle. *Photonic Structures Inspired by Nature*. Springer-Verlag, Berlin Heidelberg, Germany, 2011.

[75] K. S. Yee. **Numerical solution of initial boundary value problems involving Maxwell's equations in isotropic media**. *IEEE T. Antenn. Propag.*, **14**(3):302–307, 1966.

[76] N. Stefanou, V. Karathanos, and A. Modinos. **Scattering of electromagnetic waves by periodic structures**. *J. Phys-Condens. Mat.*, **4**(36):7389, 1992.

[77] J. W. Hovenier, K. Lumme, M. I. Mishchenko, et al. **Computations of scattering matrices of four types of non-sphericles using diverse methods**. *J. Quant. Spectr. Rad. Transfer*, **55**(6):695–705, 1996.

[78] P. M. Bell, J. B. Pendry, L. Martín Moreno, and A. J. Ward. **A program for calculating photonic band structures and transmission coefficients of complex structures**. *Comput. Phys. Commun.*, **85**:306–322, 1995.

[79] R. Carminati, J. J. Saenz, J.-J. Greffet, and M. Nieto-Vesperinas. **Reciprocity, unitarity and time-reversal symmetry of the S-matrix of fields containing evanescent components**. *Phys. Rev. A*, **62**:012712, 2000.

[80] S. G. Johnson and J. D. Joannopoulos. **Block-iterative frequency-domain methods for Maxwell's equations in a planewave basis**. *Opt. Express*, **8**(3):173–190, 2001.

[81] R. Eisberg and R. Resnick. *Quantum physics of atoms, molecules, solids, nuclei and particles*. John Wiley and Sons, New York, U.S., 2nd edition, 1985.

[82] M. A. Green. **Limiting photovoltaic monochromatic light conversion effciency**. *Prog. Photovolt: Res. Appl.*, **9**:257–261, 2001.

[83] L. Bechger, P. Lodahl, and W. L. Vos. **Directional fluorescence spectra of laser dye in opal and inverse opal photonic crystals**. *J. Phys. Chem. B*, **109**:9980–9988, 2005.

[84] S. M. Sze. *Physics of Semiconductor Devices*. John Wiley and Sons, New York, U.S., 1981.

[85] V. Lehmann and H. Föll. **Formation mechanism and properties of electrochemically etched trenches in n-type silicon**. *J. Electrochem. Soc.*, **137**:653–659, 1990.

[86] R. Memming and G. Schwandt. **Anodic dissolution of silicon in hydrofluoric acid solutions**. *Surf. Sci.*, **4**:109–124, 1966.

[87] X. G. Zhang, S. D. Collins, and R. L. Smith. **Porous silicon formation and electropolishing of silicon by anodic polarization in HF solution**. *J. Electrochem. Soc.*, **136**:1561–1565, 1989.

[88] V. Lehmann. *Electrochemistry of Silicon: Instrumentation, Science, Materials and Applications*. Wiley-VCH Verlag GmbH, Weinheim, Germany, 2002.

[89] A. Michelson and E. Morley. **On the relative motion of the Earth and the luminiferous ether**. *Am. J. Sci.*, **34**:333–345, 1887.

[90] T. Trifonov, L. F. Marsal, A. Rodríguez, J. Pallarès, and R. Alcubilla. **Fabrication of two- and three-dimensional photonic crystals by electrochemical etching of silicon**. *Phys. Status Solidi C*, **2**:31043107, 2005.

[91] S. Cheylan, T. Trifonov, A. Rodríguez, et al. **Visible light emission from macroporous Si**. *Opt. Mater.*, **29**:262267, 2006.

[92] T. Trifonov, M. Garín, A. Rodríguez, et al. **Post-etching shaping of macroporous silicon**. In *Proc. SPIE6593, Photonic Materials, Devices, and Applications II*, page 65931Q, 2007.

[93] M. Garín, T. Trifonov, D. Hernández, A. Rodríguez, and R. Alcubilla. **Thermal emission of macroporous silicon chirped photonic crystals**. *Opt. Lett.*, **35**(20):3348–3350, 2010.

[94] J. E. A. M. van den Meerakker, R. J. G. Elfrink, F. Roozeboom, and J. F. C. M. Verhoeven. **Etching of deep macropores in 6 in. Si wafers**. *J. Electrochem. Soc.*, **147**:2757–2761, 2000.

[95] D. S. Shechtman, I. Blech, D. Gratias, and J. W. Cahn. **Metallic phase with long-range orientational order and no translational symmetry**. *Phys. Rev. Lett.*, **53**:1951–1953, 1984.

[96] R. Merlin, K. Bajerna, R. Clarke, F.-Y. Juang, and P. K. Bhattacharya. **Quasiperiodic GaAs-AlAs heterostructures**. *Phys. Rev. Lett.*, **55**:1768–1770, 1985.

[97] E. Yablonovitch. **Engineered omnidirectional external-reflectivity spectra from one-dimensional layered interference filters**. *Opt. Lett.*, **23**:1648–1649, 1998.

[98] D. Hernández, M. Garín, T. Trifonov, A. Rodríguez, and R. Alcubilla. **Emissive properties of $SiO_2$ thin films through photonic windows**. *Appl. Phys. Lett.*, **100**:091901, 2012.

[99] H. R. Philipp. *Handbook of Optical Constants of Solids*, chapter Silicon dioxide (SiO2) (glass). Academic Press, San Diego, U.S., 1985.

[100] H. R. Philipp. **The infrared optical properties of $SiO_2$ and $SiO_2$ layers on silicon**. *J. Appl. Phys.*, **50**:1053, 1979.

[101] C. J. Mogab. **Measurement of film thickness from lattice absorption bands**. *J. Electrochem. Soc.*, **120**:932–937, 1973.

[102] D. V. Tsu. **Infrared optical constants of silicon dioxide thin films by measurements of R and T**. *J. Vac. Sci. Technol. B*, **18**:1796, 2000.

[103] W. L. Barnes. **Surface plasmonpolariton length scales: a route to subwavelength optics**. *J. Opt. A, Pure Appl. Opt.*, **8**:S87S93, 2006.

[104] S. A. Maier. **Plasmonic field enhancement and SERS in the effective mode volume picture**. *Opt. Express*, **14**:19571964, 2006.

[105] S. Maruyama, T. Kashiwa, H. Yugami, and E. Esashi. **Thermal radiation from two-dimensionally confined modes in microcavities**. *Appl. Phys. Lett.*, **79**:1393, 2001.

[106] H. Sai, Y. Kanamori, and H. Yugami. **High-temperature resistive surface grating for control of thermal radiation**. *Appl. Phys. Lett.*, **82**:1685–1687, 2003.

[107] H. Sai, Y. Kanamori, K. Hane, and H. Yugami. **Numerical study on spectral properties of tungsten one-dimensional surface-relief gratings for spectrally selective devices**. *J. Opt. Soc. Am. A*, **22**:1805–1813, 2005.

[108] D. Kirikae, Y. Suzuki, and N. Kasagi. **Emission spectral control using metal-coated silicon microcavity for thermophotovoltaic**. In *PowerMEMS, Washington DC, USA,*, pages 161–164, 2009.

[109] T. A. Walsh, J. A. Bur, Y. S. Kim, T. M. Lu, and S. Y. Lin. **High-temperature metal coating for modification of photonic band edge position**. *J. Opt. Soc. Am. B*, **26**:1450–1455, 2009.

[110] I. Celanovic, N. Jovanovic, and J. Kassakian. **Two-dimensional tungsten photonic crystals as selective thermal emitters**. *Appl. Phys. Lett.*, **92**:193101, 2008.

[111] D. L. C. Chan, M. Soljačić, and J. D. Joannopoulos. **Thermal emission and design in 2D-periodic metallic photonic crystal slabs**. *Opt. Express*, **14**:8785–8796, 2006.

[112] Y. X. Yeng, M. Ghebrebrhan, P. Bermel, et al. **Enabling high-temperature nanophotonics for energy applications**. *Proc. Natl. Acad. Sci. U.S.A.*, **109**(7):2280–2285, 2012.

[113] M. Ghebrebrhan, P. Bermel, Y. X. Yeng, et al. **Tailoring thermal emission via Q-matching of photonic crystal resonances**. *Phys. Rev. A*, **83**:033810, 2011.

[114] S. L. Firebaugh, K. F. Jensen, and M. A. Schmidt. **Investigation of high-temperature degradation of platinum thin films with an in situ resistance measurement apparatus**. *J. Microelectromech. S.*, **7**:128–135, 1998.

[115] N. Denkov, O. Velev, P. Kralchevski, et al. **Mechanism of formation of two-dimensional crystals from latex particles on substrates**. *Langmuir*, **8**:3183–3190, 1992.

[116] P. Jiang, J. F. Bertone, K. S. Hwang, and V. L. Colvin. **Single-crystal colloidal multilayers of controlled thickness**. *Chem. Mater.*, **11**:2132–2140, 1999.

[117] D. Norris, E. Arlinghaus, L. Meng, R. Heiny, and L. Scriven. **Opaline photonic crystals: How does self-assembly work?** *Adv. Mater.*, **16**:1393–1399, 2004.

[118] G. Taylor. **Disintegration of water drops in electric field**. *Proc. R. Soc. Lond. A*, **280**:383–397, 1964.

[119] A. Coll, S. Bermejo, D. Hernńdez, and L. Castañer. **Colloidal crystals by electrospraying polystyrene nanofluids**. *Nanoscale Res. Lett.*, **8**:26–33, 2013.

[120] J. A. Stratton. *Electromagnetic Theory*. Mcgraw Hill Book Company, New York, U.S., 1941.

[121] H. S. Sözüer, J. W. Haus, and R. Inguva. **Photonic bands: Convergence problems with the plane-wave method**. *Phys. Rev. B*, **45**:1396213972, 1992.

[122] A. Blanco, E. Chomski, S. Grabtchak, et al. **Large-scale synthesis of a silicon photonic crystal with a complete three-dimensional bandgap near 1.5 micrometres**. *Nature*, **405**:437–440, 2000.